Regional Cardiac Ion Channel Heterogeneity and the Mechanisms of Fibrillatory Conduction

by

Katherine Fisher Campbell

A dissertation submitted in partial fulfillment
of the requirements for the degree of
Doctor of Philosophy
(Molecular and Integrative Physiology)
in The University of Michigan
2013

Doctoral Committee:

Professor José Jalife, Chair
Professor Omer Berenfeld
Professor Todd Herron
Professor Anatoli Lopatin

Dedication

This dissertation is dedicated to my family.
To Mom, Ryan, Marie and most especially the loving memory of my Dad,

Thank you for all for your love and support.

Acknowledgements

I would like to thank everyone at the Center for Arrhythmia Research and the University of Michigan for sharing their time, wisdom and experience with me over the last few years. I'm very grateful to Conrado Calvo, Dr. Viviana Munõz, Dr. Sergey Mironov, Jiang Jiang, Dr. Matt Klos, Dr. Michelle Millstein, Luqia Hou, Dr. Sami Noujaim, Dr. Jérôme Kalifa, Dr. Sandeep Pandit, Dr. Sharon Zlochiver, Dr. Kuljeet Kaur, Dr. Guadalupe Guerrero-Serna and Dr. Daniela Ponce Balbuena for their training, collaborations, friendship and guidance throughout my time in the Jalife lab.

I would also like to thank the members of my committee who have guided me through my thesis projects, Dr. Anatoli Lopatin, Dr. Todd Herron and Dr. Omer Berenfeld. I would particularly like to thank Dr. Omer Berenfeld for his continual support, guidance and ideas; as he has been a second mentor to me.

Finally, I would especially like to thank my mentor Dr. José Jalife, who has created something quite special at the CAR, a multidisciplinary and collaborative environment from which I have benefited greatly, both personally and scientifically. More importantly, Dr. Jalife has been a model scientist, teacher and mentor. Without Dr. Jalife's guidance and encouragement I would not be where I am today. I will forever be grateful for this experience.

Table of Contents

List of Figures

List of Tables

List of Abbreviations

APD	Action Potential Duration
MDP	Maximum Diastolic Potential
DF	Dominant Frequency
DF_{max}	Maximum DF in a given region
CV	Conduction Velocity
RI	Regularity Index
AR	Activation Ratio
TPS	Time Space Plot
G_{Kr}	Maximal Conductance of I_{Kr}
G_{K1}	Maximal Conductance of I_{K1}
NRVM	Neonatal Rat Ventricular Myocytes
GFP	Green Fluorescent Protein
hERG	Human Ether-a-go-go Related Gene
Kir2.1	Inward Rectifying Potassium Channel, I_{K1}
Ad-GFP	Adenovirus Encoding for GFP
Ad-hERG	Adenovirus Encoding for hERG with a GFP-tag
Ad-Kir2.1-IRES-GFP	Adenovirus Encoding for Kir2.1 and IRES GFP
UN	Uninfected
W-GFP	Wholly Ad-GFP Infected
W-hERG	Wholly Ad-hERG Infected
R-GFP	Regionally Infected with Ad-GFP
R-hERG	Regionally Infected with Ad-hERG
W-Kir2.1	Wholly Ad-Kir2.1-IRES-GFP Infected

R-Kir2.1	Regionally Infected with Ad-Kir2.1-IRES-GFP
LV	Left Ventricle
RV	Right Ventricle
LA	Left Atria
RA	Right Atria
PV	Pulmonary Veins
AF	Atrial Fibrillation
VF	Ventricular Fibrillation
CHF	Chronic Heart Failure
LQT	Long Q-T Interval Syndrome
SQT	Short Q-T Interval Syndrome
CPVT	Catecholaminergic Polymorphic Ventricular Tachycardia
PAF	Paroxysmal AF
CAF	Chronic AF
BCL	Basic Cycle Length
ADP	Adenosine Di-Phosphate
ATP	Adenosine Tri-Phosphate
HBSS	Hank's Balanced Salt Solution
MNP	Magnetic Nanoparticles

Abstract

Spatial dispersion of action potential duration (APD) is a substrate for cardiac fibrillation, but the mechanisms are still poorly understood. Spatial APD dispersion has also been associated with both regional fibrillatory patterns as well as regional ionic heterogeneities in cardiac tissue. In particular, regional gradients in two major repolarizing potassium channels, hERG (I_{Kr}) and Kir2.1 (I_{K1}), have been implicated in fibrillation. We investigated the role of spatial APD dispersion and the mechanisms by which regional heterogeneity in hERG and Kir2.1 expression contribute to fibrillation. Using a structurally uniform experimental model, neonatal rat ventricular myocyte monolayers, and a novel regional magnetofection technique, we were able to isolate the effects of regional ion channel heterogeneity on electrical propagation. In combination with computer simulations, we were able to provide crucial insights into the underlying mechanisms of arrhythmias.

Regional hERG overexpression shortened APD and increased rotor incidence in the infected region. It also generated fibrillatory conduction in a frequency- and location-dependent manner. The APD gradient only generated wavebreak if activity was faster than 12.9 Hz and originated within the infected region. Simulations determined that hERG-induced transient hyperpolarization is an important factor in rotor frequency but is not significant for the generation of wavebreak. In contrast, Kir2.1 overexpression generates both APD shortening as well as a stable

hyperpolarization of the resting membrane potential. Regional Kir2.1 heterogeneity results in both an APD gradient as well as bimodal spatial and frequency-dependent conduction velocity (CV) gradient. Simulations reveal the bimodal CV gradient to be the result of the balance of sodium channel availability and potassium conductance. Regional Kir2.1 overexpression generated fibrillatory conduction in a frequency and location dependent manner. However, the minimal frequency required for wavebreak was only 10.8 Hz; this suggests that tissue containing Kir2.1 gradients may be more susceptible to fibrillation than tissue containing hERG gradients. This study provides insight, at the molecular level, into the mechanisms by which both spatial APD and bimodal CV dispersion contribute to wavebreak, rotor stabilization and fibrillatory conduction.

Chapter I

Cardiac Fibrillation: Background and Introduction

1.1 Introduction

Cardiac fibrillation is a major cause of morbidity and mortality throughout the world. Atrial fibrillation (AF), the most common clinical arrhythmia[1], currently affects an estimated 2.2 million Americans[2, 3]. Ventricular fibrillation (VF) is the leading cause of sudden cardiac death in industrialized nations; accounting for nearly 300,000 annual fatalities in the United States alone[4, 5]. Cardiac fibrillation is a disruption of the electrical activation of the myocardium which prevents the normal coordinated contraction of the heart's chambers. Clinically, this electrical disruption can be observed on the electrocardiogram (ECG) by an irregular, undulating and variable morphology of either the P-wave, in the case of AF, or of the QRS complex, in the case of VF. Both AF and VF can have serious and all too often fatal consequences. AF can cause alterations to ventricular frequencies resulting in lethargy, syncope, heart failure, and is the leading cause of stroke[6]. VF causes the failure of coordinated contraction of the ventricles, preventing an adequate generation of force necessary to pump the blood to the rest of the body;

from there it only takes 3-6 minutes after the brain stops receiving oxygen for death to occur.

Traditionally, complex and irregular ECG traces associated with AF and VF were thought to be the result of multiple randomly wandering wavelets of electrical activity throughout the heart[7, 8]. However, AF and VF turn out to be more organized than the ECG would first suggest[9, 10]. Over the last 20 years or so, numerous advances in spatial-temporal imaging, computer simulations, molecular and genetic techniques have allowed investigation into the dynamics of fibrillatory behavior and, just as importantly, the structural, ionic, molecular and genetic mechanisms underlying these dynamics. We are now at a technological point where we can integrate these differing tiers of structure as they individually and collectively contribute to the generation and maintenance of cardiac arrhythmias. With such efforts, we may be able to improve patient outcomes through the development of better designed and targeted treatments, as well as preventative measures for cardiac arrhythmias.

The data presented in this thesis is but a small addition to the vast sum of work which has been conducted investigating the mechanisms of cardiac arrhythmias. Without the scientific advancements by many creative and excellent investigators this work could not have been accomplished. In this chapter I will briefly pay homage to some of the major contributors to arrhythmia research, discussing some of the key conceptual building blocks to our current understanding of cardiac fibrillation. However, in the interest of cohesion I will refrain from covering topics not primarily relevant to the mechanisms investigated in my thesis work. It is important to note that there are many other significant contributors to our modern understanding of cardiac activity, which were not given attention in these pages. From the historical and conceptual

framework in this chapter, I will lead into a discussion of some of the more recent findings which brought about the questions addressed by my thesis research. In particular, I will present recent investigations into the role of regional ionic heterogeneity as they relate to the control of fibrillatory dynamics. The subsequent chapters will each present data on the two main projects I have worked on over the past 6 years in the Jalife lab. Both projects are concerned with regional heterogeneity of a separate repolarizing potassium channel and how each contributes to wavebreak and fibrillation by individual mechanisms. The final chapter of this thesis will provide a summary of my work along with future directions for these topics.

1.2 Historical Perspective

Gigantum humeris insidentes
Standing on the shoulders of giants
– Bernard of Chartres
John of Salisbury, *The Metalogicon* 1159

1.2.1. Cardiac Fibrillation

The ancient world has long since recognized the phenomenon of cardiac fibrillation, the earliest description occurring in Egypt in 3500 BC. In a passage from the Ebers Papyrus, ventricular fibrillation was described as “when the heart is diseased, its work is imperfectly performed: the vessel proceeding from the heart become inactive, so that you cannot feel them… If the heart trembles, has little power and sinks, the disease is advancing and death is near”. Sometime between 1696 and 2598 BC in China, the Yellow Emperor Huang Ti Nei Ching Su Wên was the first to describe atrial fibrillation[11], “When the pulse is irregular and tremulous

and the beats occur at intervals, then the impulse of life fades; when the pulse is slender (smaller than feeble, but still perceptible, thing like a silk thread), then the impulse of life is small." While medicine has long since recognized the poor prognosis associated with irregular heart rates, it still took about 4000 years to develop our modern conceptions of fibrillation.

Early modern descriptions of fibrillatory behavior came in 1543 with Andreas Vesalius's animated description of VF as "worm-like" movements of the heart before death[12] and then in 1628 when William Harvey first described the "fibrillation of the auricles" in animals[11]. An important step in the conceptual development of cardiac function came by way of physicist and physiologist Luigi Galvani in 1791 as he discovered "animal electricity" establishing the link between muscular movement and electrical impulses[13]. Fifty years or so later in 1842, Erchsen published experimental results demonstrating the relationship between coronary artery ligation with a termination of coordinated ventricular beats and death; the heart only retaining "slight tremulous motion"[14]. Shortly thereafter in 1850, Hoffa and Ludwig linked bioelectricity to ventricular functional disruption through the demonstration that faradic currents terminated adequate contraction of the ventricle[15]. In 1874, Vulpian first coined "movement fibrillaire" a phrase we still use today[16]. It was without the advent of an ECG that in 1887, McWilliams proceeded to further detail the visual description of VF ("fibrillar contraction") and gave the first demonstration of electrical defibrillation in a human through the use of electrodes, a technique which, although improved upon, is still an invaluable tool in the treatment of cardiac arrhythmias[17]. He was also the first to suggest that fibrillation may be the result of a kind of reentrant activity, "the contraction would naturally be propagated from one

contracting fiber to another over which the contraction wave had already passed"[18].

The next major advancement in arrhythmia research came by way of the invention of the electrocardiograph (ECG) by William Einthoven in 1900. The ECG would become, and still remains the primary cardiac diagnostic tool for clinicians. This device allows for collection of detailed information about the spatial and temporal electrical progression throughout a patient's chest. In 1909 Sir Thomas Lewis, a friend of Einthoven's, was the first to use the ECG to record human AF[19] while it was Hoffman in 1912 who was the first to record and publish an ECG illustrating human VF[7]. It is within these first decades of the 20th century that we start to see some of the first modern descriptions of the mechanisms of arrhythmias. In 1909, work by Alfred Mayer, first in rings of the subumbrella from the medusa jellyfish[1] clearly demonstrated the concept of reentrant paths of propagation. Mayer was able to investigate the relationships between conduction velocity (CV), path length and refractory period. "The wave will maintain itself indefinitely provided the circuit be long enough to permit each and every point in it to remain at rest for a certain period of time before the return of the wave through the circuit."[20] He also pointed out that the area of tissue where the impulse originated from was no more involved in the maintenance of the propagating wave than any other point of the tissue.

In about 1914, Garrey using loggerhead turtles observed that ringed slices of ventricular tissue taken from a fibrillating heart continued to fibrillate as long as there was a minimal tissue size of 4 square millimeters. He observed that as the ring of tissue was thinned, the disorganized fibrillatory activity would organize into rotating waves around

[1] *Cassiopea xamachana*

the ring of tissue which he called “intramuscular ringlike circuits, with resulting ‘circus contractions’”[21] (Figure 1.1.A). These results coincided with work by George Mines[22] in cold blooded animals during which he was able to link the concept of reentrant propagation to the development of cardiac arrhythmias[20]. Following these advances, in 1925, Thomas Lewis provided backing to the reentrant idea with his observations in the canine atria, concluding that “a wave circulates around a natural opening in the muscles of the auricle”[20]. Work by these men culminated in the concept of circus movement reentry, a predecessor to some of our current models of reentry driven fibrillation (Figure 1.1.A).

In the 1930s, high speed cinematography started to be used to investigate the mechanisms of VF. Using a canine model, Wiggers was able to define 4 separate stages of VF in which VF frequency progressively declines; 1) undulatory - lasting less than 5 seconds, 2) convulsive incoordination – 15 to 40 seconds, 3) tremulous incoordination – 2 to 3 minutes, and finally 4) atonic fibrillation - taking place 2 to 5 minutes after VF initiation[23].

1.2.2. The Action Potential

Concurrent with the evolution of the mechanisms responsible for fibrillatory dynamics was the development of theories explaining electrical excitation and propagation in excitable tissues. In 1902, Julius Bernstien came up with a hypothesis which stated that the resting potential of an excitable cell[2] was due to the concentration of potassium ions. He suggested that excitation was the result of a change in permeability of the

[2] Bernstien’s primary interest was in the excitable properties of nerve cells rather than cardiac cells.

cell's membrane[24]. Cole and Curtis in the 1930's went on to discover how the resistance across a cell membrane changed as cells became excited. They found that the voltage of a cell could be described in terms of a resistor in parallel with the capacitance of the cell's lipid bilayer[25, 26].

In 1949, Silvio Weidmann and Edouardo Coraboeuf[3] were the first to record a cardiac action potential using a glass microelectrode[4] impaled into the false tendon (Purkinje fiber) in the right ventricular endocardium of a canine heart[27]. Subsequent work by Weidmann and Draper was able to determine the absolute magnitude and resting membrane potential of canine cardiac cells[28]. Also in the 1950's, Alan Hodgkin and Andrew Huxley determined that it is the influx of sodium ions which is responsible for the depolarization of the cells membrane potential. From their work they developed the action potential theory and mathematically described how an excitable tissue, the giant squid axon in this case, was able to propagate electrical signal through the passage of ions across the cell membrane[29, 30]. They generated a set of differential equations which took into consideration the rates of flow of sodium and potassium currents; these rates would later be attributed to specific conformational changes of ion channel structure. This model is the predecessor to the computer simulations which are so often used to investigate the mechanisms of cardiac arrhythmias.

Further demonstrating the importance of membrane permeability to sodium, Weidmann was able to assess the voltage-dependent inactivation of sodium current (or "Na^+ carrying system") and its role in the action potential upstroke in the squid axon[31]. He also demonstrated that depolarization of the resting potential by K^+ results in a corresponding

[3] They were working in Hodgkin and Huxley's lab at Cambridge.
[4] A technique developed by Ling and Gerard (1949) and Nastuk and Hodgkin (1950).

APD shortening, and suggested that "K^+ ions may increase the permeability of the fiber membrane to K^+ ions, causing increased outflow of positive charge."[5]

In the 1960's, further specification of the cardiac currents were used in adapting the Hodgkin-Huxley equations to cardiac cells. Denis Noble made significant improvements by adding the inward rectifying potassium channel I_{K1} and slowing the kinetics of the delayed rectifier potassium current[32, 33]. Such adaptations allowed for the generation of waveforms which mimicked the changes in voltage of an excited cardiac cell. The advent of the voltage clamp technique, which allows for sensitive measurements of ionic currents passing through a cell while controlling the cells potential, greatly enhanced our understanding of the different currents involved in cardiac excitation. This led to more detailed information about potassium, calcium and sodium currents to be integrated into the existing models of cardiac excitation[34, 35]. These improvements demonstrated a mathematical comprehension of the ionic mechanisms of cardiac excitation.

These seminal works provided the framework to our understanding of the cardiac action potential. Simply put, the action potential is a change in a cell's membrane potential as it becomes excited and returns to rest. The changes in membrane potential are the result of the cumulative passage of different ionic currents across the cells membrane through different ion specific membrane-spanning channels. The resting potential of cardiac cells is primarily determined by a potassium current passed through the I_{K1} channel. This potassium current, being predominant when

[5] Edward Carmeliet later demonstrated the extracellular potassium sensitivity of its permeability (1961).

the cell is at rest, causes the membrane potential to stabilize near the electrochemical equilibrium potential for potassium[6].

In order to generate an action potential there needs to be an adequate application of depolarizing current; once the cell reaches its threshold potential, the cell will have an automatic response generating an action potential. As the cell becomes more depolarized voltage-sensitive sodium channels open causing a rapid influx of positively charged sodium[7] into the cell. Even though the sodium channel quickly inactivates, its significant influence depolarizing the membrane potential results in the activation of a number of potassium (primarily the transient outward potassium channel I_{to} and the slow and rapid delayed rectifying potassium channels, I_{Ks} and I_{Kr}) as well as calcium channels (primarily the L-type calcium channel, I_{CaL}) which continue the action potential. Calcium channels continue to generate depolarizing current into the cell; while potassium channels generate repolarizing current sending potassium out. Influx of calcium into the cell is a crucial determinant of the contractile function of the heart. It induces a process of calcium-induced calcium release from the sarcoplasmic reticulum. The influx of calcium activates the contractile proteins which generate the force of contraction used by the heart to pump blood to the rest of the body(36). For the most part these inward and outward currents balance each other, and generate a plateau phase during the action potential which keeps the cell at a relatively steady positive voltage. That is until the potassium currents overwhelm the

[6] Nernst's work in chemical thermoequilibrium resulted in an equation correlating chemical energy with the electric potential of an excitable cell or battery. $E_X = {}^{RT}/_{F} \ln({}^{[X]out}/_{[X]in})$ where E is the equilibrium potential of ion X, T is temperature in Kelvin, R is the gas constant and F is the Faraday constant.

[7] In nodal cells calcium channels are responsible for the upstroke of the action potential.

declining calcium current[8] and the cell begins to repolarize. During the final phase of repolarization the I_{K1} channels reopen, fully returning the cells membrane potential to rest.

The time it takes for the cell to become activated and return to rest is the action potential duration (APD) and is a useful investigative tool. However, even after the cell has returned to rest, often the structure of many of the ion channels, primarily I_{Na} and I_{Ks}, have not returned to a conformational state which is capable of quickly reopening. During this phase of the action potential, or effective refractory period, a depolarizing impulse cannot re-excite the cell.[9] In addition to ion channels, there are a number of electrogenic exchangers and ATPases which are just as important to re-establishing the cells resting ionic gradients. All of these elements come together to control the membrane potential and culminate in the characteristic profile of an action potential. It's important to point out that within the heart, different cell types and regions have specific relative amounts of each of these channels which correspond to different action potential profiles for each cell type or region. This cellular and regional specification plays an important role in the spread of cardiac excitation and generating the synchronized electro-mechanical function of the heart.

1.2.3 Action Potential Propagation

Lord Kelvin first described in 1855 how current and voltage are propagated along a cable(37). His interest was in the development of the

[8] Calcium channels inactivate by way of a fast calcium-dependent and slow voltage-dependent inactivation process.

[9] There is also a relative refractory period which requires a much stronger depolarizing impulse but will be able to generate an action potential response.

transatlantic telegraphic cable[10] and as such his work describes the passage of current along a passive uniform structure. In the 1870's, Hermann began to model neuronal electrotonic potentials; while Hoorweg was the first to apply Kelvin's cable equations to bioelectric propagation in 1898. These advances finally lead to the development of the cable theory for neuronal fibers in the early 20th century, independently arrived at by Hermann and Cremer. These cable equations describe the passage of voltage along a passive membrane and can be likened to the passage of current through a line of cells at a sub-threshold voltage. Essentially, they model the spread of electrotonic current at a distance from a stimulus; or how much of the current is spent locally discharging the cell's membrane capacitance compared to how much current is able to continue down the cable. To describe this idea we can use the concept of the space constant, λ, which is the distance at which the original voltage has decreased to 63% of its original value.[11] The cable theory was first successfully applied to the propagation in nerve fibers by Hodgkin and Rushton, together developing of the concept of electrotonus. They found that the passive behavior of the fiber could be determined by 4 electrical constants: 1) the electrical resistance of the extracellular fluid, 2) the resistance of the intracellular fluid, 3) the capacitance of the membrane and 4) the resistance of the membrane.

Curtis and Cole in 1942 and Hodgkin and Huxley in 1945 concluded that these equations do not fully encompass the instance of electrical progression through excitable media[(29, 38)]. To conceptualize the interaction of depolarizing and repolarizing currents, as a wave progresses through excitable tissue, in 1937 Rushton developed the concept of liminal

[10] The first transatlantic cable was sent in 1858.

[11] $\lambda = (r_m/r_i)^{0.5}$ where r_m is the membrane resistance and r_i is the intercellular resistance.

length[37]. To understand this parameter we can look at the example of a line of excitable cells, an action potential generated at one end will first send some depolarizing current onto the next couple cells down the line. Unlike the case of a passive cable, cardiac cells are tightly tuned to respond to changes in voltage by opening or closing several ion channels. The first initial flow of sub-threshold depolarizing current into the downstream cells will cause them to respond with an increase in outward potassium current. In these first cells the increased resistance to depolarization serves as a current sink; meaning more depolarizing current is used to offset the increased potassium current. This then decreases the amount of depolarizing current available to pass on to the next cells down the line. Once there is enough depolarizing current to overcome this reactionary increase in potassium current, threshold can be reached and the action potential generates in that cell. So, in a line of cells where the first one is freshly depolarized, the first couple cells down the line will be experiencing a net influx of positive charge while the couple cells further down will have a net efflux of positive charges as they resist depolarization. The length of fiber which needs to be raised above threshold in order for the depolarizing wavefront to overcome the increased outward potassium current of the cells downstream and propagate the action potential is considered the liminal length.

The success or failure of propagation has to do with the balance between the magnitude of the incoming current from the excited cell and its ability to pass it on and depolarize the downstream cell past threshold. The I_{Na} channel is primarily responsible for the first part[12]. Gap junctions,

[12] In some cell types calcium channels are primarily responsible for depolarization rather than sodium. Additionally channels which exert an influence over the resting membrane potential have the ability to influence sodium channel availability can also have a contributing role in the magnitude of the incoming current from an excited cell.

which are channels that span between the intercellular space of neighboring cells, are then responsible for the passage of current between cells. The I_{K1} channel is primarily responsible for resisting depolarization to threshold. The proper balance of these parameters determines whether a wavefront will successfully propagate and is crucial for normal cardiac function.

1.2.4 From Multiple Wavelets to Rotors

By the 1950's and 60's a new theory to explain the mechanisms of fibrillation started to evolve. Moe suggested that fibrillation may be initiated by either a rapidly firing focus, a premature systole or circus reentrant activity; however he was skeptical that simple circuit reentry could generate the complex and irregular patterns often observed during fibrillation and envisioned that the maintenance of fibrillation was the result of "randomly wandering wave fronts, ever–changing in direction"[39, 40]. Moe and colleagues took advantage of the rapid technological advancements in computer science of the 20th century by applying computer simulations in the investigation of cardiac arrhythmias[8]. Using a model of a two-dimensional sheet of myocardium consisting of 992 units, each with a randomly assigned refractory state, they were able to demonstrate that fibrillation existed as a stable state maintained by irregularly wandering multiple wavelets. Large numbers of wavelets were able to sustain fibrillation as long as the area was sufficiently large and the refractory period sufficiently brief. Moe's simulations predicted that 23-40 wavelets were necessary to maintain fibrillation[8]. Experimental evidence for the theory of multiple wavelets came about 20 years later from experiments by Allessie[41] using high-resolution electrode mapping;

However, Allessie suggested that only 4-6 wavelets were necessary to maintain fibrillation.

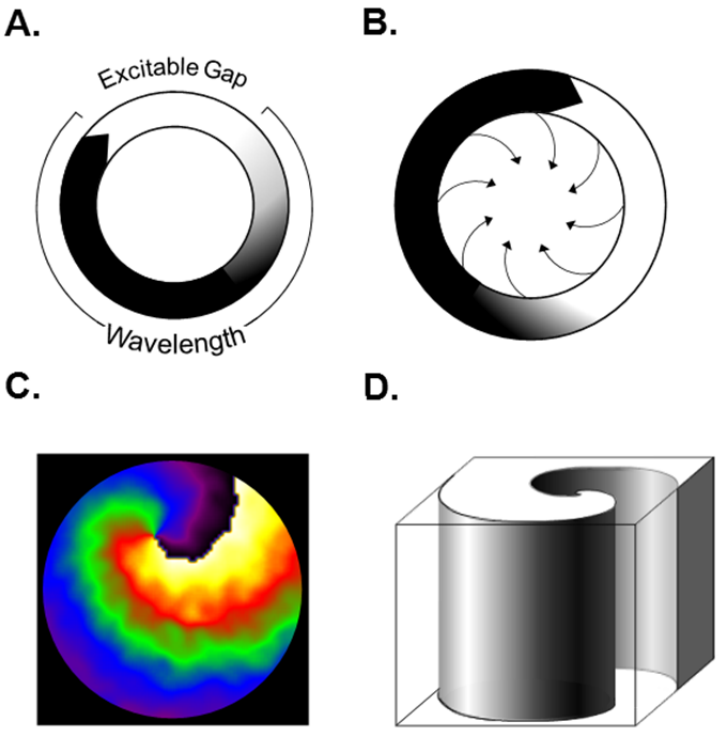

Figure 1.1. Reentry, Basic Concepts. A. Schematic of reentry around a ring-like anatomical obstacle, wavelength (black-grey) is shorter than the path length allowing for a fully excitable gap (white). **B.** Schematic of leading circle reentry around a functional obstacle. **C.** Two-dimensional rotor rotating around an unexcited but excitable core. **D.** Schematic of a three-dimensional scroll wave.

Allessie gave rise to the notion of the “leading circle”, or reentry without the presence of an anatomical obstacle[42-44] (Figure 1.1.B). Allessie was able to observe functional reentry in the absence of an anatomical obstacle. Furthermore, he proposed that the center of the reentry was kept in a refractory state due to the centripetal wavefronts passing depolarizing current, and that the dynamics of the reentrant path were determined by the smallest loop which could maintain this circling behavior. Defining the length of the smallest loop he found to be the conduction velocity and refractory period of the tissue.

By the 1970's, the idea of electrical reentry around a structural obstacle was well established[42, 43, 45, 46], however, the original description by Lewis and Mines does not fully replicate the activity observed during fibrillation. Work on a thermodynamically driven chemical reaction (Belousov-Zhabotinski or B-Z reaction) demonstrated the generation and maintenance of spirals in a media[47]. Spirals can be observed throughout the natural world, from harmless sea shells to devastating and dynamically evolving hurricanes and tornadoes. So it may be unsurprising, at least from our modern perspective that this iterative pattern can be found within the human body. Krinskii used cellular automata models and derived the necessary condition for self-sustaining activity[48]. Similarly, Gulko and Petrov conducted simulations based on the B-Z reaction suggesting that functional reentry (or "reverberators") was feasible in the heart[49]. In the 1980's, Winfree enhanced this work with a pinwheel experiment in which regional phase heterogeneity results in sustained spiral waves, this was demonstrated in cardiac tissue by Ideker *et al.*[50, 51]. Winfree was also the first to coin the terms we most commonly use today to describe this reentrant behavior, the "rotor" and "spiral wave" (Figure 1.1.C). He later went on to expand and adapt the idea of the rotor to three dimensions, describing the scroll wave using simulations (Figure 1.1.D).

In the 1990's work by the Jalife lab further demonstrated the importance of rotors as organizers of behavior during fibrillation[52-55]. The rotor hypothesis says that rotors are the primary organizers of fibrillation, and that it is the underlying ionic, molecular and temporal properties of the cardiac tissue which both establishes the rotors as well as determines the complexity of the arrhythmias[56]. Studies using high-resolution mapping using either electrode arrays or voltage-sensitive fluorescent dyes have provided ample evidence to support the idea that the dominant

mechanism sustaining many types of fibrillation is reentry[51, 57-61]. This has changed the focus from random multiple wavelets to the rotor hypothesis, bringing an improved version of Lewis and Mines' model of reentry back into vogue[56].

1.2.5 The Advent of Optical Mapping

Over the last 40 years, major technological advances have provided much insight into the mechanisms of arrhythmias. One such technique prominently used to study cardiac arrhythmias, and employed in this thesis, has been optical mapping. Optical techniques initially employed by Wiggers[62] have substantially evolved to become one of the most useful tools in studying the dynamics of cardiac fibrillation. First employed by Salzberg[13] in 1973 to neuronal tissue and then by Morad and Salama to cardiac tissue[63, 64], optical mapping uses highly lipophilic potentiometric dyes to visualize excitation and propagation in the myocardium with a much higher degree of spatial and temporal accuracy than alternative electrode mapping techniques[65, 66]. Many advancements have been made in the developments of these first dyes. Problems such as photobleaching, insufficient signal to noise ratios and phototoxicity needed to be addressed. Dyes such as Di-4-ANEPPS and Di-8-ANEPPS developed by Leslie Loew *et al.*[67] have become the primary voltage sensing dyes because of their high signal and low levels of phototoxicity.

The primary mechanism for the fluorescent voltage-sensing dyes used throughout this thesis is one of reorientation[14]. Dyes such as Di-8-

[13] Merocyanine 540 was the first dye which was used to measure action potentials.

[14] Other mechanisms employed by voltage sensitive dyes are On-Off mechanisms (common to cyanine and oxonol dyes, kinetics on the order of 0.01 seconds) or

ANEPPS contain different chromophores which when illuminated by a specified wavelength, generate a characteristic emission spectrum. As the cardiac cells become excited, depolarizing the membrane potential of the cell, the dye located in the cell's lipid membrane senses the change in voltage causing the chromophore portion of the molecule to shift a charge, resulting in a change in the emission spectrum of the molecule. When the cell returns to rest so does the dye's chromophore, which results in a return to the dye's original emission spectrum. Using the correct set of excitation and emission filters (Figure 2.1) one can record the propagation of electrical activity throughout a tissue by looking at the progression of this shift in emission spectrum[65, 66]. This technique generates so-called optical action potentials which are an average of the temporal activation and repolarization of the cells within 1 pixel. Optical mapping allows for excellent visualization of electrical dynamics during fibrillation, with a spatial resolution on the order of micrometers and temporal resolution of 1-2 KHz[66].

1.3 Wavebreak and Reentry

Even before the advent of the rotor, it was demonstrated that circus movement reentry could be initiated by unidirectional block around an obstacle (Figure 1.1.A). Similarly, functional reentry requires an obstacle. However, rather than traversing the obstacle on a given path; functional reentry uses the obstacle to break the wavefront to generate rotors.

Obstacles which result in functional reentry can be any number of anatomical or functional inhomogeneity in the cardiac tissue, from fibrosis

---

redistribution mechanisms (such as TMRE, kinetics on the order of second) which alter the dyes location upon changes in voltage[72]).

or ischemia to regional or temporal heterogeneities in excitability. In particular, spatial dispersion of APD and refractoriness has been identified as a major factor for arrhythmogensis[68-70]. For nearly 100 years, from Mines' demonstrations of unidirectional block in 1913, it has been clear that, to achieve uniform propagation downstream, cells must have already returned to rest in order for them to be re-excited. If regions of downstream cells have not returned to rest when a new wave approaches they are not able to become excited and the wave becomes disrupted; neighboring regions of tissue which have differing APD or refractoriness can easily create this situation.

Figure 1.2 shows the collision of a wavefront (white) with such an obstacle (red). Once the wave makes contact with the obstacle it can take on one of several behaviors, primarily determined by the excitability of the tissue. If the tissue is highly excitable the wave breaks but is able to circumnavigate the obstacle reforming the wavefront. If the tissue is less excitable, the conduction velocity is slower such that curvature of the wavefront (R) will decrease at the edge of the obstacle. Once excitability has reduced such that the curvature is below a critical value (R_{Cr}) the wavefront will detach from the obstacle and will not be able to rejoin its other broken end. In this instance the detached waves, still curling, turn into rotors. If excitability is reduced further, the same detachment will occur, but the broken ends do not have enough curvature to form sustainable rotors and will undergo decremental conduction and die off[71]. In addition to the excitability of the tissue and the critical curvature of the wavefront, the shape of the obstacle and the frequency of excitation also play a role in rotor formation[72]; sharper obstacle edges and higher pacing frequencies increase the chances of wavebreak[73].

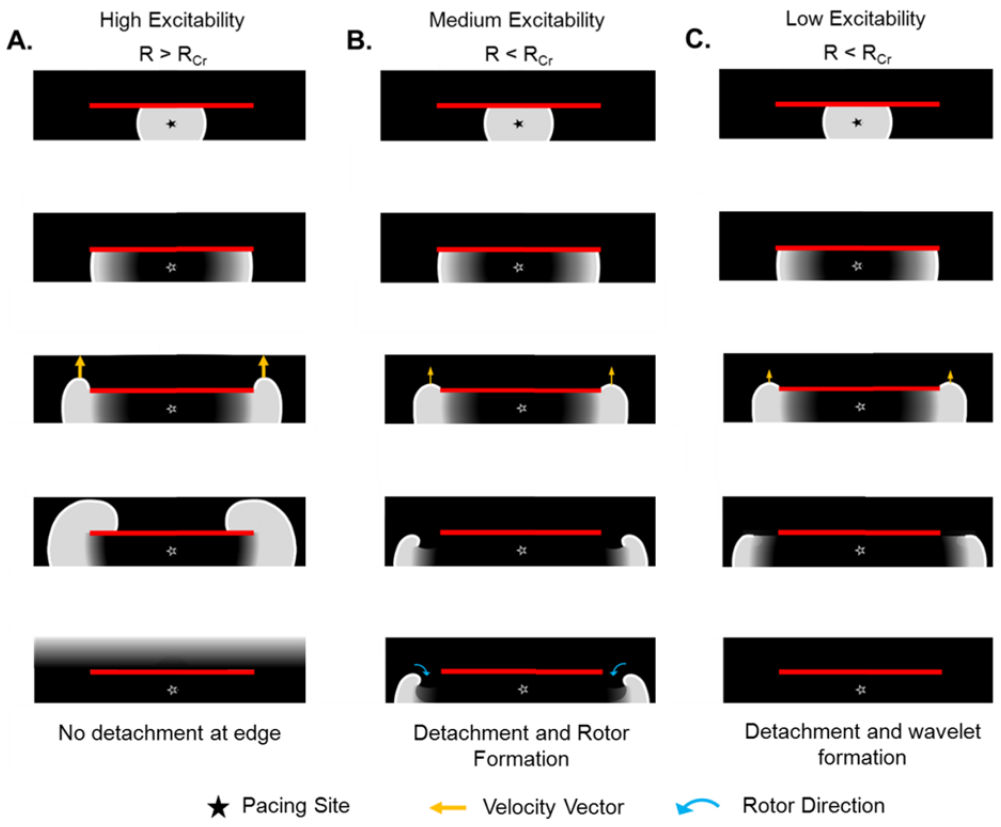

Figure 1.2. Wavebreak and Rotor Initiation. A. Schematic of a wave initiated at the star (the wavefront in white and repolarized tissue in black) as it comes in contact with an obstacle (red line). When there is sufficiently high excitability, the curvature of the wavefront (R) in the third panel down is great enough that the wave does not detach from the obstacle. **B.** As cardiac excitability is reduced the curvature of the wavefront (3rd panel down) falls below a critical curvature (R_{Cr}) which leads to detachment from the obstacle leading to rotor initiation. **C.** As excitability is reduced further detachment occurs but there is a further decrease in the curvature which prevents the generation of rotors and results in waves which undergo decremental conduction (adapted from Cabo *et al.*[73]).

Another way to look at whether or not an obstacle will result in rotor formation is to examine how the excitatory nature of the wavefront compares with the excitatory properties of the tissue it is coming across.

This is otherwise known as source-to-sink mismatch and is an important concept for grasping the mechanics of a rotor.

The amount of source-to-sink mismatch a propagating wave encounters is determined by how much excitatory charge the cells at the front of the wave need to pass on to the cells just in front of the wave in order to propagate[36]. If we first consider a simplified example of a homogenous layer of tissue, we can investigate what effect source-to-sink mismatch has on the relationship between the conduction velocity (CV) and the curvature of the wavefront[74]. In the case of a planar wave, we can think of each cell along the wavefront activating progressively more cells in front of it in a 1 to 1 ratio. If the wavefront were to become concave, the number of cells needed to be activated is fewer than the number of cells already activated, and so less current is needed before the downstream row of cells reach threshold; this translates into an overall increase in conduction velocity. Conversely, in the instance of a convex wave, the wavefront has more cells to activate than are already activated, thus more current is needed before threshold is reached in the downstream row of cells; this translates into a decrease in conduction velocity. When the curvature becomes more convex, as is the case in a spiral as one proceeds towards the tip, the conduction velocity progressively slows. Propagation in the direction perpendicular to the wavefront continues until a critical curvature is reached at which point the curvature is so great that the wavefront cannot pass enough depolarizing current to the downstream cells to elicit an action potential.

The critical curvature of a rotor generates a region of cells known as the core around which it rotates[15] (Figure 1.3). It's important to note that while the waves continuously spiral around a core region of cells, these cells are still functional and are not acting as a structural obstacle. The cells within the core of the rotor receive a continuous depolarizing current while the phase singularity remains close. However, as the core is being generated by the curvature of the wavefront, it has a reciprocal effect on the wavelength (WL)[(60)], wavelength being a product of the conduction velocity (CV) and the time a cell takes to become excited and return to rest, the action potential duration (APD)[(75)]. Cells in the core become a prevailing sink for the current to drain into; the voltage difference results in an electrotonic effect on the cells near the core generating shorter APD and consequently shorter WL. The point of critical curvature, combined with these electrotonic effects generates a point considered the phase singularity or singularity point and is at the pivot point of every rotor (star in Figure 1.3). At this point all of the portions of the wave from the wavefront and wavetail meet up circling this phase singularity. With the advent of optical mapping techniques which allow for the clear visualization of rotors, Grey *et al.* developed an analytical method which can identify and track phase singularities by transforming optical signals into phase space over a range between π and $-\pi$[(58)]. By referencing the fluorescence signal of a pixel at time t and $t+\tau$ (where τ is a quarter of the rotation time) to the mean fluorescence of the pixel (F_{mean}), an equation representing the relative progressions of phase in addition to identification of the singularity point can be generated for further analysis.

[15] Not all cores are stably defined; the singularity point may take on a variety of meandering patterns which are thought to be the result of the relative contribution of the curvature, wavefront-wavetail interactions and electrotonic currents from the core.

Many of the dynamic properties of rotors have been shown to heavily rely on the relative contribution of tissue excitability and APD. Increased tissue excitability is permissive of a higher critical curvature which can result in faster rotor frequencies and greater rotor stability, while an increased APD and wavelength can generate wavefront-wavetail interactions which can reduce both the frequency and stability of a rotor forcing it to meander and even leading to rotor termination. As excitability and APD are the primary result of the interaction of different ionic currents, further investigation of individual and collective roles of these currents is warranted.

1.4 Rotors and Excitability – I_{K1} and I_{Na} Interactions

The inwardly rectifying potassium channel (I_{K1}), has been shown to play a vital role in the control of rotor frequency and stability[76-78]. At rest, I_{K1} channels pass current and are primarily responsible for the control of the resting membrane potential. The conductance through I_{K1} decreases as the membrane depolarizes due to intracellular block by polyamines such as spermine, spermidine and putrescine[79-83]. The I_{K1} channel is formed by 4 Kir2.x membrane spanning subunits encoded by the genes *KCNJ2, KCNJ12* and *KCNJ4*. A recent study in humans has suggested that a larger I_{K1} density in the left atrium explains the dominant left-to-right frequency gradients that prevail in patients with paroxysmal AF[84]. Additionally, mutations in Kir2.1 are associated with short QT syndrome type 3 (SQT3), familial AF, Anderson's syndrome and catecholaminergic polymorphic ventricular tachycardia (CPVT), further identifying Kir2.1 as an important regulator of fibrillatory dynamics and a potential therapeutic target [85-88].

In the heart I_{K1} is composed of heterotetramers of Kir2.1-2.3; the proportion of each of the three proteins varying dependent on species as well as the location and cell type within the heart[89]. However, it appears that Kir2.1 is the primary component of I_{K1} in the heart. Kir2.1 and Kir2.2 knockout mouse models demonstrated that while the Kir2.2 knockout mice had an I_{K1} which was reduced by 50%, the neonatal Kir2.1 knockout mice had no I_{K1} at 4mM external K^{+}[84-85].

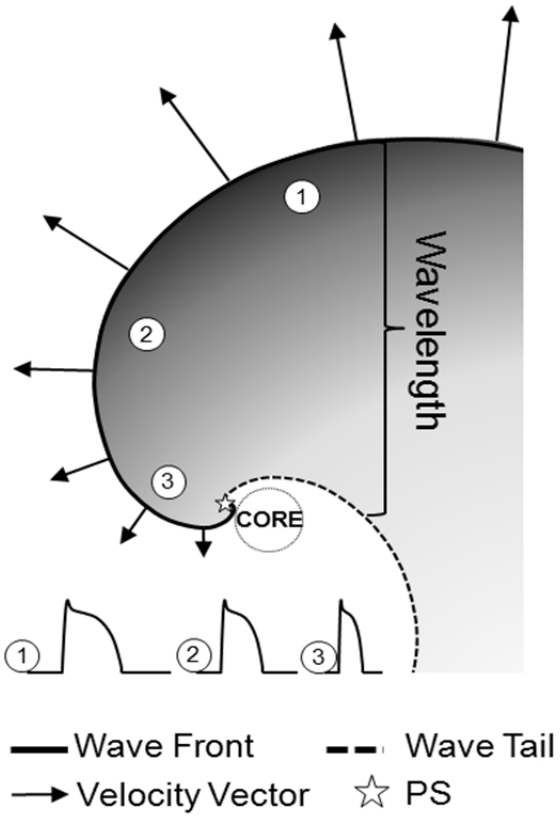

Figure 1.3. Spatial Characteristics of a Rotor. The propagation velocity decreases as the wavefront becomes progressively more convex, reaching critical curvature at the phase singularity (PS), at which point there is no longer perpendicular propagation and the PS circumnavigates an unexcited but excitable core. Action potential duration and wavelength decrease near the core (see text for details). Arrows of different length indicate the direction and velocity of wavefront propagation (the shorter the arrow the slower the velocity). Encircled numbers indicate location of action potential. Adapted from Vaquero *et al.*[60].

A number of genetically modified models have proved useful in elucidating the importance of Kir2.1. Both Kir2.1 knockout mice as well as transgenic mice expressing a dominant negative Kir2.1-AAA subunit, which suppressed I_{K1} to less than 10% of its native levels, demonstrate how a decrease in I_{K1} results in a prolongation of APD, and in the first mouse model it increases spontaneous activity of isolated ventricular cells[89, 90]. APD prolongation, as well as depolarization of the resting membrane potential, and lengthening of the QT interval were observed in a guinea pig model in which adenoviral dominant negative Kir2.1-AAA was expressed[91]. In these larger hearts, Kir2.1 reduction was also associated with arrhythmias, 40% of treated animals having premature ventricular beats. Conversely, adenoviral overexpression of Kir2.1 caused a hyperpolarization of the resting membrane potential, an abbreviation of the APD and a shortening of the QT interval[91].

In addition to models which decrease I_{K1}, Li *et al.*[92] generated 2 viable lines of a transgenic mouse model, in which Kir2.1 with a green fluorescent protein (GFP) tag was overexpressed. Both lines showed cardiac abnormalities. Line 2 had dramatic abnormalities in excitation, having a slowed heart rate, short QT interval, junctional escape, AV block, atrial flutter and sudden death. Line 1 fared better, surviving longer than line 2. However, both lines had a marked increases in I_{K1} current density, a shortening of the QT interval, prolongation of the QRS interval and a reduction in the effective refractory period.

Using the line-1 mice, Noujaim *et al.*[76] further demonstrated that I_{K1} controls rotor and fibrillatory dynamics. In addition to shortening the action potential duration, increases in I_{K1} conductance hyperpolarize the resting membrane potential. This small hyperpolarization has an important

effect on sodium channel availability. During the course of a normal action potential, the sodium channel, being voltage-gated, responds to the initial depolarizing impulse by opening and flooding the cell with sodium. The sodium channel, however, quickly inactivates after only a couple of milliseconds. After this fast inactivation process, the channel then progresses into a number of slow inactivation states which make the channel more difficult to reopen. Both the shortening of the action potential duration, as well as hyperpolarization of the resting membrane potential direct more of the sodium channels into the fast inactivated state. This causes more sodium channels to be easily opened as a depolarizing stimulus approaches. The additional sodium channel availability thus increases the sodium influx, the upstroke velocity of the action potential, and the conduction velocity of the wave. A decrease in the space constant (λ) and a decrease in the size of the core were also observed when I_{K1} was increased; both due to the decrease in electrotonic spread. Additionally, both simulations and experiments yielded an increased conduction velocity near the core when I_{K1} was increased. This study provides mechanistic insight into the role of I_{K1} in the acceleration and stabilization of reentry and VF[76].

1.5 The Delayed Rectifier Potassium Current (I_{Kr} and I_{Ks}) - APD, Post Repolarization Refractoriness and Rotors

Another major ionic component to fibrillatory dynamics is the delayed rectifier potassium current first described by Noble and Tsien[93]. This current is primarily responsible for the late repolarization phase of the action potential and plays a major role in determining the APD. Sanguinetti and Jurkievicz[94] were able to pharmacologically distinguish 2

components of this current; the rapid delayed rectifier current[16] (I_{Kr}) and the slow delayed rectifier current (I_{Ks}). As their names indicate, I_{Ks} kinetics are such that it activates and deactivates slowly, whereas I_{Kr} activates more rapidly and has a prominent inward rectification. Each of these currents is passed through an individual ion channel. I_{Ks} is passed through the K_vLQT1 channel (or Kv7.1, coded by *KCNQ1*) and is associated with an important regulatory subunit minK (coded by *KCNE1*) which reduces the current through K_vLQT1[(95-97)]. I_{Kr} on the other hand is passed through the human ether-a-go-go-related (hERG or Kv11.1) channel, coded by *KCNH2*[(98, 99)]. I_{Kr} has been reported to associate with minK-related peptide 1 (MiRP1, encoded by *KCNE2*) however the physiological importance of this association is still debated, and it appears as if MiRP1 may have a greater functional association with I_{Ks} than I_{Kr}, or it may structurally associate with I_{Kr}[(100-102)]. Both I_{Kr} and I_{Ks} have a major influence over cardiac repolarization and refractory period and have been implicated in a number of arrhythmogenic diseases.

1.5.1 I_{Ks} – Post Repolarization Refractoriness, Rotors and Wavebreak

Mutations in *KCNQ1* (I_{Ks}) have been associated with a number of disease states. Loss of function mutations result a prologation of the APD generating Long QT syndrome (LQT1). Excessive APD prolongation is associated with early afterdepolarization (EAD)-induced arrhythmias[(103, 104)]. Additionally, gain of function mutations have been associated with both short QT syndrome (SQT) and familial AF, or even both in the same patient[(105, 106)]. Similar to APD prolongation, APD shortening is also associated with VF and sudden death.

[16] I_{Kr} was identified as it was selectively sensitive to a benzenesulfonamide compound E-4031 whereas the I_{Ks} component is not.

To better understand the role of I_{Ks} in fibrillatory dynamics Muñoz *et al.*[107] adenovirally overexpressed both *KCNQ1* (I_{Ks}) and *KCNE1* (minK) in a model of neonatal rat ventricular myocyte (NRVM) monolayers which were then optically mapped. This experimental technique uses mechanically and enzymatically dissociated neonatal rat ventricular cells which have been plated such that they create a relatively uniform single layer of myocytes[17] and is an excellent model for investigating electrical propagation as it is able to recapitulate numerous features of both normal propagation and fibrillation[18]. It also is currently the only model which can do this while reproducibly controlling the structure and ionic profiles[19].

Using this model in parallel with single cell voltage clamping experiments and computer simulations Muñoz *et al.*[107] found that I_{Ks} overexpression generated somewhat faster rotor frequencies and shortened APD and wavelength during reentry. On the other hand conduction velocity as a function of distance from the core did not increase as much as in the control monolayers, suggesting a decrease in excitability. As decreases in APD, WL and CV were primarily observed during rotors, but not pacing experiments, their study suggested that I_{Ks} enhances the repolarizing influence of the core in addition to increasing the rate of repolarization of the action potential; this is the suspected mechanism for the small I_{Ks}-induced increases in rotor frequency.

The major effect of I_{Ks} overexpression was on wave propagation dynamics. Unlike the control situation, which generated rotors which

[17] 35 mm diameter monolayers are typically plated with 1-1.2 million cells per Petri dish, discussed further in the methods section of Chapter 2.

[18] This model does have limitations in that it is only a 2D sheet and so lacks 3D structural impact on arrhythmias and due to the immature nature of the cells and their alignment have a reduced I_{K1} and slower conduction velocities than those observed in whole heart models.

[19] Variations on this model using atrial cells or neonatal mouse ventricular or atrial cells are also used to make monolayers.

propagated evenly through the monolayer, rotors generated in the I_{Ks} overexpressing monolayers often underwent a time-dependent generation of wavebreak and formation of new shorter lived rotors. These wavebreaks were first initiated at a distance to the primary rotor, but eventually progressing towards it and finally reaching a steady state of uniform dominant frequency throughout the tissue. Using HEK cells and computer simulations to demonstrate the rate-dependent effects of I_{Ks}[20], they showed how the slow deactivation kinetics of I_{Ks} may be sufficient to induce wavebreak formation in the setting of heterogeneous expression of I_{Ks}.

The role of I_{Ks} in action potential repolarization has been a matter of contention; in humans both loss and gain of function mutations can lead to APD prolongation[103, 104, 108, 109]. However, the slow recovery from inactivation of I_{Ks} has been implicated in a phenomenon of post repolarization refractoriness. Even after the sodium channels have recovered from inactivation after an action potential, I_{Ks} can contribute to an activation failure; the cell has returned to resting potential but has not yet returned to an excitable state. Spatial dispersion of APD and refractoriness has long been identified to play a major role in fibrillatory dynamics[68-70]. Computer simulations establish that spatial dispersion in the excitable state or recovery kinetics may be sufficient to generate wavebreak and fibrillatory conduction. In the study of Muñoz *et al.*, I_{Ks} was shown to have modest effects on rotor frequency, but a major influence

[20] I_{Ks} channels have a number of inactivated states. The first inactivated states can readily transition into an open state, given time channels will transition into other inactivated states which take longer to transition out of and reopen. At slow frequencies the increased time between beats allows more channels to pass into the inactivated states which then take longer to reopen. This reduces the overall I_{Ks} current upon cellular depolarization. At higher frequencies there is less time for a channel to progress into the secondary inactivated states, so upon cellular depolarization more channels can quickly open creating an increased I_{Ks} current.

over fibrillatory dynamics as spatial heterogeneity in I_{Ks} infection leads to temporally dependent fibrillation due to its effect on post repolarization refractoriness.

1.5.2 I_{Kr} – APD, Transient Hyperpolarization and Rotors

Mutations in hERG have been also associated with human short and long QT syndrome as well as heterogeneous APD dispersion[110-112]. Similar to I_{Ks}, I_{Kr} is a voltage-gated potassium channel; however, it has both a rapid activation and inactivation and has an unusual increase of tail current as the cell becomes repolarized. This is due to a voltage-dependent C-type inactivation which limits current at positive voltage but undergoes a rapid recovery from the inactivated state as the cell repolarizes. I_{Kr} plays a major part in cardiac repolarization, increasing the role of the potassium current at a more positive potential than the I_{K1} channel can accommodate.

A recent study from our lab investigated the effect I_{Kr} overexpression had on rotor frequency and stability in the same NRVM monolayer model as Muñoz *et al*. Hou *et al.*[113] observed that I_{Kr} increased rotor frequency, sometimes to values as high as 25 Hz. They found that I_{Kr} overexpression was similar to I_{Ks}, in that during pacing it shortened the APD (although with I_{Kr} it accomplished this at all pacing frequencies, unlike I_{Ks} which only showed APD shortening at low frequencies) and I_{Kr} did not alter CV. During rotors the influence of I_{Kr} and I_{Ks} on APD and WL shortening was similar. However, unlike I_{Ks} overexpression[107] but similar to I_{K1} overexpression[76], I_{Kr} overexpression increased CV as a function of distance from the core of the rotor when compared to controls, suggesting an increase in excitability. Similarly, the curvature of the wavefront was greater. This indicates that I_{Kr}

overexpression plays a role in excitability during rotor activity, in addition to the roles of I_{K1} and I_{Na} previously established.

Patch-clamping and computer simulations demonstrated that I_{Kr} generates both APD shortening as well as a brief overshoot of the resting membrane potential. This suggests that at high enough frequencies this transient hyperpolarization may contribute to an increase in sodium channel availability in a manner similar to that of I_{K1}. In computer simulations, using I_{Ks} overexpression as a control group, we found that I_{Kr} had a greater effect on APD shortening than I_{Ks}. Furthermore, I_{Kr} had a much greater impact on the resultant peak sodium current. Two-dimensional simulations with I_{Kr} overexpression were then used to show how rotor frequency was affected by the transient hyperpolarization. By running simulations which progressively clamped the membrane potential by 1 mV increments from -70 to -66 mV, Hou *et al.*[113] were able to show how the rotor frequency declined from 18.5 Hz to just below 17 Hz. These results demonstrate that both APD shortening and transient hyperpolarization of the membrane contributed to increased excitability, rotor frequency and rotor stability. However, it is worth noting that increases in I_{Kr} do not always generate such a transient hyperpolarization. In isolated canine and rabbit ventricular cells, overexpression of hERG resulted in a shortening of APD but did not produce a reported transient hyperpolarization[114, 115]. This is most likely the result of species specific differences and may shift the relative influence of APD shortening as a mechanism for rotor stabilization to the forefront depending on the model.

While other potassium channels contribute to the action potential, I_{K1}, I_{Ks} and I_{Kr} have each been shown to exert a substantial influence over the mechanisms underlying rotors and the dynamics of fibrillation. Each channel, by way of APD shortening, has an impact on sodium channel availability, the effect being greatest with I_{K1} and I_{Kr} and to a much lesser

extent I_{Ks}. I_{K1} and I_{Kr} have an even greater effect on sodium channel availability by way of hyperpolarizing the membrane potential after repolarization, I_{Kr} transiently and I_{K1} continuously, the net effect being an increased rotor frequency, increased rotor curvature and increased rotor stability[21]. I_{Ks} overexpression, while having only a modest effect on rotor frequency, has a major role in fibrillatory dynamics by way of increasing postrepolarization refractoriness. This serves as a temporally established mechanism of wavebreak under spatially heterogeneous conditions. Together, these repolarizing potassium channels are major regulators of fibrillatory dynamics making them the subjects of much cardiac arrhythmia research.

1.6 Spatial Dispersion of APD and Fibrillatory Conduction

There is both clinical and experimental evidence to support the hypothesis that at least some types of fibrillation result from the activity of a small number of high frequency rotors localized in one cardiac chamber (atrium/ventricle)[22], with fibrillatory conduction extending into the other chamber[(55, 57, 116)]. While previous sections of this chapter have provided mechanistic insight into the establishment of rotors, emphasizing the roles of I_{K1}, I_{Ks} and I_{Kr} in this process[23], little attention has yet been paid to the other major dynamic process observed during fibrillation, the irregular and

[21] Even though I_{Ks} was shown in simulations to modestly increase sodium channel availability (Hou *et al. 2010*) the effect on post repolarization refractoriness appears to have a greater influence on rotor frequency causing a net decrease in CV near the core compared to controls (Muñoz *et al. 2007*).

[22] Not all clinical and experimental evidence has found a stable rotor driving fibrillation, but there is enough evidence to say it is certainly a mechanism driving some types of fibrillation.

[23] In the interest of brevity the roles of I_{Na} and I_{Ca} in rotor stabilization were not addressed. Beaumont *et al.* (1998), Mandapati *et al*.(1998) and Starobin *et al*. (1996) have investigated the role of I_{Na} in the stabilization of rotors, while Samie *et al*. (2000) demonstrated how I_{Ca} blockade stabilized reentry, reducing DF and wavebreak.

complex behavior of fibrillatory conduction. The predominant explanation for the generation of fibrillatory conduction is that there are inherent structural and electrical heterogeneities[24] throughout the heart which disrupt propagation and lead to wavebreak, rotor initiation and an overall destabilization of uniform propagation.

A lot of work has been done investigating the effects of structural heterogeneities. However, it has only been recently, with the development of many molecular, genetic and imaging techniques, which much examination of the regional ionic heterogeneities and their role in fibrillation has begun. So far, evidence suggests that regional heterogeneities in the ionic profiles of neighboring tissues may be just as important to our understanding of cardiac arrhythmias as the role of structural heterogeneities.

It is clear from the observations of different types of fibrillation, in both human and animal models, that there are regional domains which reproducibly create distinctive fibrillatory patterns. In 2000, Zaitsev *et al.*(117) demonstrated, in sheep ventricular slabs, that the dominant frequency (DF)[25] of excitation does not change within specific regions of the tissue. In 2001, Samie *et al.*(57) used Langendorff-perfused guinea pig hearts, further demonstrating that DFs were clearly distributed throughout the ventricles in specific domains. The highest DFs localized within the left ventricle (LV) and the slower DFs localized to within the right ventricle (RV). They found that the highest frequency region corresponded to the

[24] Temporally established heterogeneities such as alternans have also been regarded as a mechanism which can contribute to patterns of fibrillatory conduction.

[25] Dominant Frequency is another analytical tool used in the investigation of cardiac arrhythmias. A fast Fourier analysis of the optical signal from a given pixel's recording generates the frequency spectrum; the frequency with the most power is considered the dominant frequency (DF). This is not to be confused with the maximal dominant frequency which is the highest dominant frequency within a given region of pixels/tissue.

site of a stable rotor and demonstrated how block and wavebreak occurred at the boundary between frequency domains. In addition to this observation, patch-clamp studies and computer simulations led to the proposal of a molecularly based mechanism for this regional pattern of fibrillatory dynamics.

As previously discussed, I_{K1} plays an important role in the stability and frequency of rotors, thus it stands to reason a region of tissue with increased I_{K1} would have a stabilizing effect on rotors. Samie *et al.*[57] found that there are significant differences in the outward conductance of the I_{K1} current between left and right ventricles; being almost 1.5 times greater in the left ventricle. The increase in I_{K1} results in a regional shortening of the APD. Computer simulations which implemented this APD heterogeneity, found that the higher level of I_{K1} in the LV was able to generate and maintain rotors while the lower level of I_{K1} in the RV was not able to sustain rotors due to wavefront-wavetail interactions. A simulation combining a central square of LV modeled tissue in a larger region of RV modeled tissue replicated both the regional frequency domains seen in experiments, but also the behavior of a rotor surrounded by patterns of fibrillatory conduction generated at the boundaries between the two tissue types.

Further investigation by Warren *et al.*[118] demonstrated the regional effects of I_{K1} on the DF and regional organization of VF. In addition to confirming the regional increase in the outward component of I_{K1} within the LV, Warren *et al.* found that there was an increase in both Kir2.1 and Kir2.3 mRNA within the LV; Kir2.1 almost doubled and Kir2.3 increased 1.5 times. The application of barium (an extracellular blocker of I_{K1}) reduced fibrillatory frequencies unevenly in the heart, the regional LV-RV DF dispersion dropping from 15 Hz to 1 Hz. Additionally, barium perfusion

resulted in a reduction in the number of frequency domains, in essence organizing the fibrillatory behavior. This suggests that heterogeneity of I_{K1} is, at least in part, responsible for the increased in the complexity of the arrhythmia seen before the application of barium.

Sekar *et al.*[119] further investigated the role of regional I_{K1} heterogeneity in rotor initiation and stabilization. A stenciled NRVM monolayer model was used to create a central region (6 mm diameter) of lentivirally transduced cells, over and around which a layer of non-transduced cells were plated one day later (12-17 mm diameter). This model generated a gradient in ionic heterogeneity of about 50 μm. Using lentiviral vectors for Kir2.1 and a dominant negative Kir2.1AAA, Sekar *et al.* found that a stimulated pulse in homogenous monolayers propagated uniformly and did not generate rotors. On the other hand, heterogeneous preparations showed changes in CV which corresponded to the amount and region of I_{K1} and, unlike controls, did generate rotors.

Upon the induction of a rotor, in either of the heterogeneous conditions, it tended to circle around the region of heterogeneity with either the tip locating just inside or just outside the boundary. This is the first experimental model to investigate heterogeneous ion channel expression in a controlled and relatively[26] uniform model and its role in rotor dynamics; and with it they have demonstrated that regional Kir2.1 heterogeneity is proarrhythmic.

It is clear that heterogeneous ion channel expression is an important modulator of electrical propagation as well as dynamic

[26] A consideration for this paper is that their model introduces a certain amount of structural heterogeneity as the central region of cells is getting covered by a second layer of cells, of course not all of these cells integrate with the central region, but it is clear from their images that enough survive the process for it to be a potential concern when interpreting their results on the basis of purely ionic heterogeneity.

fibrillatory behavior. However, detailed knowledge as to the character of the various ionic gradients has only barely begun and there is much yet to be fully described. Most often there are characterizations of regional current, protein or genetic transcripts available for a given current. However, I have yet to come across information describing the native spatial profile of any ionic gradients. In addition to regional heterogeneity of ion channels there is still much to consider by way of their regional association with regulatory units, signaling pathways and the interactions of multiple ionic gradients. These interactions have not yet been fully described, nor has the impact these gradients may have on fibrillation. In addition to the native regional ionic heterogeneities, it is likely that under pathological conditions these gradients can become altered. Such alterations to ionic gradients may have consequences for fibrillatory dynamics in certain disease states[120]. Grasping the significance of these physiological and pathophysiological cardiac heterogeneities may provide insight into the mechanisms and hopefully the treatments of arrhythmias. Below is a brief summarization describing what is known about the heterogeneity of some of the major potassium currents in the heart[27].

1.6.1 Regional Heterogeneity in Inward Rectifying Potassium Channels

Rectification is a non-ohmic current voltage (I-V) relationship, such that a channel's conductance changes with the voltage; the ion channel preferentially allows current to pass in one direction[121]. There are 3

[27] VF and AF are associated with a number of disease states nearly all leading to alterations in one or a number of ion channels and their expression patters. In this chapter I will only include some of the potassium channel changes associated with some of the major disease states.

primary inward rectifying potassium channels in the heart, two strongly rectifying, I_{K1} (Kir2.x) and I_{KACh} (Kir3.x), and one weakly rectifying, the I_{KATP} (Kir6.x) channel.

1.6.1.1 Regional I_{K1} Channel Heterogeneity

As discussed above, there are regional LV-RV differences in Kir2.1 and Kir2.3 and associated LV increases in I_{K1} in the guinea pig heart[57, 118]. Additionally, in the mouse, LA-RA and ventricular apical-endocardial gradients in I_{K1} exist. In the ventricles of this model, the RV tends to have an increase in inward I_{K1} compared with LV[89, 122]. In the feline, LV endocardial tissue has more inward and outward I_{K1} compared to epicardial tissue[123]. There is also I_{K1} heterogeneity between the LA and pulmonary veins (PV) in the canine[124]; PV I_{K1} density reduced by about 58% of the LA[125]. This region is of particular interest to researchers and clinicians, as it has been implicated in the mechanisms of atrial fibrillation. Ablation around the PV is often effective at terminating the arrhythmia, the thought being that it is preventing spontaneous beats from the PV from disrupting the normal activation of the atria. However, it may be the case that the regional ionic heterogeneity between these regions also contributes to a substrate for wavebreak and fibrillatory conduction.

Given the number of changes to I_{K1} which occur in different disease states, it is also likely that these regional ionic gradients will be altered. Atrial I_{K1} is increased in patients with chronic AF[126, 127]. In chronic heart failure (CHF) there is some evidence to suggest ventricular I_{K1} is reduced, although the results are not consistent[126, 128-131]. In the atria of chronic heart failure patients, a condition often associated with atrial fibrillation, atrial I_{K1} was reduced[132], but no changes were observed in a canine

model of CHF[133]. In a feline model of right ventricular hypertrophy, increases in I_{K1} were seen in the RV[134], but LV hypertrophy did not increase I_{K1} in the LV[135]. It is likely that under pathological conditions regional I_{K1} gradients become altered which may have an important effect on fibrillatory dynamics[120] . Understanding such changes to I_{K1} gradients may even shed light onto the progression of certain cardiac diseases, making regional I_{K1} heterogeneity an area deserving of further study.

1.6.1.2 Regional K_{ATP} Channel Heterogeneity

The K_{ATP} channel is a weakly rectifying potassium channel that is activated by adenosine di-phosphate (ADP) under conditions of metabolic stress such as during ischemia when adenosine tri-phosphate (ATP) is decreased; the primary result of sustained VF. The K_{ATP} channel is not primarily involved in the action potential under normal conditions, but it is involved in the progression of ventricular fibrillation as the heart becomes metabolically strained. The K_{ATP} channel, when activated, plays an important role in shortening the APD and has been associated with a number of regional heterogeneities. Endo-to-epicardial heterogeneity has been found in the LV of cardiomyopathic human hearts[136] among other models[137, 138], as well as between the LV and RV. In cardiomyopathic human hearts the K_{ATP} channel's gene expression, Kir6.1 and Kir6.2, as well as its accessory subunits, SUR1 and SUR2, were decreased by about 40% within the epicardium[136]. Blockade of the channel significantly reduced effective refractory period heterogeneity during ischemia. In addition to edo-epicaridal heterogeneity there is also LV-RV heterogeneity which has been demonstrated in the guinea pig[139]. During ischemia glibenclamide (an I_{KATP} blocker) abolished a prominent 28.4 ms APD_{70}

gradient. Additionally, the LV had higher mRNA levels of K_{ATP} channel genes; Kir6.1 was increased to 136% of its expression in the RV and Kir6.2 was 44% more abundant[139]. In addition to heterogeneous expression of K_{ATP} channel, it has been observed to respond more sensitively to ATP reduction in epicardial cells compared to endocardial cells[138]; this further illustrates the levels of complexity which control the function of a given region of cardiac tissue.

1.6.1.3 Regional K_{ACh} Channel Heterogeneity

I_{KACh} is an acetylcholine (ACh) activated inward rectifying potassium current. I_{KACh} has been implicated in the control of regional AF frequencies. A number of publications have identified that AF in the presence of ACh is maintained by fast rotor activity within the LA which emanates into the lower frequency patterns of fibrillation in the RA[140-143]. In an ACh-dependent manner, Sarmast *et al.*[142] were able to reveal a chamber specific increase in frequency. Both chambers resulted in faster frequencies, but the LA was faster at each increasing level of ACh. Additionally, this regional DF sensitivity to ACh was associated with an increase in LA mRNA expression of Kir3.1 and Kir3.4 which compose the channel pore, as well as a LA increase in I_{KACh}[142]. A study by Voigt *et al.*[84] examined LA-RA heterogeneity in I_{KACh} in cells from patients with sinus rhythm, paroxysmal AF and chronic AF. In sinus rhythm RA I_{KACh} was 70% greater than in the LA, during PAF and CAF a reduced in I_{KACh} was only observed in the RA. Similarly, protein levels of Kir3.1 and Kir3.4 were greater in the RA during sinus rhythm and were decreased in PAF and CAF. Taken together, these results strongly point to regional I_{KACh} heterogeneity as an important modulator of AF dynamics.

1.6.2 Regional Heterogeneity in Delayed Inward Rectifier Potassium Channels

1.6.2.1 Heterogeneity of the Slow Delayed Rectifier Current - I_{Ks}

Regional heterogeneities in I_{Ks} have been observed in the mouse with a decrease in I_{Ks} in the endocardial compared with epicardial cells in the LV[122]. In the canine I_{Ks} is smaller in the LA than PV[124, 125]. In canine ventricle there is a reduction of I_{Ks} in the mid-myocardium[144], however in the guinea pig it is increased in both the mid and sub-epicardium compared to the sub-endocardium[145].

1.6.2.2 Heterogeneity of the Rapid Delayed Rectifier Current - I_{Kr}

I_{Kr} heterogeneity is found transmurally and from apex to base in the ventricles of ferret hearts[146]. hERG heterogeneity is also found transmurally in basal LV tissue of guinea pig hearts[145], as well as epi-endocardially in the canine ventricle[144, 146] and in a canine wedge preparations modeling LQT2[114]. In canine atria, I_{Kr} is greater in the PV than LA[124, 145, 147]. I_{Kr} is also greater in the LA than RA of the canine[148].

From this brief summary of potassium channel heterogeneity, it is clear that the heart is an incredibly complex and regionally heterogeneous tissue. Ion channels, excitability, APD and refractoriness, all have an important impact on propagation and thus fibrillatory dynamics. However, there is a long way to go to understand the specific contributions of any given ionic heterogeneity, let alone multiple overlapping heterogeneities, as they impact the mechanisms of arrhythmias. The pure magnitude of

complexity of regional ion channel heterogeneities in the heart and their un-elucidated role in fibrillation is a significant topic of study which deserves further investigation.

1.7 Summary

Over the last few centuries, tremendous advancements in our understanding of cardiac arrhythmias have occurred; however despite the laudable progress, atrial and ventricular fibrillation remain complex phenomenon whose mechanisms are not fully understood. Advances in high-resolution mapping technology, electrophysiology, molecular biology and genetics, together with the awareness that fibrillation in the atria or ventricles can result from electrical derangements caused by mutated and/or heterogeneously expressed ion channels[57, 76, 85, 88, 142], has opened new avenues for research on the subcellular mechanisms of these two complex, life-threatening clinical arrhythmias. The manner in which different ionic currents contribute to the control of normal and abnormal electrical wave propagation is now being successfully investigated at various levels of integration, from the molecular to the organ levels [76, 84, 107]. To date, most of these studies have led to the recognition that often during fibrillation, the normal electrical activation of the heart is replaced with patterns of reentry, wavefront fragmentation or wavebreak and fibrillatory conduction which prevent normal cardiac function [84, 141, 143, 149, 150].

However, we are still at a point where the demonstration of the direct mechanistic link between molecular influences and the dynamics of fibrillation has only just begun. The work presented in this thesis aims to add to our understanding of some of the ionic mechanisms behind

patterns of wavebreak and fibrillatory conduction. In the following chapters I provide data demonstrating how regional heterogeneity in the expression of the two major repolarizing potassium channels I_{Kr} and I_{K1} contribute to fibrillatory dynamics through similar but individual mechanisms using a novel regional magnetofection technology. Further study of cardiac arrhythmias, particularly concerning the integration of information from genetic, molecular, ionic, whole organ and systematic levels, can only improve our understanding of the pathophysiology of the human heart and hopefully teach us how to prevent and/or treat cardiac arrhythmias and improve patient care.

Chapter II

Spatial Gradients in Action Potential Duration Created by Regional Magnetofection of hERG are a Substrate for Wavebreak and Turbulent Propagation in Cardiomyocyte Monolayers[28]

2.1 Introduction

Clinical and experimental evidence supports the hypothesis that fibrillation results from activity of a small number of high frequency reentrant sources (rotors) localized in one cardiac chamber (atrium/ventricle), with fibrillatory conduction to the other chamber[57, 116]. As shown in animals and in man, waves emanating from rotors propagate throughout the atria or ventricles where they undergo intermittent block and wavebreak generating highly complex patterns of local electrical activation[7, 116]. The latter phenomenon, which resembles turbulence in water, is known as "fibrillatory conduction"[37]. Arguably, understanding the ionic mechanisms involved in the formation of wavebreak and fibrillatory

[28] © 2012 Journal of Physiology

conduction should prove useful in developing therapies to prevent and/or terminate life-threatening tachyarrhythmias.

Spatial dispersion of cardiac electrophysiological properties likely plays a major role in establishing spatially distributed gradients of fibrillatory frequency across the cardiac chambers. More specifically, during fibrillation, chamber specific differences in excitability, action potential duration (APD) and refractoriness are likely to be the cause of stabilization of rotors in one cardiac chamber with fibrillatory conduction in the other[57]. Sarcolemmal potassium currents are known to be strong modulators of excitability, APD, rotor frequency and ventricular fibrillation (VF) dynamics[57, 76, 107]. The inward rectifying potassium current (I_{K1}) and its spatial heterogeneity, are thought to play important roles in the mechanisms of rotor stability and frequency in the atria[124] and the ventricles[57, 76]. On the other hand, overexpression of the slow delayed rectifier current (I_{Ks}) was found to increase fibrillatory conduction in cardiomyocyte monolayers while not increasing rotor frequency[107]. More recently, we investigated the consequences of overexpressing the alpha subunit of the human ether-a-go-go-related (hERG) channel, coded by *KCNH2*, which is responsible for the rapid delayed rectifier current (I_{Kr}) and helps to establish the action potential duration and morphology. We showed that I_{Kr} upregulation increases rotor frequency in a manner that depends on its APD shortening effects[113]. Mutations in hERG have been associated with human short and long QT syndrome and heterogeneous APD[110-112]. On the other hand, viral transfer of the *KCNH2* mutant G628S associated with long QT syndrome eliminated AF in porcine model by prolonging atrial APD[151]. I_{Kr} heterogeneity is found transmurally and from apex to base in the ventricles of ferret hearts[146]. It is also found transmurally in basal LV tissue of guinea pig hearts, and in canine wedge

preparations modeling long QT syndrome type 2 (LQT2), as well as between the pulmonary veins and left atria in the canine[124, 145, 147].

Here we focus on the role of spatial APD heterogeneity in the mechanisms of wavebreak and fibrillatory conduction. Since I_{Kr} is important in the control of the APD, and APD dispersion is thought to be important in cardiac fibrillation, we surmised that generating hERG gradients in a well-controlled environment may recreate the arrhythmogenic substrate that results in wavebreak and rotor formation.

Our central hypothesis is that in the presence of a spatial APD gradient, wavebreak and fibrillatory conduction occur when high-frequency waves generated in the short APD region propagate toward, and impinge on the boundary with the long APD region, but not the reverse.

To test this hypothesis, we used heterogeneous hERG expression as a tool and reduced the complex problem of fibrillatory propagation in the 3-dimensional heart to a 2-dimensional model. We used a novel regionally heterogeneous magnetofection of adenovirus containing the hERG cDNA sequence into neonatal rat ventricular myocyte (NRVM) monolayers. The results may provide important information about the nature of arrhythmias in the heart and how we may better prevent and treat them in future.

2.2 Materials and Methods

2.2.1 Ethical Approval

All experiments were approved by the University Committee on the Use and Care of Animals (UCUCA) at the University of Michigan, and the

Department of Laboratory Animal Resources. All euthanasia was performed following the recommendations of UCUCA and DLAR-CHUA. All mother rats were either donated to the university “rat recycling program” for use by other investigators, or euthanized by placing the rat in a carbon dioxide filled chamber, followed by removal of a vital organ (e.g., heart). The neonatal rats were euthanized by quick decapitation.

2.2.2 Myocyte Isolation and Culture

We created neonatal rat ventricular myocyte (NRVM) monolayers as previously described[107, 152]. Ventricles from 1-2 day old neonatal Sprague-Dawley rats (Charles River, Wilmington, MA) were aseptically removed then minced in calcium- and magnesium-free Hanks’ Balanced Salt Solution (HBSS, Sigma). Sequential digestion in 0.06% trypsin (Roche Applied Science) and 0.15% pancreatin (Sigma) in HBSS at 36°C was used to further isolate cells. A two hour differential preplating period was used to reduce the presence of non-cardiomyocytes. Medium M199 (Cambrex) containing 10% fetal bovine serum (FBS, Cellgro), 20 U/mL penicillin, 20 µg/mL streptomycin and 100 µmol/L bromodeoxyuridine to inhibit fibroblast proliferation (Sigma) was used to suspend and plate cells. Cells were plated on human collagen type IV (Sigma) coated 35 mm tissue culture dishes at a density of $1x10^6$ cells per monolayer. Cells were kept at 37ºC, 5% CO_2. Media was changed after 24 and 48 hours using the same 5% FBS media. Magnetofection was performed on day 2 in culture. Experiments were conducted at an additional 48 hours, allowing for protein expression.

2.2.3 Magnetofection

Magnetic nanoparticles (MNP), such as ViroMag magnetic beads, are a relatively new product primarily used for increasing infection efficiency[153]. MNPs are small (typically 50-500 μm in diameter) iron oxide molecules which have been stabilized with a coat of biocompatible polymers chosen to bind different gene transfer vectors[154]. The MNPs are then complexed with the gene transfer vectors (for our experiments adenoviral vectors) and then added to a dish of cultured cells. At this point the cells are placed over a magnetic plate for a short period of time, the solution is changed and the cells can be cultured. MNPs are primarily designed to increase the efficiency of gene transfer into cells which are not easily infected or for instances of a small stock of virus. The primary mechanism believed responsible for the effectiveness of magnetic nanoparticles is accelerated sedimentation[155, 156]. That is, the MNPs are efficiently directing the adenoviral vector to the cell membranes. After being brought quickly to the cell, the virus enters through its normal mechanism of coxsackievirus and adenovirus receptor (CAR)-mediated endocytotic internalization[157].

While our project utilized adenoviral mediated MNP gene transfer, other MNPs have been designed to bind lentiviral vectors, DNA plasmids, siRNA and lyposomes[155]. There is evidence that for MNPs designed to bind DNA vectors, the mechanism of internalization is endocytosis, likely mediated through caveolae and clathrin-dependent means[156]. However, some research has found that adenovirus-bound MNPs can infect cells which have little or no CAR receptors[158]. This suggests that MNPs may also provide alternative mechanisms of adenoviral internalization which have not been fully elucidated. However, once inside the cell the adenovirus will proceed as if it were a normal infection process. DNA will be extruded into the nucleus where it will lead to the overexpression of the specified protein[157].

The MNPs are then relegated to endosomes or lysosomes within the cell[155]. MNPs are primarily composed of iron oxide which is then easily degraded by the cell into free iron and slowly released into the cytoplasm[155]. The use of MNPs has the potential for cellular toxicity as they can result in the excess production of reactive oxygen species (ROS) and free radicals such as superoxide anion, hydroxyl radicals and non-radical hydrogen peroxide[155, 159, 160]. However, such cellular toxicity occurs in a dose dependent manner[155, 161, 162]. In these experiments we did not asses these markers of toxicity for two reasons. The first is that the product information for ViroMag suggests a therapeutic range of 10-120 µl of ViroMag per 0.4-1x10^6 cells, at which they have not found any toxic effects. We used 20 to 240 times less than their suggested range; finding that 0.5 µl of ViroMag per 1-1.2x10^6 cells was more than sufficient for our infection. The second and more convincing reason is that we saw no significant difference in cellular morphology, APD, CV, rotor frequency or behavior between our uninfected or wholly or regionally GFP infected monolayers. Taken together this strongly suggests we are not using enough magnetic nanoparticles to elicit any toxic effects on the cells.

A non-trivial amount of work was necessary for the determination of the ViroMag and virus concentrations as well as the duration of exposure to magnetic field for these experiments[29]. Each of these parameters was determined to be optimal when uninfected regions did not express GFP fluorescence while maintaining infection within infected region.

Magnetofection was performed on day 2 in culture. We infected monolayers with either an adenovirus containing fused cDNA sequence of human ether-a-go-go-related gene (hERG) with green fluorescent protein

[29] I also was able to develop several techniques to control the width and shape of the gradient within certain parameters.

(GFP) sequence (Ad-hERG-GFP) created by Dr. Zhengfeng Zhou [113, 163] or just the GFP sequence (Ad-GFP)[113]. Only the α-subunit of the I_{Kr} channel was included in the virus.

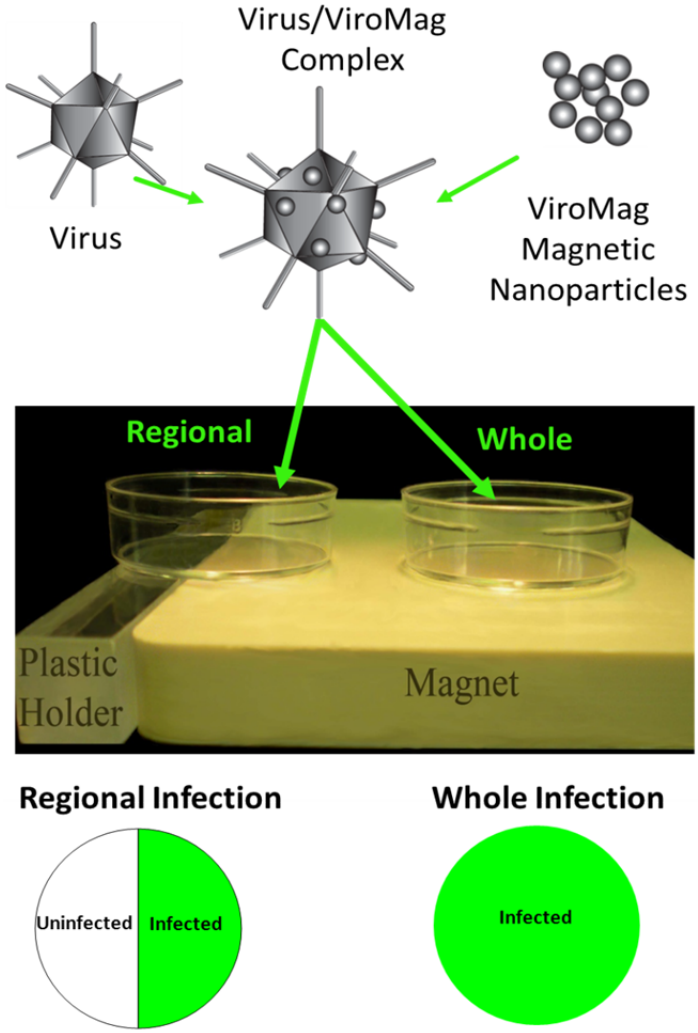

Figure 2.1. Whole and Regional Magnetofection Schematic. Adenoviral constructs bind with the Viromag magnetic nanoparticles to form a complex. The complex is then added to a monolayer. Right: A wholly infected monolayer is generated by adding the complexed ViroMag and virus to the NRVM monolayer placed entirely over the super magnetic plate. Left: A regionally infected monolayer is generated by adding the same complexed ViroMag and virus to a monolayer which is only regionally exposed to the magnet. In both instances the magnetic nanoparticles tug the virus to the area of cells which is placed over the magnet.

Each virus was first complexed to ViroMag Magnetofection nanoparticles (Boca Scientific, FL); a product normally used for increasing infection efficiency[153]. 0.5 µl of ViroMag was complexed with $1x10^8$ viral particles in 200 µl HBSS (Sigma) for 15 minutes then raised to a final transduction volume of 2 ml per monolayer. As illustrated in Figure 2.1, each monolayer was exposed to a Super Magnetic Plate (Boca Scientific, FL) for 1.5 ± 0.5 minutes in the presence of the magnetofection solution. Wholly infected monolayers were placed entirely over the magnet while regionally infected monolayers were created by exposing only half of the lower surface area of the dish containing the monolayer to the magnet. The magnetofection solution was then removed and monolayers were washed twice with and returned to 5% FBS media and given an additional 48 hours to express protein. Uninfected controls were treated similarly using HBSS for 1.5 ± 0.5 minutes.

2.2.4 Optical Mapping

Experiments were conducted at an additional 46-50 hours after magnetofection. Monolayers were stained with potentiometric dye di-8-ANEPPS (40 µmol/L; Molecular Probes) for 15-25 minutes and then placed on a heating chamber connected to a temperature controller maintained at 37 ± 1°C and continuously superfused with HBSS without bicarbonate (Sigma) containing (in mmol/L): 1.6 $CaCl_2$, 5.4 KCl, 0.8 $MgSO_4$, 0.4 KH_2PO_4, 4.2 $NaHCO_3$, 136.9 NaCl, 0.3 $NaHPO_4$, 5.5 D-Glucose, and 10 HEPES; pH 7.4 (NaOH) (Figure 2.2). Quiescent monolayers received repetitive stimuli (duration, 5 ms; strength, twice diastolic threshold) applied by a thin extracellular bipolar electrode at

increasing frequencies, starting at 1 Hz, until loss of 1:1 capture or initiation of sustained reentry. Five-second high resolution optical mapping movies were obtained at 200 frames/s (LabWindows Acquisition) using an 80 × 80 pixel CCD camera (SciMeasure Analytical Systems; Decatur, GA). Signals were amplified, filtered, and digitized for offline analysis. No electromechanical uncouplers were used.

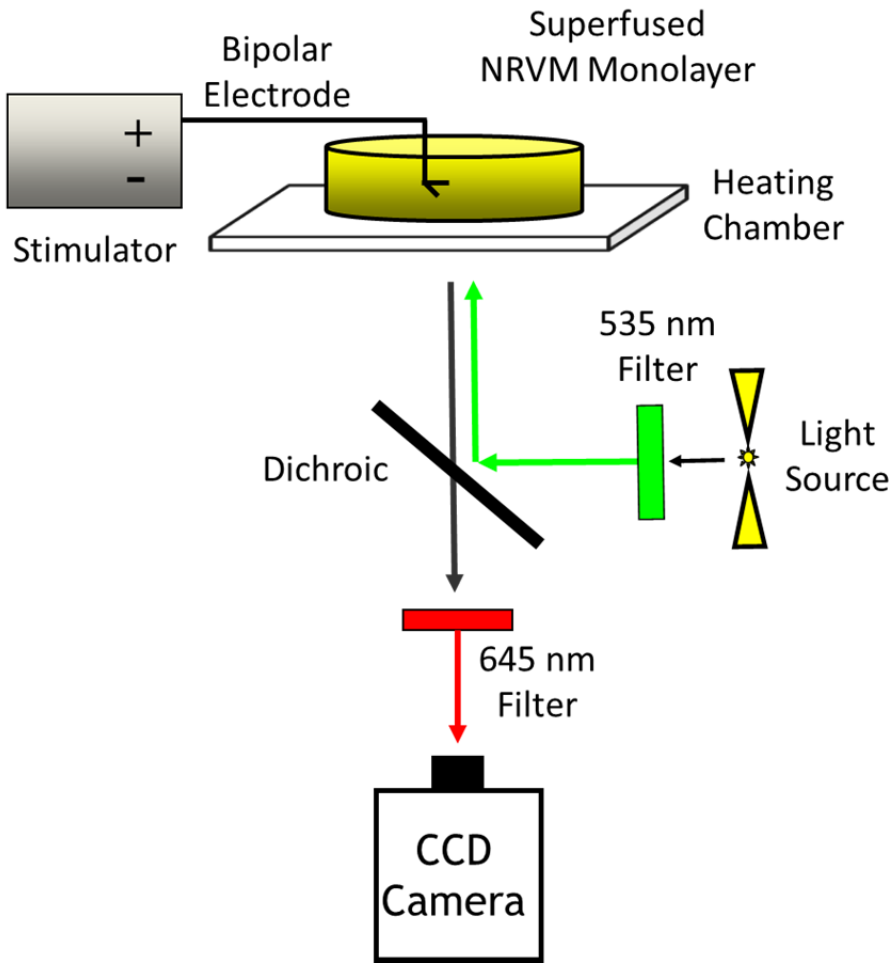

Figure 2.2. Schematic of Optical Mapping Apparatus. (See text for details.)

2.2.5 Optical Data Analysis

Dominant frequency (DF) maps were constructed by taking the Fast Fourier Transformation of the fluorescence signal at each pixel[117, 164, 165]. APD and conduction velocity (CV) measurements used average signals obtained from individual 5 second optical movies recorded during repetitive pacing at varying frequencies. Movies were filtered as previously described[113]. APD color maps were constructed by measuring the time between the upstroke and 50 and 75% of repolarization in each pixel. For CV measurements, activation times were calculated for each pixel, and local conduction vectors were determined as described[113]. The activation ratio (AR; dubbed n:m ratio) is a ratio between the number of activations in the uninfected to the infected regions. Thus n:m was calculated as the number of activations in the distal or uninfected region of the monolayer (n) divided by the number of activations at the proximal or infected region (m). The number of activations in a given region was determined by three 1 second time-space plots (TSP) taken along parallel lines at ¼, ½ and ¾ of the way within each dish perpendicular to the gradient. During rotor analysis in the wholly uninfected and infected monolayers, distal and proximal regions were arbitrarily assigned; in regional infections distal refers to uninfected region and proximal refers to infected regions. Average DF and regularity index (RI) maps and their respective standard error maps were created in Matlab (Mathworks, Natick MA).

2.2.6 Fluorescence Microscopy

We imaged monolayers on day 4 in culture before optical mapping using a Nikon Eclipse Ti confocal microscope. Composite images were taken over 9 x 14 mm; length perpendicular to the gradient.

Images were analyzed in Matlab and best fits were determined using Origin 7.0.

2.2.7 Statistical Analyses

For statistics we used one-way ANOVA with a Bonferroni correction (Origin software version 7.0). Values are expressed as mean ± SEM. A value of $p<0.05$ was considered significant. Contingency table tests and χ^2 analysis were conducted where appropriate. N refers to the number of dissociations and n refers to the number of monolayers.

2.2.8 Computer Simulations

We used a mathematical model for the NRVM adapted to experimental data, as previously described in detail[113], with minor modifications. A 2-dimensional (2D) disk-shaped sheet used a Cartesian mesh of 352 x 352 nodes with a spatial resolution of 100 μm that contains a 35 mm diameter disk-shaped active domain in its center, with a non-diffusive outer domain boundary was used to simulate a NRVM monolayer of tissue. The area outside of the monolayer (the black peripheral region) was implemented with passive and non-diffusive nodes for ease of integration. The membrane model at each node was solved by the finite volume method with a time-step of 10 μs and no-flux boundary conditions, as described previously by Zlochiver *et al*.[166] G_{Kr} maximal conductance was either set as homogeneous (whole G_{Kr}, 1xG_{Kr}–uninfected or 5xG_{Kr}–infected) or varied spatially across the model (regional G_{Kr} model). To simulate the spatial gradient in G_{Kr} expression along the model we implemented the Boltzmann best fit of the hERG-GFP fluorescence data obtained in the experiments for all the groups (Figures 2.3B and 2.13). A native level of G_{Kr} was used in the 'uninfected' region (1x). G_{Kr} was increased over a range of 1 to 20 times basal levels within 'infected region'

of the model. Reentry was induced via S1-S2 cross-field stimulation protocol. DF, DF profiles and n:m ratios were determined as in experiments (See the Appendix for further details).

2.3 Results

2.3.1 Regional I_{Kr} Expression Model

Understanding the mechanisms of how regional hERG heterogeneity influences fibrillatory dynamics is a complicated problem, a problem which was compounded by the fact that when beginning this project there were no adequate models available. Solving this technical issue was a major aspect of my thesis project. In order to study the effects regional hERG heterogeneity we needed a model where we could avoid any confounding influence from the numerous structural and ionic heterogeneities which exist in the whole heart. We needed a structurally homogeneous tissue where we could control regional ion channel heterogeneity. The first part can be answered by using a well-established model of cardiac arrhythmias the NRVM monolayer. They provide a structurally and functionally homogenous layer of tissue. As for the second part of our model requirements, I devised a number of different techniques and created several devices which would allow us to controllably overexpress hERG, each method having varying levels of success[30].

[30] A dual system to allow regional drug perfusion was somewhat successful in creating regional electrical heterogeneity. Several models using a barrier during infection also had a moderate degree of success. Barriers made of thin and very soft agarose gel intended to have a slight contact with cells and create a sealed barrier almost always created damage to the cells even though it generated a good regional infection. Cellophane

In the end we developed a method which took advantage of the magnetic properties of magnetic nanoparticles. As described in the methods section we used magnetic nanoparticles to bind to our adenovirus. Once bound the magnetic beads will bring the attached virus to any area of our monolayer exposed to a magnetic plate. This novel technique allows us to generate regionally controlled areas of hERG overexpression while maintaining a structurally homogeneous layer of functioning cardiac tissue.

Our novel technique of regional magnetofection allows for the creation of confluent, electrically-coupled monolayers with regional differences in hERG channel expression. Figure 2.3.A shows a representative fluorescence image across 16 mm at the center of a regionally infected monolayer expressing GFP tagged hERG channels (Ad-hERG) in the left side only. In B, the non-uniform hERG expression across 6 monolayers follows a characteristic Boltzmann distribution with a gradient at the center of the monolayers; best fit of the averaged fluorescence showed approximately 4 times more fluorescence in the infected than uninfected region, and a slope factor of 0.97 ± 0.12 mm at the gradient location (border zone). In C, contrast-micrographs from the infected and uninfected regions confirm the presence of uniform NRVMs confluency and distribution across the monolayer.

To characterize the electrophysiological properties of regional hERG overexpression we optically mapped our monolayers. We used a

---

barriers designed to fall about 1 mm or less above the cells did not damage cells but allowed for an inconsistent perfusion of the virus into the uninfected region whenever there was a slight perturbation of the monolayer. Tilting the monolayers at an angle during infection proved the most effective alternative method for creating a gradient in overexpression. However, it did not sufficiently generate 3 distinct regions of electrical heterogeneity rather it created a long gradient across the monolayer. Regional magnetofection gave us the most controllable regional infection.

bipolar electrode in the infected region to pace the monolayers. The APD map shown in Figure 2.4.A confirms that regional Ad-hERG infection generates well demarcated APD heterogeneity with an APD_{75} gradient of 16.6 ± 0.72 ms. In B, the average and best fit for both fluorescence (grey lines) and APD_{50} (black lines) as a function of distance have been represented, where 0 mm is the central location within the monolayer. Representative optical action potentials and average APD_{50} and APD_{75} values (Figure 2.4C) demonstrate that the regional infection generated significant APD heterogeneity. The upstroke velocity of these traces was significantly faster than repolarization. Having demonstrated that regional hERG overexpression results in a regional change in the APD of the infected tissue we compared our APD results with our control groups during pacing. In the top graph of panel D, APD_{75} was the same in the uninfected (UN) and whole-Ad-GFP infected (W-GFP) monolayers, while the APD_{75} in the whole-Ad-hERG (W-hERG) monolayers was significantly shorter than the other two. In the bottom graph, APD_{75} in the infected region of the regionally infected hERG (R-hERG) monolayers was significantly shorter than the infected region of the regionally infected GFP (R-GFP) monolayers. We did not observe any regional APD differences within UN, W-GFP, R-GFP or W-hERG and we observed a non-significant APD difference between the R-GFP and UN groups was observed. Analysis of APD_{50} showed similar results. Additionally, optical mapping based analysis of wave propagation in uninfected, whole-infected and regionally infected monolayers during 1 Hz pacing demonstrated no significant differences in CV among groups (Figure 2.5).

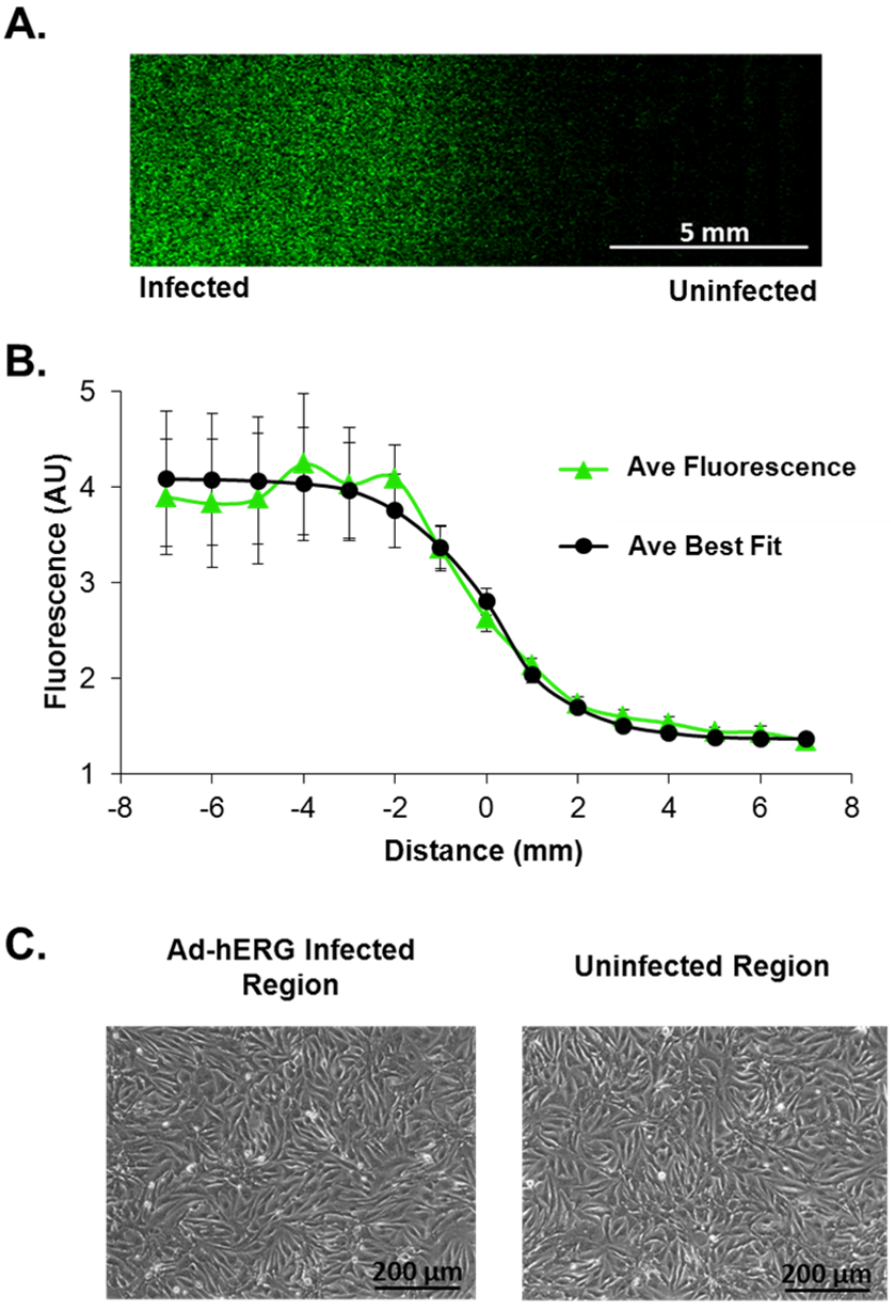

Figure 2.3. Spatial Gradient in hERG Expression. A. Fluorescence image across 16 mm at the center of a monolayer regionally infected with Ad-hERG-GFP. **B.** Average fluorescence gradient and best fit with a slope factor (dx) = 0.97 ± 0.12 mm (n=6, x_0 of best fit is set to 0). **C.** Phase contrast images of infected and uninfected regions show full myocyte confluency and structural homogeneity.

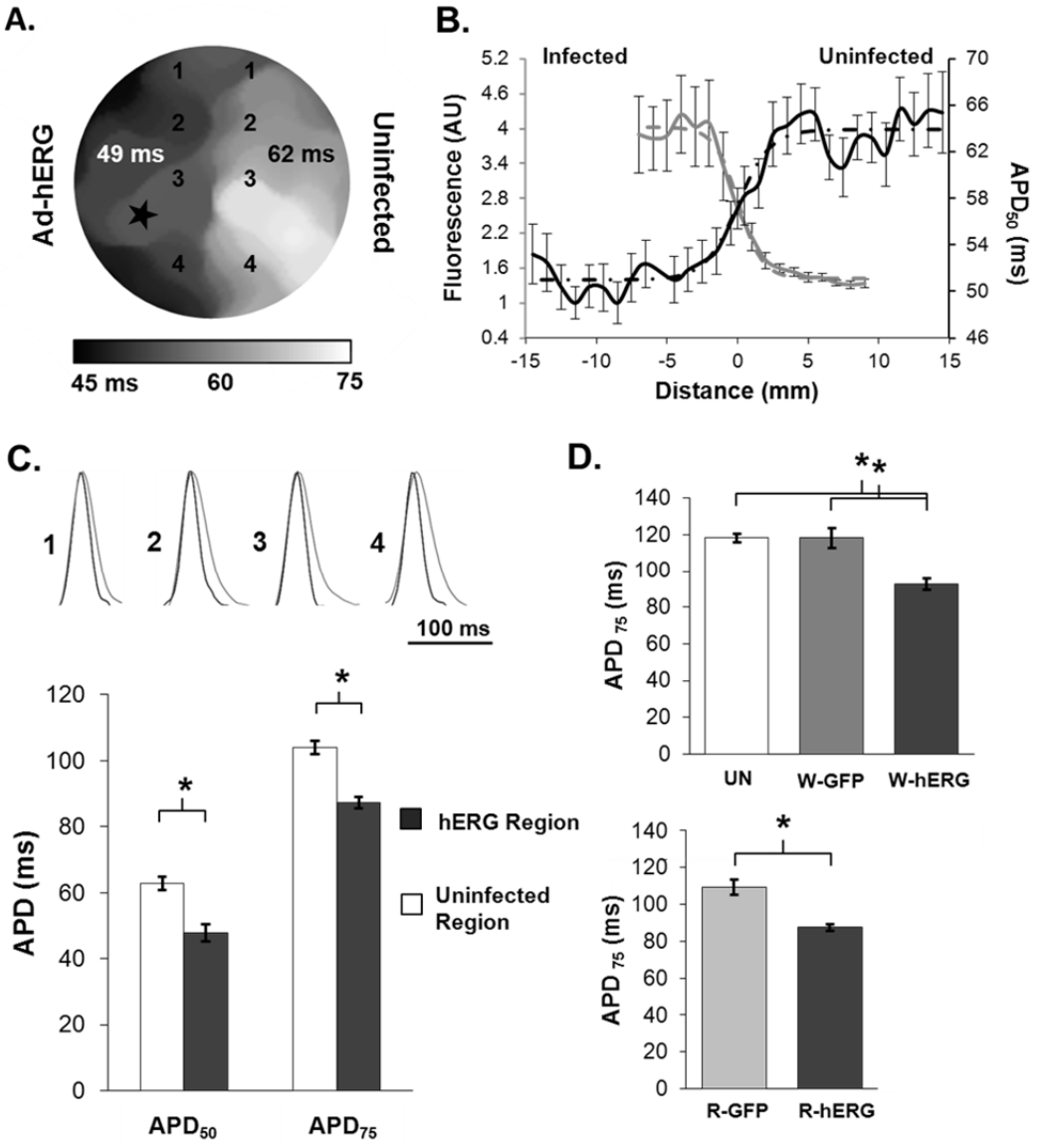

Figure 2.4. APD Distribution During Pacing at 1 Hz. A. APD_{50} map shows regional APD heterogeneity (paced from star). **B.** APD_{50} profile perpendicular to infection border superimposed on Ad-hERG-GFP profile. **C.** Top: superimposed representative optical action potentials in infected (black) and uninfected (grey) regions: pixel locations indicated on APD map above. Bottom: mean ± SEM APD_{50} (n=3, p=0.009) and APD_{75} (n=3, p=0.003) in infected and uninfected regions. **D.** Mean ± SEM APD_{75} values for homogeneous (top) and infected region of heterogeneous monolayers (bottom). Top: UN (uninfected; n=11); W-GFP (whole Ad-GFP infected; n=7); W-hERG (whole Ad-hERG infected; n=9), * p<0.0005. Bottom, R-GFP (regionally Ad-GFP infected; n=9); R-hERG (regionally Ad-hERG infected; n=3) * p=0.015.

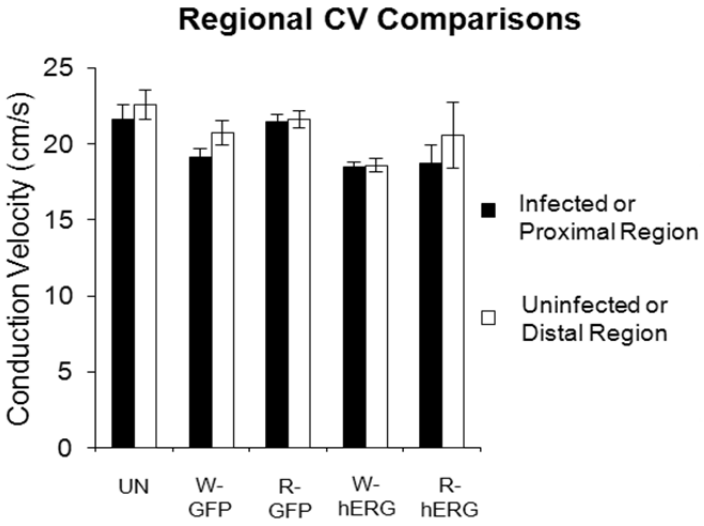

Figure 2.5. Regional Conduction Velocity. During 1 Hz pacing from the proximal half (infected half for regional infections), regional CV between all groups was found to be non-significant (uninfected n=11, GFP whole n=8, GFP Regional n=9, hERG whole n=8 and regional hERG n=3, $p>0.05$).

2.3.2 Rotors in Heterogeneous Monolayers

Single or multiple rotors were observed in any given monolayer group. Dominant rotors were defined as those being the most stable, having the longest life-span and presenting the maximal DF (DF_{max}). Figure 2.6 (top) shows snapshots of dominant rotors in a whole Ad-hERG infected monolayer (left; DF_{max}, 14 Hz) and in the infected region of a regional Ad-hERG infected monolayer (right; DF_{max}, 14.8 Hz). Time-space plots (TSPs) in the center show that in the W-hERG monolayer the waves emanating from the rotor propagated unobstructed throughout the field of view. In contrast, waves from a rotor of similar DF_{max} in the infected region of the regionally infected monolayer underwent intermittent blockade and wavebreak as they impinged upon the border zone on their way to the uninfected region. In those cases slower and often short lived rotors were observed within the uninfected region. Therefore, while 1:1 propagation was maintained throughout the whole-infected monolayer (left), the Ad-hERG gradient in the regionally infected monolayer resulted in a 4:3 m:n pattern of propagation from the infected to the uninfected region. As

shown by the DF maps, pixel by pixel power spectral analysis of the 5 sec movies yielded a DF gradient of 3.2 Hz in the regionally infected monolayer because of a reduced activation rate to 11.6 Hz in the uninfected region. Similar results were obtained when high frequency pacing (15 Hz) in the infected region was used to compare wave propagation in regionally infected versus whole-infected monolayers (Figure 2.7). As demonstrated below, the presence of the Ad-hERG expression gradient can generate wavebreak, block or delay when waves emanating from the infected region enter the longer APD border zone.

DF_{max} values were not significantly different between uninfected (UN), W-GFP and R-GFP (Figure 2.8.B). Similarly, the DF_{max} in W-hERG and R-hERG monolayers were the same; however, both were significantly higher than control groups. A non-significant DF_{max} difference between the R-GFP and UN groups was observed. This strongly suggests a dependency of DF_{max} on I_{Kr} density. Frequency analysis of the dominant rotors based on their location within the regionally infected Ad-hERG monolayers demonstrates that the level of hERG expression is a strong determinant of both the local DF_{max} and DF_{max} gradients across the monolayer.

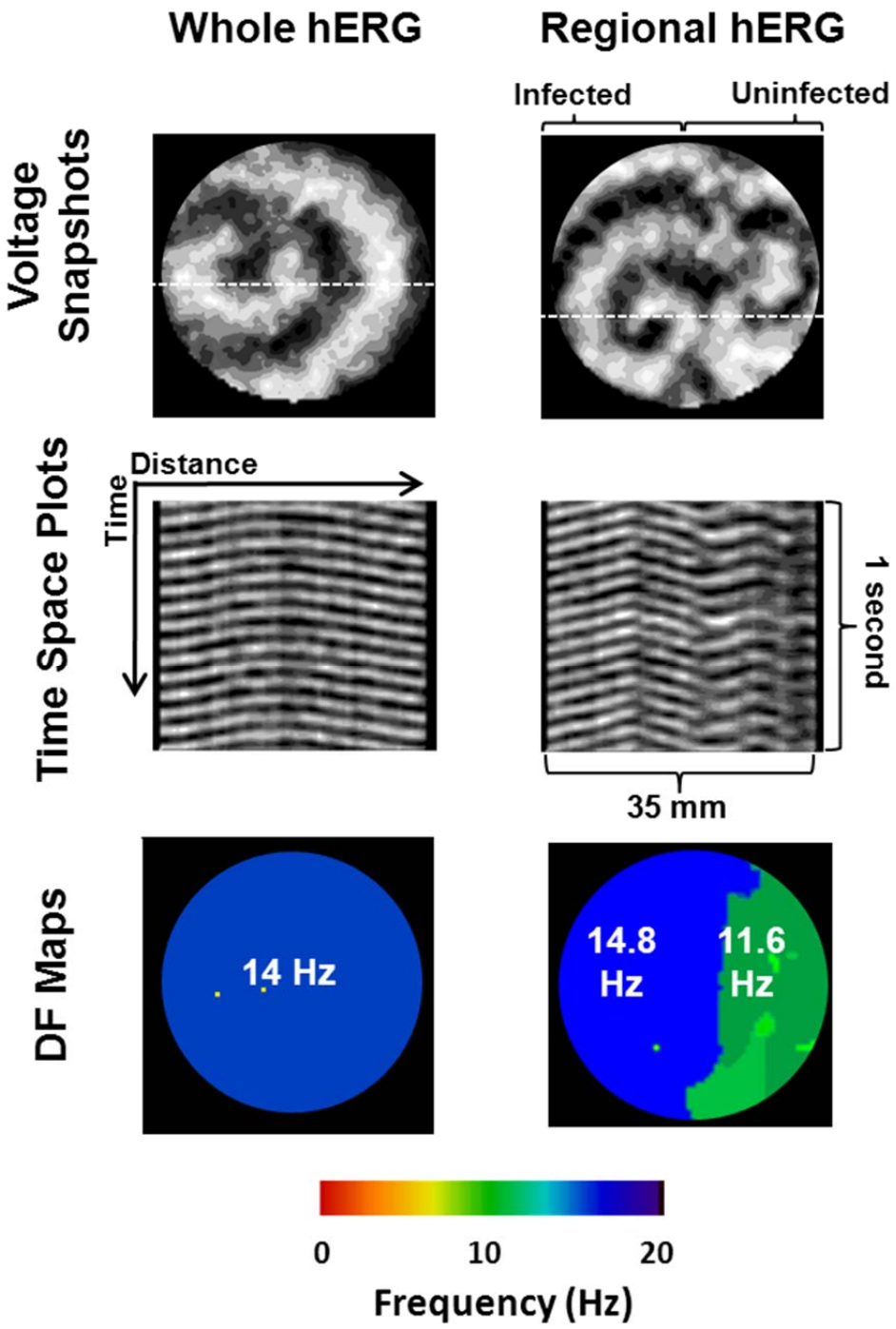

Figure 2.6. Rotor Activity and Propagation of Waves. Top: snapshots of dominant rotors in W-hERG (left) and R-hERG (right) monolayers. Center: time-space plots taken at the dashed lines in the snapshots. Uniform propagation in the whole-hERG (left), and 4:3 pattern in the R-hERG monolayer. Bottom: DF maps. Note 3.2 Hz gradient between infected and uninfected regions.

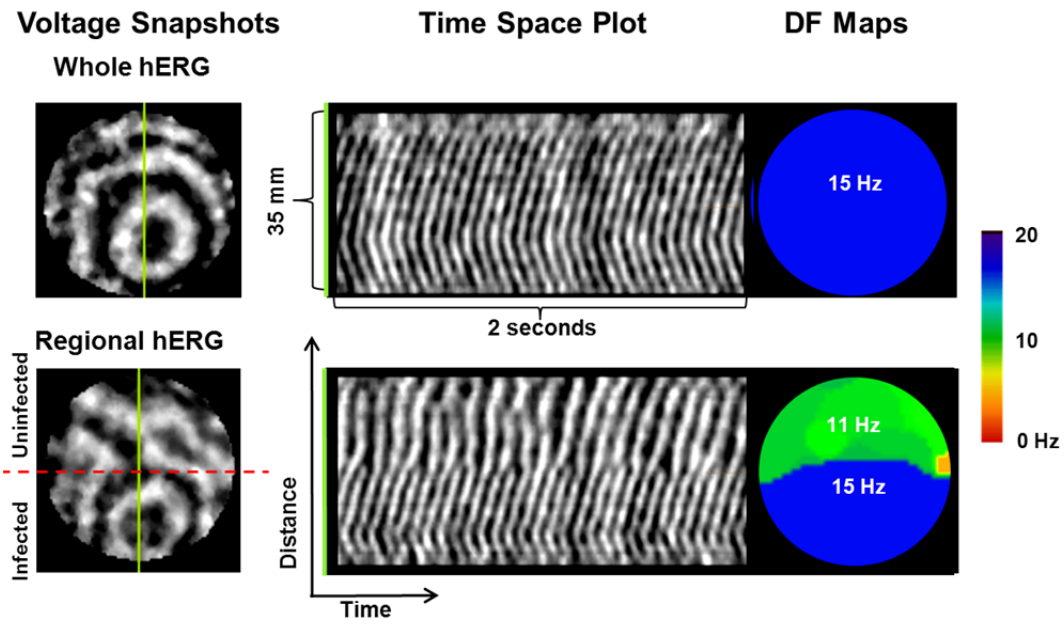

Figure 2.7. Pacing Induced Wavebreak. Top Left: I_{Kr} whole-infection; paced at 15 Hz. Top Mid: time space plot (TSP) (taken at the green line) shows the lines activity over time on the x-axis (total 2 sec). Top Right: DF Map. Bottom Left: I_{Kr} regional infection paced at 15 Hz. Bottom Mid: TSP showing block, 70% of waves pass into the uninfected region. Bottom Right: DF Map. In all homogeneous dishes (infected with I_{Kr} (n=9), uninfected (n=14), GFP (n=2)), no block was observed. In all I_{Kr} heterogeneously infected dishes (n=9) block and/or wavebreak was seen when pacing was ≥ 10 Hz from the infected region. Regions of block occurred along the interface between the APD regions.

2.3.3 Incidence and Localization of Rotors Generating Fibrillatory Conduction

Many rotors spontaneously appeared, presenting an opportunity to determine whether the level of I_{Kr} expression modulated the incidence of spontaneously occurring rotors (Table 2.1). Overall, the incidence of spontaneous rotor activity was different among hERG overexpressing and control groups (p=0.005, χ^2 analysis). For uninfected, W-GFP, and R-GFP groups, the percentage of spontaneous rotors was similar, 39% (12/31), 25% (4/16) and 35% (7/20) respectively. For the W-hERG group it was

74% (45/62), suggesting that I_{Kr} overexpression alone generates spontaneous rotor activity. However, the R-hERG group had an even higher proportion of spontaneous rotors at 84.2% (64/76) of the time. Suggesting that regional I_{Kr} overexpression may be an independent promoter of spontaneous rotor activity and appears to be a factor in the initiation of arrhythmias.

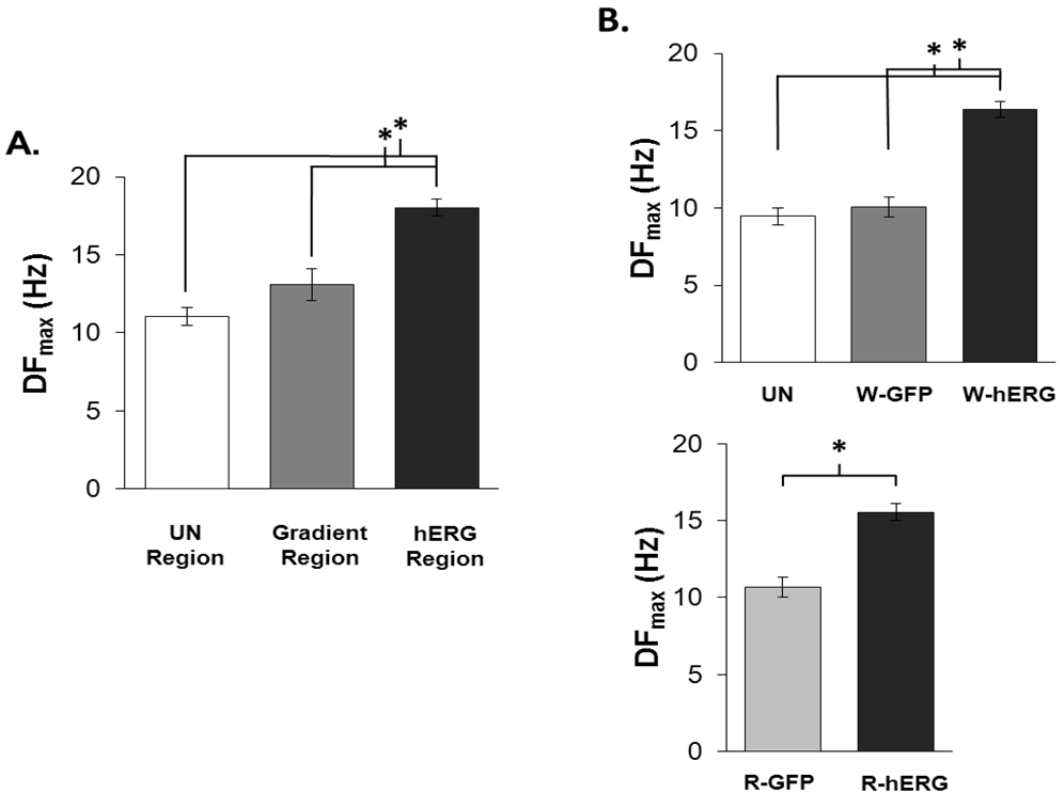

Figure 2.8. Rotor Frequencies. A. hERG gradient results in DF_{max} gradient. DF_{max} in the Ad-hERG infected region (n=37) was significantly higher frequencies than gradient (n=12) and uninfected (n=15) regions *$p<5x10^{-9}$. **B.** DF_{max} values. No significant differences between uninfected (n=12) and W-GFP (n=4). However both were significantly different from W-hERG (n=45) *$p<5x10^{-9}$. DF_{max} of R-hERG monolayers (n=64) was significantly higher than R-GFP monolayers (n=7) (p=0.005).

Dominant rotors and DF_{max} sites were homogeneously distributed and did not show any regional preference in the uninfected, W-GFP, R-GFP or W-hERG monolayers. Also, in the presence of a single rotor, these monolayers did not generate wavebreak patterns or fibrillatory conduction even during high frequency activity. When more than one rotor was present, annihilation occurred by collision of wavefronts generated by each of the rotors, but this did not generate significant DF heterogeneity.

In R-hERG monolayers, the dominant rotors showed a preference to stably localize within the infected region. Dominant rotors were seen within the infected region (57.8%), the gradient region (18.8%), and the uninfected region (23.4%) in 64 monolayers ($p<0.0001$; χ^2 analysis).

Regional hERG heterogeneity with rotors localized within the infected region was the only condition which generated patterns of wavebreak and fibrillatory conduction. We did not observe wavebreaks in R-hERG monolayers when the dominant rotor was localized within the border zone or the uninfected region. However, average DF and standard-error (SE) maps of R-hERG monolayers with rotors localized within the infected region (n=37) clearly divide the monolayer into two halves (Figure 2.9): The infected half has DFs ~16 Hz and the uninfected half ~12 Hz, with intermediate levels at the border zone. The SE is much larger in the infected than the uninfected half, likely due to a varying level of I_{Kr} overexpression in the infected half. In contrast to the heterogeneous DF map, when rotors localized in the uninfected half or in W-hERG infected monolayers the DF maps were uniform (right side of Figure 2.9).

To further quantify the consequences of I_{Kr} heterogeneity and rotor location, we collected average DF profiles perpendicular to the border zone. Only rotors that localized within the infected region of the R-hERG monolayers produced wavebreaks (Figure 2.10.B, triangles), this resulted in a DF gradient profile (Figure 2.11). DF changed gradually in space from

values similar to those in the W-hERG monolayers (squares) to those similar to DFs when the rotor was in the uninfected region (diamonds). The half-way transition point (x_o) occurred approximately at the center of the border zone (18.5 mm from the uninfected edge of the dish (left) or at -1 mm along the x-axis in Figure 2.10.A). The DF transition depended on the precise location of the dominant rotor and on whether two or more dominant rotors co-existed. Multiple dominant rotors in the infected region yielded a heterogeneous DF profile with a larger slope factor than for single dominant rotors which had a sharper DF transition (Figure 2.11).

Table 2.1. Spontaneous Rotor Activity

Monolayer Group	Percentage of Spontaneous Rotor Activity	Percentage of Dominant Rotors Based on Location			
		Uninfected or Distal Region	Gradient or Central Region	Infected or Proximal Region	Multiple Rotors Uniform DF
Uninfected	(12/31) 38.7%	(4/12) 33.3%	(3/12) 25%	(4/12) 33.3%	(1/12) 8.3%
Ad-GFP Whole	(4/16) 25%	(1/4) 25%	(1/4) 25%	(1/4) 25%	(1/4) 25%
Ad-GFP Regional	(7/20) 35%	(3/7) 42.9%	(2/7) 28.6%	(2/7) 28.6%	
Ad-hERG Whole	(45/61) 73.8%	(8/45) 17.8%	(10/45) 22.2%	(15/45) 33.3%	(12/45) 26.7%
Ad-hERG Regional	(64/76) 84.2%	(15/64) 23.4%†	(12/64) 18.8%†	(37/64) 57.8%†	

Distal, Central and Proximal regions were assigned to wholly infected monolayers as described in the Methods section. † Significantly different from one another $p<0.0001$; χ^2 analysis

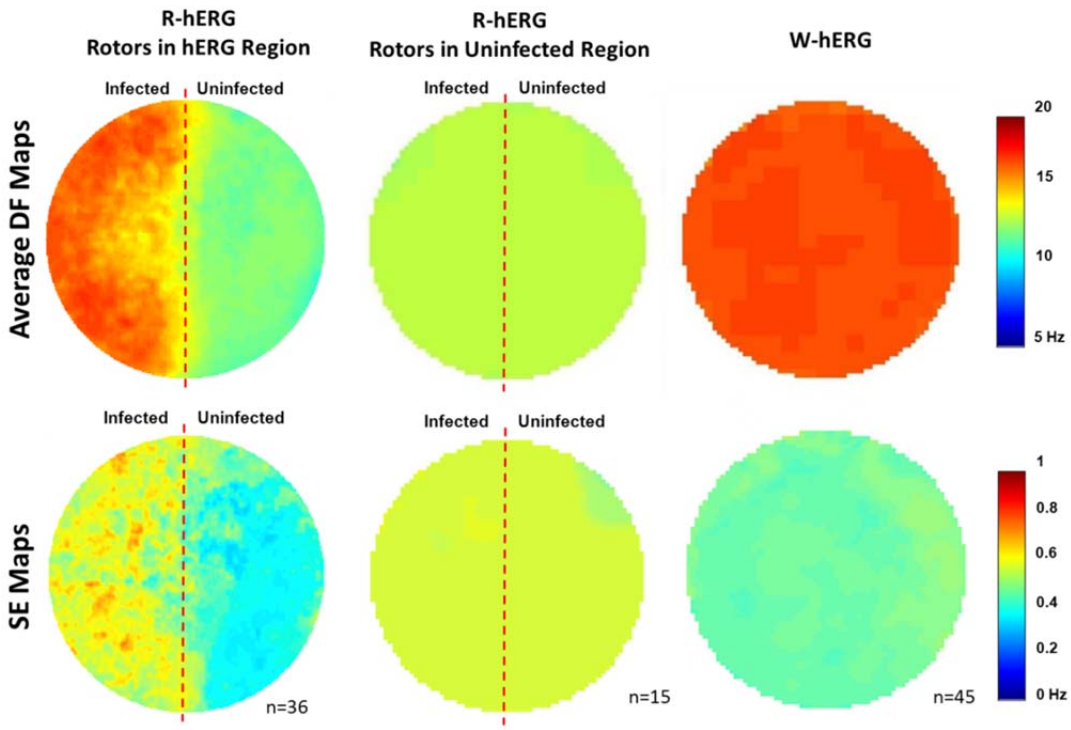

Figure 2.9. Average DF Maps and DF Profiles. Average DF maps and corresponding standard error maps of spontaneous rotors in the infected half of regionally infected Ad-hERG monolayers (Left, n=36), uninfected half of regionally infected Ad-hERG monolayers (Center, n=15) and wholly Ad-hERG infected monolayers (Right, n=45). Only when the rotors are localized in the hERG infected region of the regionally infected monolayers is there any significant regional DF heterogeneity, while the remaining groups show uninform average DF maps.

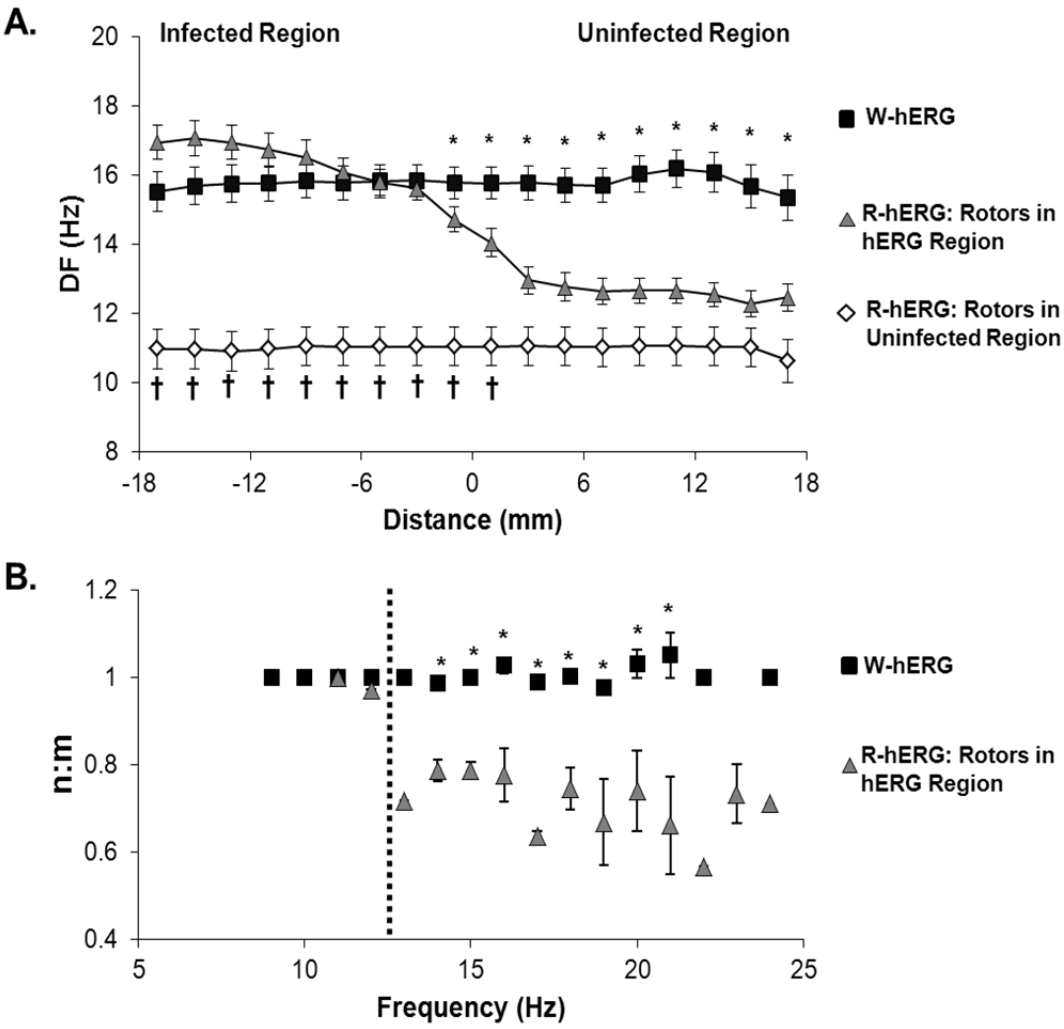

Figure 2.10. DF Gradients Across Heterogeneous Monolayers. A. Spatial DF profiles for rotors in the infected (triangles, n=37) and uninfected (diamonds, n=15) regions of R-hERG monolayers. R-hERG with rotors in the infected region is significant to W-hERG (* $p<0.05$) and to R-hERG with rotors in the uninfected region († $p<0.05$). The half-way transition point of the DF profile in the R-hERG monolayers occurred within the gradient region. **B.** Values of n:m for W-hERG (squares, n=45) and R-hERG (triangles, n=37) monolayers as a function of dominant rotor frequency. Dashed line is the frequency at which wavebreak begins.

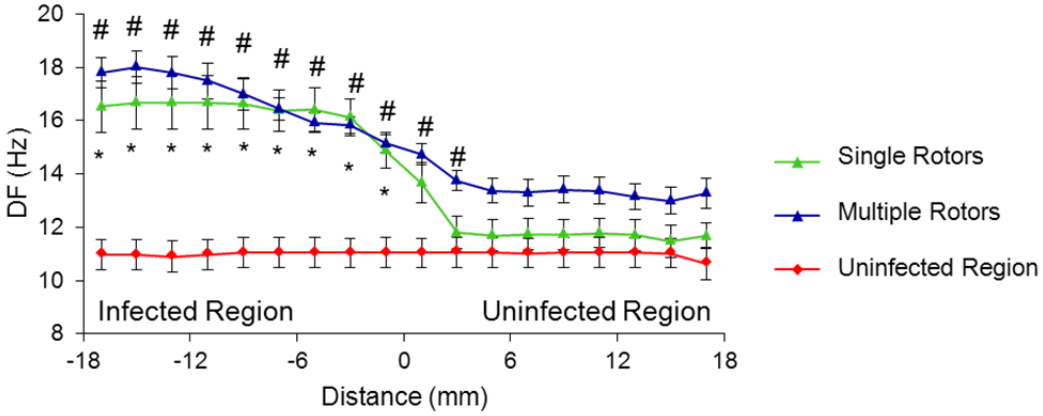

Figure 2.11. DF Profiles, Singular and Multiple Rotors. Differences in DF profiles between cases of singular rotors or multiple rotors are localized within the I_{Kr} overexpressing region. While not significantly different from one another, the multiple rotor group (blue, n=17) has significantly higher frequencies over 20.5 mm while the singular rotor group (green, n=9) is significant only to 17.5 mm compared to the uninfected group (# $p<0.05$).

To determine the frequency dependence of wavebreak, we characterized the proximal-to-distal activation ratios (n:m) over a range of rotor frequencies (Figure 2.10.B). The n:m for W-hERG and R-hERG with rotors localized in the uninfected region remained at 1.00 ± 0.005 (n=45; 9-24 Hz) and 1.00 ± 0.005 (n=15; 7.5-12.9 Hz). However, when rotors in the infected region had frequencies of 12.9 Hz or higher, complex patterns of activation developed, ranging from AR = 0.72 (i.e., m:n = 3:2; infected:uninfected) at 12.9 Hz to 0.57 (5:3) at 22 Hz. Other intermediate ARs were also observed, including 0.79 (5:4) and 0.66 (20:13). Finally, we observed a declining trend in n:m as the spontaneous rotor frequency increased to 24 Hz. Altogether, regional gradients in Ad-hERG resulted in intermittent wavebreak and significantly variable n:m when the frequency of rotors in the infected region ranged between 13 and 24 Hz.

Next, we calculated the regularity index (RI), taken from the power spectrum defined as the power under the DF_{max} divided by the total

power[117, 165] to determine where wavebreaks and fractionation occurred most frequently in the R-hERG monolayers. Figure 2.12.A shows a phase map in which a rotor in the infected region was accompanied by fibrillatory conduction toward the uninfected region. Three pixels were sampled for RI analysis: Pixel (1) near the core of the dominant rotor showed a frequency of 14.8 Hz and a relatively high RI at 0.72; pixel (2) at the border zone also showed 14.8 Hz, but its RI was appreciably reduced (0.53); pixel (3) in the uninfected region showed a reduced frequency (11.7 Hz) but a high RI (0.71). The spectrum at pixel 2 clearly shows 2 peaks each corresponding to the frequency of activation within the infected and uninfected regions. Average RI and SE maps demonstrate that there is a substantial area within the border zone (horizontal dashed line) which consistently has reduced RI of about 0.4 or lower. RI profiles perpendicular to the border zone taken for single dominant rotors in the infected (green) and uninfected regions (red) show that 1) regularity is higher when the rotors are in the uninfected region compared with the infected region; and 2) irregular activity at the center of the border zone (-2.5 to 3.5 mm on the x-axis or 15-21 mm from the infected edge of the monolayer) is greatest when the rotors reside within the hERG infected region.

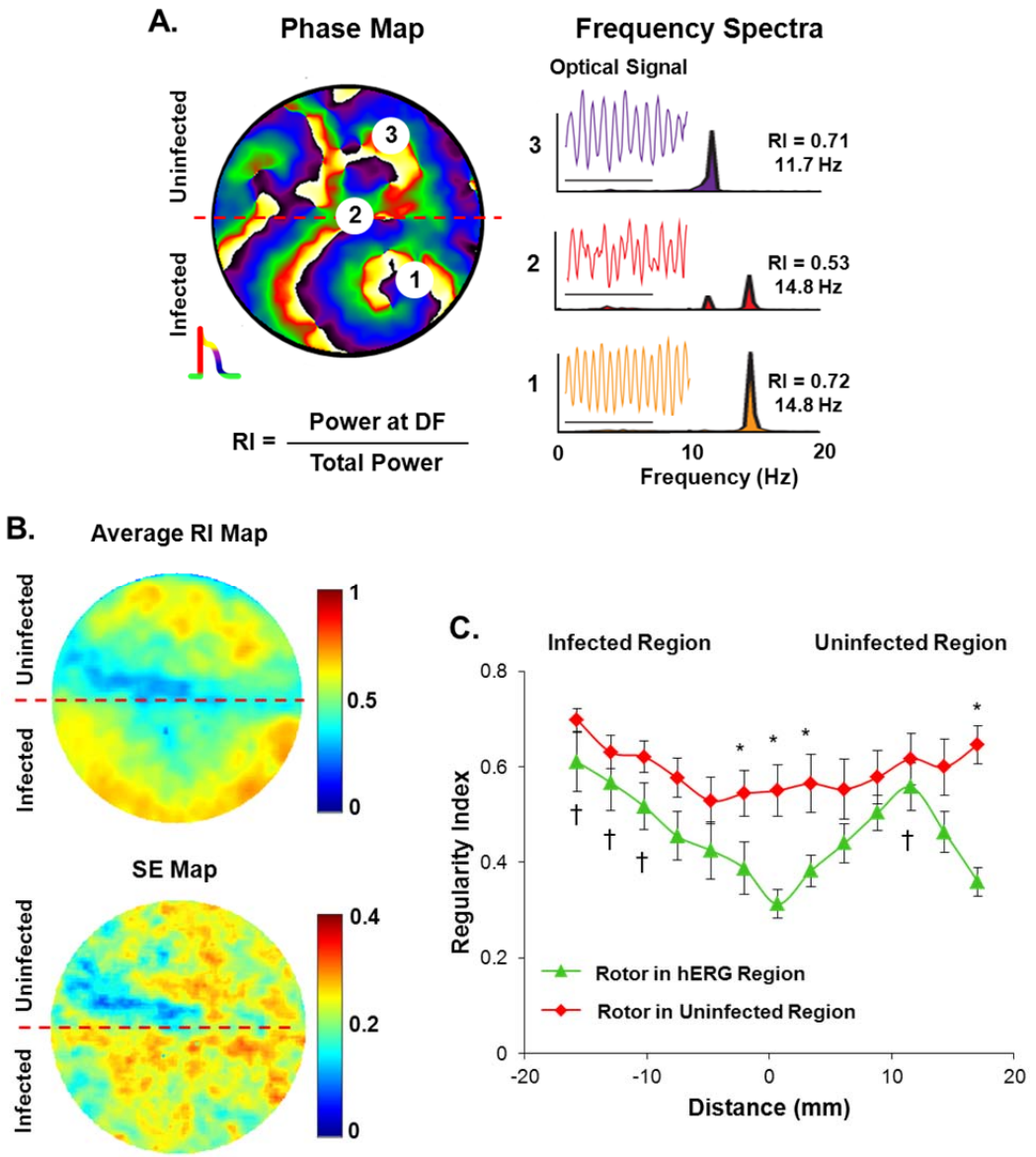

Figure 2.12. Single Rotors and Regularity Index Gradients. A. Left: color phase map. A rotor in the infected region resulted in fibrillatory conduction in the uninfected region. Map shows pixel locations 1-3 used for RI analysis. Right: single pixel time series and power spectra for points 1-3. **B.** Average RI and SE maps (n=10) show reduced RI at the border zone (dashed red line). **C.** Spatial RI profiles perpendicular to the border zone for single dominant rotors in the infected (triangles, n=10) and uninfected regions (diamonds, n=12, * $p<0.05$). RI is high when the rotors are in the uninfected region. RI is lowest at the border zone when the rotor resides within the infected region, † $p<5x10^{-5}$ between minimal RI (18.5 mm).

2.3.4 Mechanisms of Wavebreak and Fibrillatory Conduction: Computer Simulations

Experimental data obtained from the regional hERG overexpression suggest that rotor acceleration and fibrillatory conduction are consequences of the non-uniform I_{Kr} current density distribution, which results in significant APD dispersion. To support this idea and to further investigate the mechanisms of fibrillatory conduction, we used a 2D mathematical model of NRVM electrical activity (see Figure 2.13 and Appendix A for details). Figure 2.14.A shows a snapshot (left) and TSP (right) of rotor activity in a monolayer model with a regional 5-fold increase in I_{Kr} conductance (G_{Kr}) in the rotor region. Similar to the experiments, a stable rotor at 15.0 Hz in the region of increased G_{Kr} ("infected" region) generated wavefronts that blocked intermittently at the border zone and resulted in a 3:2 m:n pattern (n:m = 0.67) of propagation in the region of nominal G_{Kr} ("uninfected region"), which closely reproduced the experimental results (n:m at 15 Hz is 0.79 ± 0.02; n=4).

Computer simulations were specifically implemented to fetter out the respective roles of regional APD and maximum diastolic potential (MDP) in the mechanism of fibrillatory conduction, to do this we first examined their dependence on G_{Kr} in the infected region. In Figure 2.14.B, APD_{80} decreases as G_{Kr} increases, as expected. In the uninfected region (squares), APD_{80} decreases somewhat at G_{Kr} values below the wavebreak point (dashed line). Beyond that point, 1:1 propagation (n:m = 1.0) cannot be maintained. Consequently APD_{80} in the uninfected region increases stepwise from 42 to ~50 ms, while APD_{80} in the infected region (diamonds) decreased linearly with the G_{Kr} increase. In C, the MDP in the infected region hyperpolarizes monotonically from -69.5 mV at G_{Kr} = 1 to about -76 mV at 20xG_{Kr}. At the same time, the MDP in the uninfected region varies non-monotonically: When the G_{Kr} in the infected region

changes from 1 to 2x, the uninfected region depolarizes slightly to about -68 mV, likely due to the increased DF during 1:1 activation of that region. At the wavebreak point, 1:1 activation is lost and the MDP in the uninfected region changes abruptly to a relatively stable level of ~-70 mV. Hence, the next step was to test the relationship between APD dispersion and the MDP distribution in the generation of fibrillatory conduction.

We next conducted simulations to evaluate the role of MDP in the generation of wavebreak. In Figure 2.15 we clamped the MDP of each monolayer at incremental predetermined depolarized values while allowing APDs, DF_{max} and ARs to vary spontaneously. In A, MDP profiles along the length of the monolayer ranged from the unclamped values ($5xG_{Kr}$ region, -72 mV; $1xG_{Kr}$ region, -70 mV) to -62 mV. The unclamped, -72 and -71 mV clamped profiles resulted in non-uniform MDPs with the more negative values in the $5\times G_{Kr}$ region. All other conditions resulted in a uniform MDP profile as the clamped values rose to -70 mV and above (the MDP in the $1\times G_{Kr}$ regions). The DF profiles, shown in B, correspond to each clamped MDP value. It is clear that: 1) DF in the $5\times G_{Kr}$ region is not sensitive to MDP values more negative than -68 mV (values which are close to those in the $1xG_{Kr}$ region); and 2) DF gradients exist for MDPs up to -67 mV, which allow for rotor $DF_{max} \cong 14.6$ Hz in the $5\times G_{Kr}$ region. In addition, as the MDP clamp value changes to more depolarized levels, the location of wavebreak shifts to the right; i.e., toward the $1xG_{Kr}$ region. It is only when the MDP is clamped at -66 mV or more positive voltages that the driving rotor is forced to slow to ~13.7 Hz, at which point wavebreak and fibrillatory conduction are no longer possible, and the uninfected-to-infected n:m becomes 1.0. Panel C shows the manner in which rotor DF_{max} (black) and n:m values change as the clamped MDP depolarizes. Between -72 and -67 mV rotor DF_{max} remains high, and wavebreaks at the border zone result in fibrillatory conduction with an n:m of ~0.6. At -66 mV,

DF_{max} begins to decline, wavebreak ceases and n:m becomes equal to 1.0.

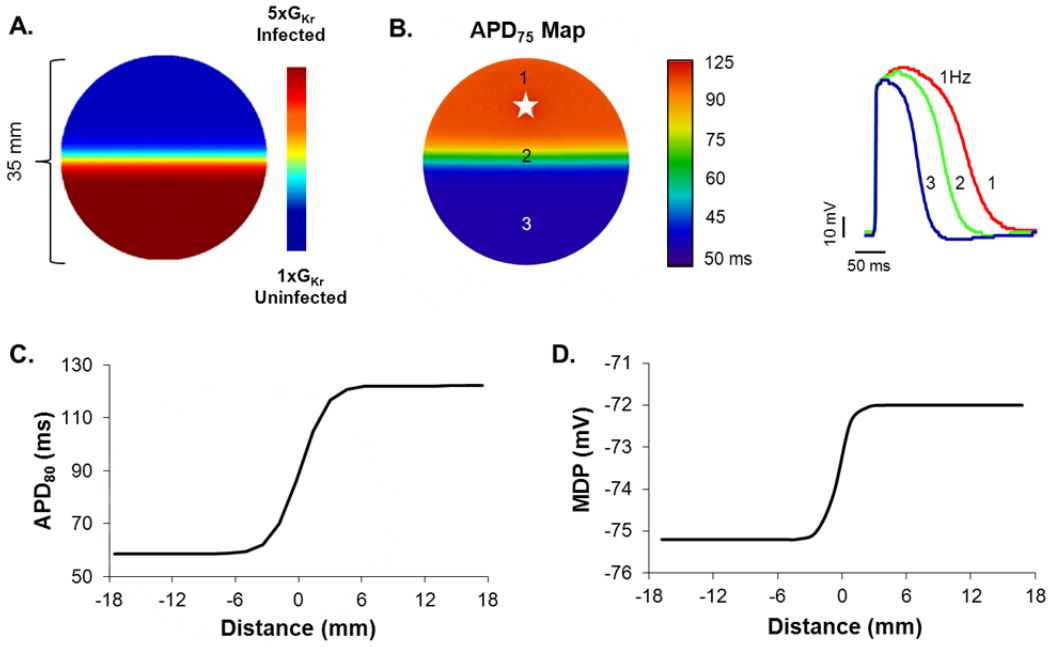

Figure 2.13. Fitting I_{Kr} Fluorescence Gradient to a Boltzmann Distribution. **A.** Left: Fluorescence gradient for I_{Kr} regional infection fitted to a Boltzmann distribution (Δx = 0.97 ± 0.119 mm, n=4) was used to generate the spatial gradient of the maximal conductance of G_{Kr} (x_0 = 17.6 mm and slope Δx = 0.98676 mm) used in simulations. Shown is its introduction into the 2D mathematical model. $5xG_{Kr}$ was used for the upregulated region. **B.** APD_{75} map implementing the spatial gradient in G_{Kr} with representative regional AP traces paced at 1 Hz from star. **C.** G_{Kr} heterogeneity induces both unequal APD and MDP distribution profiles across the model. APD_{50} profile taken perpendicular to G_{Kr} gradient, APD_{50} is 103.3 ms within the $1xG_{Kr}$ region and 48.1 ms within the $5xG_{Kr}$ region. **D.** Resting membrane potential (RMP) profile perpendicular to G_{Kr} gradient. RMP is -72.0 mV within the $1xG_{Kr}$ region and -75.2 mV within the $5xG_{Kr}$ region.

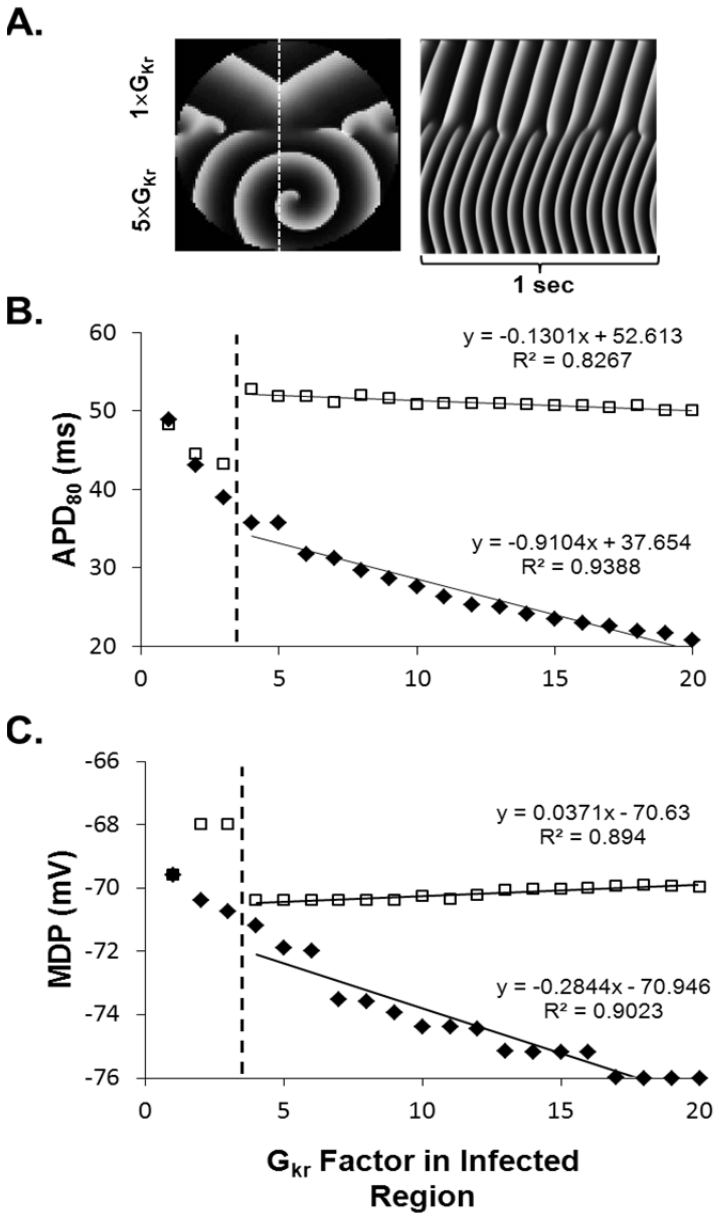

Figure 2.14. Simulations Showing Dependence of APD_{80} and MDP on G_{Kr} Factor in the "Infected Region". A. Snapshot (left) and TSP (right) taken at the dotted vertical line showing rotor activity in the infected region (G_{Kr}=5x). At 15 Hz, rotor activity generated wavefronts that transformed at the border zone into a 3:2 (infected:uninfected) pattern. **B.** APD_{80} in the infected (diamonds) and uninfected (squares) regions as a function of G_{Kr} factor in infected region showing an initial transient decrease of APD_{80} in the uninfected region (2-3xG_{Kr}). **C.** MDP vs. G_{Kr} factor in the infected region. MDP transiently depolarizes in the uninfected region when G_{Kr}=2-3x in the infected region. Dashed lines - critical value of G_{Kr} at which wavebreak occurred.

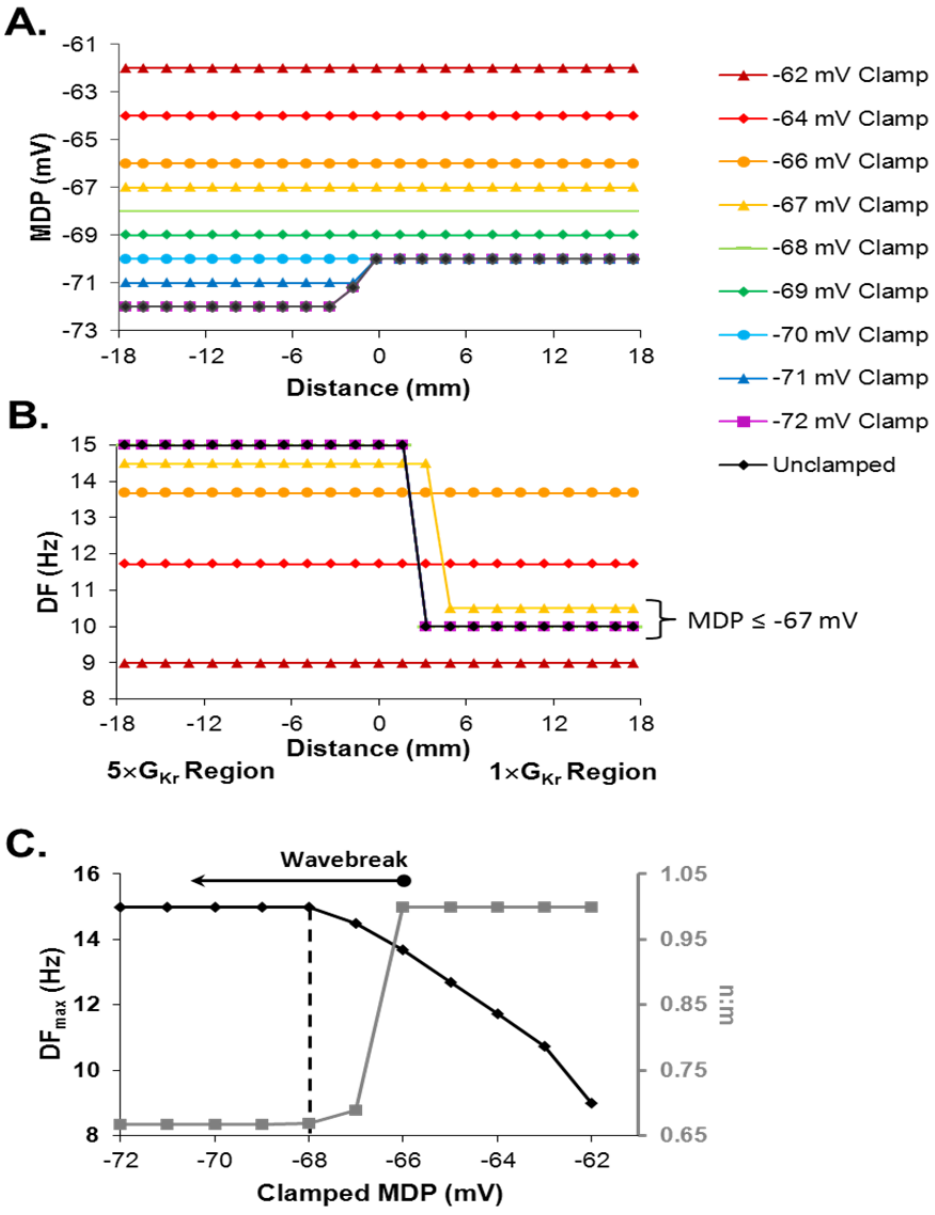

Figure 2.15. MDP and the Control of DF_{max} Gradients. A. MDP was clamped at varying predetermined values. APD and ARR were allowed to change. MDP ranged from the unclamped values ($5xG_{Kr}$, -72 mV; $1xG_{Kr}$, -70 mV) to -62 mV. **B.** Spatial DF profiles correspond to MDP as indicated. DF in the $5xG_{Kr}$ region is insensitive to MDPs more negative than -67 mV remaining at 14.7 Hz. The rotor frequency decreases when clamped MDP is less negative than -66 mV and wavebreak ceases. **C.** Rotor DF_{max} (black) and n:m (grey) change as functions of MDP in the infected region. For MDP of -68 mV and more negative DF and n:m remain constant.

It is important to stress that, in the unclamped condition (Figure 2.15.A, black diamonds) appreciably different MDPs would be expected to contribute to the genesis of wavebreak, in part by establishing different APD values in the two regions. However, wavebreak and fibrillatory conduction continued to occur at clamped MDPs of -70 to -67 mV, which are equal to, or slightly more positive than the MDP of the unclamped 1xG_{Kr} region. This suggests that an MDP gradient is not essential to generate wavebreak (see also Figure 2.16).

We demonstrated in Figure 2.14.B (see above) the strong dependency of APD_{80} on G_{Kr} in the numerical NRVM model. In Figure 2.17.A we demonstrate a similar strong dependency of rotor DF_{max} on APD_{80}. As shown in Figure 2.14, there is a critical level of G_{Kr} (and APD) at which 1:1 propagation across the border zone is no longer possible. Thus we conducted a set of simulations over a range of G_{Kr} values to determine whether the model predicts a critical level of DF_{max} at which wavebreak should occur. In 2.17.B, DF is plotted as a function of G_{Kr} in the infected region. Consistent with recent experimental and simulation data[107, 113], DF in the infected region (diamonds) increases linearly as G_{Kr} increases up to 20x. The uninfected region (squares) is activated in a 1:1 manner up to a rotor frequency of ~13.7 Hz, corresponding to 3xG_{Kr} in the infected region (vertical dashed line). Beyond that line, intermittent wavebreaks at the border zone resulted in sharp DF reduction in the uninfected region, with stabilization at 10.2-11.3 Hz, regardless of the DF values in the infected region. Panel C demonstrates the manner in which the ARs across the border zone change with the DF_{max} of the rotor in the infected region. Altogether, the numerical data predict a critical rotor DF_{max} in the infected region at which wavebreak and fibrillatory conduction should occur. Such predictions are clearly borne out of the experimental

results in which n:m ratios <1 reproducibly appear at a critical DF_{max} breakpoint of ~14 Hz (see Figure 2.10).

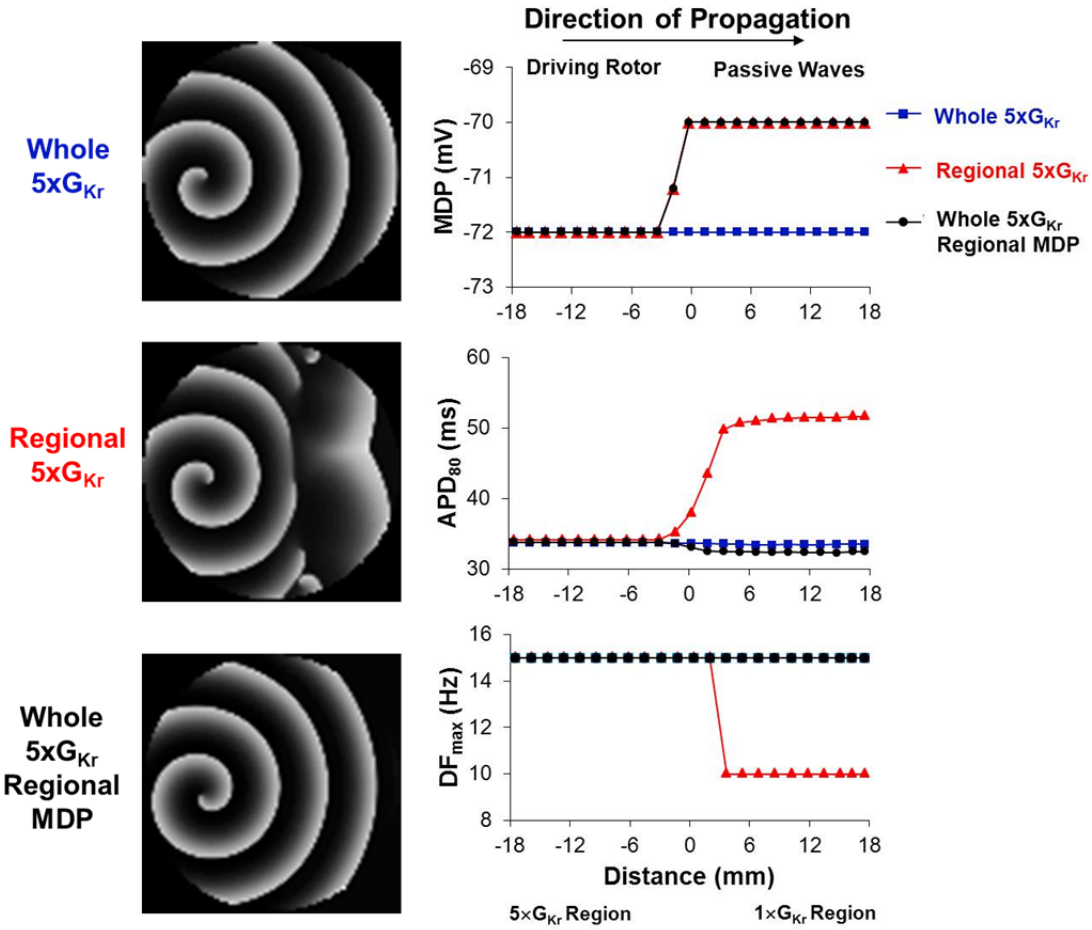

Figure 2.16. MDP Gradients are not a Major Mechanism of Wavebreak. A. Snapshots of rotors in whole 5xG$_{Kr}$ (top), regional 5xG$_{Kr}$ (middle) and whole 5xG$_{Kr}$ with regional MDP (bottom) simulations. Rotors are localized on the left hand side which corresponds to the 5xG$_{Kr}$ and/or lower MDP regions. Wavebreak is only observed in the regional 5xG$_{Kr}$ model. **B.** MDP as a function of distance across the gradient in whole 5xG$_{Kr}$ (blue squares), Regional 1-5xG$_{Kr}$ (red triangles) and whole 5xG$_{Kr}$ simulation with the application of a MDP gradient (black circles) similar to the MDP gradient generated in the Regional 1-5xG$_{Kr}$ model. **C.** APD_{80} as function of distance across the gradient. **D.** DF Profiles across the gradients indicate that only the Regional 1-5xG$_{Kr}$ and not the Regional MDP model generated a decrease in frequency.

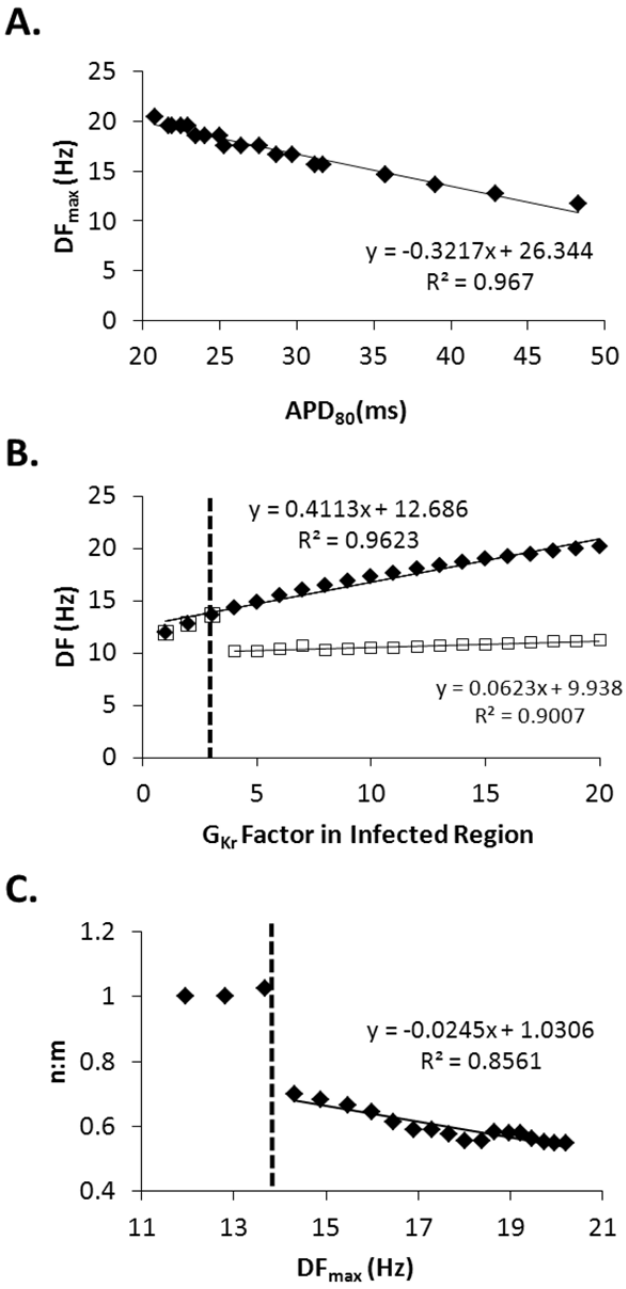

Figure 2.17. Critical Dependence of Wavebreak and Fibrillatory Conduction on DF Gradient. A. Rotor DF_{max} strongly depends on APD_{80}. **B.** DF in infected (diamonds) and uninfected (squares) regions as functions of G_{Kr} in infected region. Vertical broken line shows level of G_{Kr} at which wavebreaks occur. **C.** Values of n:m across the border zone as a function of DF_{max} in the infected region at varying levels of G_{Kr} in the infected region. Vertical line shows critical rotor DF_{max} (~14 Hz) at which wavebreak occurs.

2.4 Discussion

2.4.1 Major Results of the Study

We have investigated the mechanisms by which gradients in I_{Kr} density contribute to the mechanisms of high-frequency rotor formation, wavebreak and fibrillatory conduction in heterogeneous cardiac tissues. Gradients in hERG and GFP expression were created in NRVM monolayers using adenoviral-mediated magnetofection, which allowed accurate spatial control of protein distribution. Computer simulations using a realistic NRVM monolayer model provided mechanistic insight which greatly clarified experimental results. Our main findings were: 1) Regional increase in I_{Kr} density shortened the APD and increased the incidence of rotor formation in the Ad-hERG infected region. 2) An APD_{75} gradient profile of 16.6 ± 0.72 ms followed the distribution profile of hERG-GFP across the monolayer; conduction velocity was not significantly altered by Ad-hERG infection. 3) Rotors in the Ad-hERG infected region whose DF_{max} was ≥12.9 Hz resulted in wavebreak at the interface (border zone) between infected and non-infected regions; when the DF_{max} was <12.9 Hz or the rotors resided in the uninfected region, the DF distribution was uniform. 4) The higher the rotor DF_{max} in the infected region the lower the regularity at the border zone. 5) In computer simulations, the regional increase in I_{Kr} led to both regional APD abbreviation and MDP hyperpolarization. However, the steep APD gradient at the border zone was the primary mechanism of wavebreak and fibrillatory conduction in this model. Overall, our study provides insight into the molecular mechanisms by which non-uniform distribution of a major repolarizing potassium channel results in rotor stabilization, APD dispersion and fibrillatory conduction.

2.4.2 Magnetofection Enables Controlled Spatial Gradients in Ion Channel Expression

Regional magnetofection can be used to generate structurally homogeneous but electrically heterogeneous monolayers to investigate the role of spatial gradients in ion channels in the mechanism of cardiac fibrillation. Magnetofection is a relatively new technique that is used primarily to enhance cellular infection efficiency[167]. Our novel use of Magnetofection produced well controlled gradients in Ad-hERG-GFP expression in the form of a Boltzmann profile spanning over a distance of hundreds of NRVMs (~5 mm), with a slope factor of ~1 mm. We submit that such a gradual transition of ion channel distribution is much more realistic from the physiologic and pathophysiologic standpoint than the previous model of ionic heterogeneity which generates gradients that are (~50 μm) 100 times steeper that those we have created here[119]. Our approach enabled us to demonstrate for the first time that regional I_{Kr} heterogeneity is an arrhythmogenic substrate, which increases the probability of spontaneous rotor formation and promotes wavebreak and fibrillatory conduction from regions of high to low I_{Kr} density. The approach is readily applicable to the study of other channels and channel associated proteins and might prove useful in in-vivo experimental studies on the pathophysiological consequences of heterogeneous ion channel expression.

2.4.3 I_{Kr} Gradients and APD Dispersion in the Heart

Spatially distributed heterogeneity of I_{Kr} has been observed in a number of animal models and is associated with APD dispersion. In myocytes from the basal subendocardium of the guinea pig heart I_{Kr} is decreased by a factor of 0.6 with respect to the subepicardium[145]. Both

apical-to-basal and transmural gradients in the density of I_{Kr} channels have been reported in the ferret heart[146]. However, I_{Kr} distribution in the canine ventricles remains controversial. One study reported hERG expression to differ by as much as 3.3 fold on the epicardum of the left vs. right ventricles[168]. Another study reported a more than 2-fold transmural gradient[169]. Yet another study found that although treatment with I_{Kr} blockers revealed regional APD prolongation, under basal conditions there were no gradients in I_{Kr}[147]. Moreover, in canine wedge preparations, d-sotalol generated transmural APD heterogeneity and resulted in the generation of spontaneous as well as stimulation-induced Torsades de Pointes[147]. In canine atria, I_{Kr} density differed by ~20% between cells from the posterior wall of the left atrium and the pulmonary veins[124]. Unfortunately, none of the above studies showing regional differences gave an idea of how abrupt the transitions were from one region to the other. Nevertheless, based on the limited information available it is reasonable to estimate that the spatial differences correspond to gradual gradients spanning over a few millimeters.

2.4.4 Spatial Dispersion of K Channels and Cardiac Fibrillation

Cardiac fibrillation may depend on the presence of a small number of high frequency reentrant sources[57, 76, 170, 171]. Spiral wave fronts emanating periodically away from such sources may encounter functional, temporal and/or anatomical tissue heterogeneities and result in wavebreak with multiple wavelet formation[57]. The wavelets undergo irregular spatiotemporal patterns of fibrillatory conduction[7, 37]. In the isolated guinea pig heart, the presence of a fast and stable rotor driving fibrillatory activity has been demonstrated to correlate with gradients in I_{K1} density between the left and right ventricles[57]. Hou *et al*., demonstrated that

overexpression of hERG in an NRVM system stabilizes and accelerates rotors[113]. Reduction of I_{Kr} in the pig atria by transfection of the G628S-hERG mutant significantly reduced the ability to induce atrial fibrillation by burst pacing[151]. Thus there is a link between fibrillatory frequency and APD. However, details regarding the relationship between the spatial organization of excitation and the spatial I_{Kr} distribution were lacking. Here we demonstrate that regional I_{Kr} heterogeneity can be a mechanism of rotor formation, wavebreak and fibrillatory conduction. Importantly, only rotors localized within higher hERG expression regions and whose frequency exceeded ~13 Hz resulted in wavebreaks and fibrillatory conduction. On the other hand, no fibrillatory activity was observed in cases in which a single driving rotor resided in lower I_{Kr} regions or in uniformly infected monolayers, regardless of the frequency of the rotors. While hERG overexpression does not transiently hyperpolarize the MDP in all cell types[114, 115], in NRVM it has been shown previously to both transiently hyperpolarize the MDP and abbreviate APD, both factors contributing to rotor acceleration[113]. Our numerical results indicate that spatial APD dispersion induced by MDP heterogeneity alone does not result in fibrillatory conduction. Therefore, in these monolayers, regional I_{Kr} heterogeneity leading to APD dispersion is the primary mechanism of the fibrillatory activity.

2.4.5 Clinical Relevance

Ion channel gradients have been suggested to exist in the atria of patients with atrial fibrillation[84, 172]. This, together with the recent demonstration by Narayan *et al.* that AF in humans may result of long-standing rotors with fibrillatory conduction to the surrounding atrium[116], strongly supports the conclusion that rotors are the primary drivers of AF,

at least in some patients. Most important, brief radiofrequency ablation at or near the center of rotation alone acutely terminated AF[116], this provides a solid rationale for investigating the mechanisms of wavebreak, rotor formation and fibrillatory conduction. While our results cannot be extrapolated directly to the clinical situation they demonstrate that heterogeneity in the atrium in the form of spatially distributed APD gradients constitutes a likely arrhythmogenic substrate in which waves emanating at high frequency from either focal or reentrant sources results in the turbulent electrical activation which manifests as fibrillatory conduction.

Gain-of-function of I_{Kr} abbreviates QT interval (SQT1) and generates heterogeneous APD shortening and refractoriness[110, 111]. On the other hand, recently it was reported that viral transfer of a hERG mutant (KCNH2-G628S) associated with long QT syndrome eliminated AF in porcine model by prolonging atrial APD[151]. As both gain- and loss-of-function mutations in hERG exacerbate APD heterogeneity, spatially distributed hERG gradients may be very relevant to understanding the mechanisms of these arrhythmias. It is important to note, however, that APD gradient secondary to heterogeneous hERG expression is by no means the only the only substrate conducive to wavebreak and high-frequency rotor formation leading to fibrillatory conduction. We have previously shown in a similar monolayer model overexpressing KvLQT1 and minK, that I_{Ks}-mediated postrepolarization refractoriness can also promote wavebreak formation and fibrillatory conduction during rapid pacing or sustained high-frequency reentry by a completely different mechanism[107]. In agreement with such data, Shimizu *et al.*[173] found that the I_{Kr} blocker D-sotalol increased transmural inhomogeneity in APD and was proarrhythmic, while an I_{Ks} blocker uniformly increased APD and was proarrhythmic only after the addition of isoproterenol. Taken together,

these findings suggest that APD heterogeneity and/or post-repolarization refractoriness are both important but separate determinant factors in the mechanisms of wavebreak, rotor formation and fibrillatory conduction. Consequently, investigating the functional effect of individual and multiple overlapping ionic gradients in both normal and diseased hearts should lead to a better understanding of the mechanism.

2.4.6 Limitations

Several limitations should be considered: First, cardiac fibrillation occurs in a complex 3D structure and our study was performed in a simplified monolayer system. Nevertheless, we focused on ionic mechanisms of fibrillatory activity. Our methods thus provide a well-controlled model system to study the role of cellular and ionic heterogeneities in the generation of fibrillatory conduction. Such heterogeneities would be very difficult to study in the whole heart. Second, the effect of regional hERG overexpression was examined using NRVMs whose electrical properties are vastly different from those of human myocytes and have slower CV. Clearly, the α-subunit of hERG channels expressed in rodent myocytes differ functionally from adult human channels additionally containing the β-subunit KCNE2 (MiRP1). Nevertheless, we[113, 166, 174] and others[119] have demonstrated that the uniform and heterogeneous NRVM models recapitulate many of the observations in whole adults hearts. Third, we did not address the potential effects hERG overexpression may have on other transmembrane currents. However, based on our experimental and numerical results, we are confident that regional hERG overexpression was an appropriate tool to generate predictable and quantifiable APD gradients. Wavebreak and fibrillatory conduction occur when high-frequency waves generated in the short APD region propagate toward, and impinge on the boundary with the

long APD region, but not the reverse. Fourth, magnetofection may introduce unidentified effects on the electrophysiology of the cells. Yet we feel reassured that this technique did not adversely affect our preparations. Magnetofection of Ad-GFP in the monolayers did not produce any effects on CV, APD or rotor frequency. Finally, varying levels of hERG overexpression were not studied and conclusions regarding changes in I_{Kr} density rely on computer simulations.

Chapter III

Regional Kir2.1 Overexpression Generates Action Potential Duration Dispersion and Bimodal Conduction Velocity Gradients which Serve as a Substrate for Wavebreak and Fibrillatory Conduction

3.1 Introduction

As discussed in previous chapters, clinical and experimental evidence supports the hypothesis that fibrillation results from activity of a small number of high frequency reentrant sources (rotors) localized in one cardiac chamber (atrium/ventricle), with fibrillatory conduction to the other chamber, generating highly complex patterns of local electrical activation[7, 57, 116]. Such spatial dispersion of cardiac electrophysiological properties plays a major role in the regionally distributed frequency gradients often observed during fibrillation. Chamber specific differences in excitability, APD and refractoriness are likely to be the cause of

stabilization of rotors in one cardiac chamber with fibrillatory conduction in the other[57].

The inward rectifying potassium current (I_{K1}) is a major factor in the control of cardiac excitability and arrhythmogenesis[76, 77, 124]. Moreover, Kir2.1, the molecular correlate of I_{K1}, is regionally heterogeneous throughout the cardiac chambers[57, 84, 118]. A recent study in humans has suggested that a larger I_{K1} density in the left atrium explains the dominant left-to-right frequency gradients that prevail in patients with paroxysmal AF[84]. Additionally, mutations in Kir2.1 are associated with SQT3, familial AF, Anderson-Tawil syndrome and CPVT, further identifying Kir2.1 as an important regulator of wave dynamics and a potential therapeutic target[85-88].

Increases in the expression of Kir2.1 lead to an increase in I_{K1}, an abbreviation of APD, hyperpolarization of the resting membrane potential and increases sodium channel availability[57, 76].The balance of increased I_{K1} opposing depolarization, hyperpolarization of the resting membrane potential away from the excitation threshold, and sodium channel availability are the primary determinants of CV and excitability. As such, Kir2.1 overexpression has been shown to increase CV, rotor frequency and stability[76]. However, while I_{K1} can increasingly oppose excitation as more channels are overexpressed, increases in sodium channel availability are limited in their ability to offset the increased I_{K1} by their channel numbers. This suggests that relatively small increases in Kir2.1 overexpression will increase CV while larger amounts of Kir2.1 overexpression will decrease CV. Therefore, we propose that regional I_{K1} heterogeneity has the potential to generate bimodal gradients in CV, which may have a significant impact on fibrillatory dynamics.

In this chapter I focus on the role played by both spatial APD and CV heterogeneity generated by regional Kir2.1 overexpression in the mechanisms of wavebreak and fibrillatory conduction. Since I_{K1} is important in the control of the CV and APD, both important parameters to cardiac fibrillation, we surmise that generating Kir2.1 gradients in a well-

controlled environment may recapitulate the arrhythmogenic substrate that results in wavebreak and rotor formation.

Our central hypothesis is that regional overexpression of Kir2.1 will generate a regional APD gradient, as well as a bimodal CV gradient, both parameters responsible for and contribute to the dynamic patterns of fibrillatory conduction.

To test the above hypothesis, we first reduced the complex problem of fibrillatory propagation in the 3-dimensional heart to a 2-dimensional model using neonatal rat ventricular myocyte (NRVM) monolayers. We then employed a regionally heterogeneous magnetofection of adenovirus containing the Kir2.1 cDNA sequence and generated regional Kir2.1 heterogeneity in a structurally uniform layer of cardiac tissue. The results may provide important information about the nature of arrhythmias in the heart and how we may better prevent and treat them in future.

3.2 Materials and Methods

3.2.1 Ethical Approval

All experiments were approved by the University Committee on the Use and Care of Animals (UCUCA) at the University of Michigan, and the Department of Laboratory Animal Resources. All euthanasia was performed following the recommendations of UCUCA and DLAR-CHUA. All mother rats were either donated to the university “rat recycling program” for use by other investigators, or euthanized by placing the rat in

a carbon dioxide filled chamber, followed by removal of a vital organ (e.g., heart). Neonatal rats were euthanized by quick decapitation.

3.2.2 Myocyte Isolation and Culture

We created neonatal rat ventricular myocyte (NRVM) monolayers as previously described[107, 152]. Ventricles from 1-2 day old neonatal Sprague-Dawley rats (Charles River, Wilmington, MA) were aseptically removed then minced in calcium- and magnesium-free Hanks' Balanced Salt Solution (HBSS, Sigma). Sequential digestion in 0.06% trypsin (Roche Applied Science) and 0.15% pancreatin (Sigma) in HBSS at 36°C was used to further isolate cells. A two hour differential preplating period was used to reduce the presence of non-cardiomyocytes. Medium M199 (Cambrex) containing 10% fetal bovine serum (FBS, Cellgro), 20 U/mL penicillin, 20 µg/mL streptomycin and 100 µmol/L bromodeoxyuridine to inhibit fibroblast proliferation (Sigma) was used to suspend and plate cells. Cells were plated on human collagen type IV (Sigma) coated 35 mm tissue culture dishes at a density of $1x10^6$ cells per monolayer. Cells were kept at 37ºC, 5% CO_2. Media was changed after 24 and 48 hours using the same 5% FBS media. Magnetofection was performed on day 2 in culture. Experiments were conducted at an additional 48 hours, allowing for protein expression.

3.2.3 Magnetofection

Magnetofection was performed on day 2 in culture to infect monolayers with either an Ad-Kir2.1-IRES-GFP containing cDNA sequence of both the WT mouse inward rectifying potassium channel (Kir2.1) and green fluorescent protein (GFP) sequences obtained from

Peter Backx[175] or an Ad-GFP virus[113]. Each virus was first complexed to ViroMag Magnetofection nanoparticles (Boca Scientific, FL); a product normally used for increasing infection efficiency[153]. 0.5 µl of ViroMag was complexed with a specified amount of viral particles depending on the desired level of infection in 200 µl HBSS (Sigma) for 15 minutes then raised to a final transduction volume of 2 ml per monolayer. As illustrated in Figure 2.1, each monolayer was exposed to a Super Magnetic Plate (Boca Scientific, FL) for 1.0 ± 0.5 minutes in the presence of the magnetofection solution. Wholly infected monolayers were placed entirely over the magnet while regionally infected monolayers were created by exposing only half of the lower surface area of the dish containing the monolayer to the magnet. The magnetofection solution was then removed and monolayers were washed twice with and returned to 5% FBS media and given an additional 48 hours to express protein. Uninfected controls were treated similarly using HBSS for 1.0 ± 0.5 minutes.

Determination of the ViroMag and virus concentrations as well as the duration of exposure to magnetic field were determined to be optimal when uninfected regions did not express GFP fluorescence while maintaining infection within infected region and more than 50% of monolayers remained excitable.

3.2.4 Optical Mapping

Experiments were conducted at an additional 46-50 hours after magnetofection. Monolayers were stained with potentiometric dye di-8-ANEPPS (40 µmol/L; Molecular Probes) for 15-25 minutes and then placed on a heating chamber connected to a temperature controller maintained at 37 ± 1°C and continuously superfused with HBSS without

bicarbonate (Sigma) containing (in mmol/L): 1.6 $CaCl_2$, 5.4 KCl, 0.8 $MgSO_4$, 0.4 KH_2PO_4, 4.2 $NaHCO_3$, 136.9 NaCl, 0.3 $NaHPO_4$, 5.5 D-Glucose, and 10 HEPES; pH 7.4 (NaOH). Quiescent monolayers received repetitive stimuli (duration, 5 ms; strength, twice diastolic threshold) applied by a thin extracellular bipolar electrode at increasing frequencies, starting at 1 Hz, until loss of 1:1 capture or initiation of sustained reentry. Five-second high resolution optical mapping movies were obtained at 200 frames/s (LabWindows Acquisition) using an 80 × 80 pixel CCD camera (SciMeasure Analytical Systems; Decatur, GA). Signals were amplified, filtered, and digitized for offline analysis. No electromechanical uncouplers were used.

3.2.5 Optical Data Analysis

Dominant frequency (DF) maps were constructed by taking the Fast Fourier Transformation of the fluorescence signal at each pixel[117, 164, 165]. APD and conduction velocity (CV) measurements used average signals obtained from individual 5 second optical movies recorded during repetitive pacing at varying frequencies. Movies were filtered as previously described[113]. APD color maps were constructed by measuring the time between the upstroke and 50 and 75% of repolarization in each pixel. For CV measurements, activation times were calculated for each pixel, and local conduction vectors were determined as described[113].

3.2.6 Statistical Analyses

For statistics analysis, we used one-way ANOVA with a Bonferroni correction or paired Student t-tests where appropriate (Origin software version 7.0). Values are expressed as mean ± SEM. A value of $p<0.05$ was considered significant. N refers to the number of dissociations and n refers to the number of monolayers.

3.2.7 Computer Simulations

A mathematical model of NRVM was adapted to experimental data, as previously described in detail[113, 176], with minor modifications. A 2D disk-shaped sheet used a Cartesian mesh of 352 x 352 nodes with a spatial resolution of 100 μm that contains a 35 mm diameter disk-shaped active domain in its center, with a non-diffusive outer domain boundary was used to simulate a NRVM monolayer of tissue. The area outside of the monolayer was implemented with passive and non-diffusive nodes for ease of integration. The membrane model at each node was solved by the finite volume method with a time-step of 10 μs and no-flux boundary conditions, as described previously by Zlochiver *et al*.[166] G_{K1} maximal conductance was either set as homogeneous (whole G_{K1}, $1xG_{K1}$–uninfected or $5xG_{K1}$–infected) or varied spatially across the model (regional G_{K1} model). To simulate the spatial gradient in G_{K1} expression along the model we implemented the Boltzmann best fit of the Kir2.1-IRES-GFP fluorescence data obtained in the experiments as described previously. A native level of G_{K1} was used in the 'uninfected' region ($1xG_{K1}$). G_{K1} was increased to 1.5x, 2x, 5x and $10xG_{K1}$ basal levels within 'infected region' of the model. Reentry was induced via S1-S2 cross-field stimulation protocol. DF and CV profiles were determined as in experiments (See the Appendix for further details).

3.3 Results

3.3.1 Regional I_{K1} Heterogeneity: Computer Simulations

Determining how regional Kir2.1 heterogeneity influences fibrillatory dynamics is a complicated problem. Using a 2-dimentional mathematical

model we were able to simulate regional electrical heterogeneity in a sheet of neonatal rat ventricular myocytes by regionally increasing the level of I_{K1} conductance, G_{K1}. Increasing G_{K1} increases rotor frequency in uniform monolayers; $1xG_{K1}$ (or the native 'uninfected' level of G_{K1}) produced rotors of 11.9 Hz, while rotors in $5xG_{K1}$ monolayers produced frequencies of 18.4 Hz. Rotors generated in the $1xG_{K1}$ region of simulations with regional $1x\text{-}5xG_{K1}$ heterogeneity did not generate wavebreak or regional DF domains (11.9 Hz). Rotors generated in the $5xG_{K1}$ region generated patterns of wavebreak which occurred at the gradient region between 1x and $5xG_{K1}$, as well as multiple frequency domains within the $1xG_{K1}$ region (upper portion of Figure 3.1.A). Additionally, pacing from the $5xG_{K1}$ region demonstrated a frequency dependent effect on the generation of wavebreak and patterns of fibrillatory conduction. Pacing at 10 Hz did not generate wavebreak, while 20 Hz did, generating a pattern of almost 2:1 block at the portion of gradient closest to the pacing site (Figure 3.1.B).

3.3.2 APD and CV in Response to Regional Increase in I_{K1}: Computer Simulations

To elucidate the mechanism(s) responsible for the patterns of wavebreak observed in these simulations, we examined how regional increases in I_{K1} effects CV and APD. Figure 3.2 shows how non-uniform G_{K1} distribution results in APD heterogeneity. We found that as the level of G_{K1} is increased in the infected region, APD_{90} within that region decreases. Regional $1x\text{-}5xG_{K1}$ heterogeneity generates an APD_{75} gradient of 29.8 ms and an APD_{90} gradient of 40 ms.

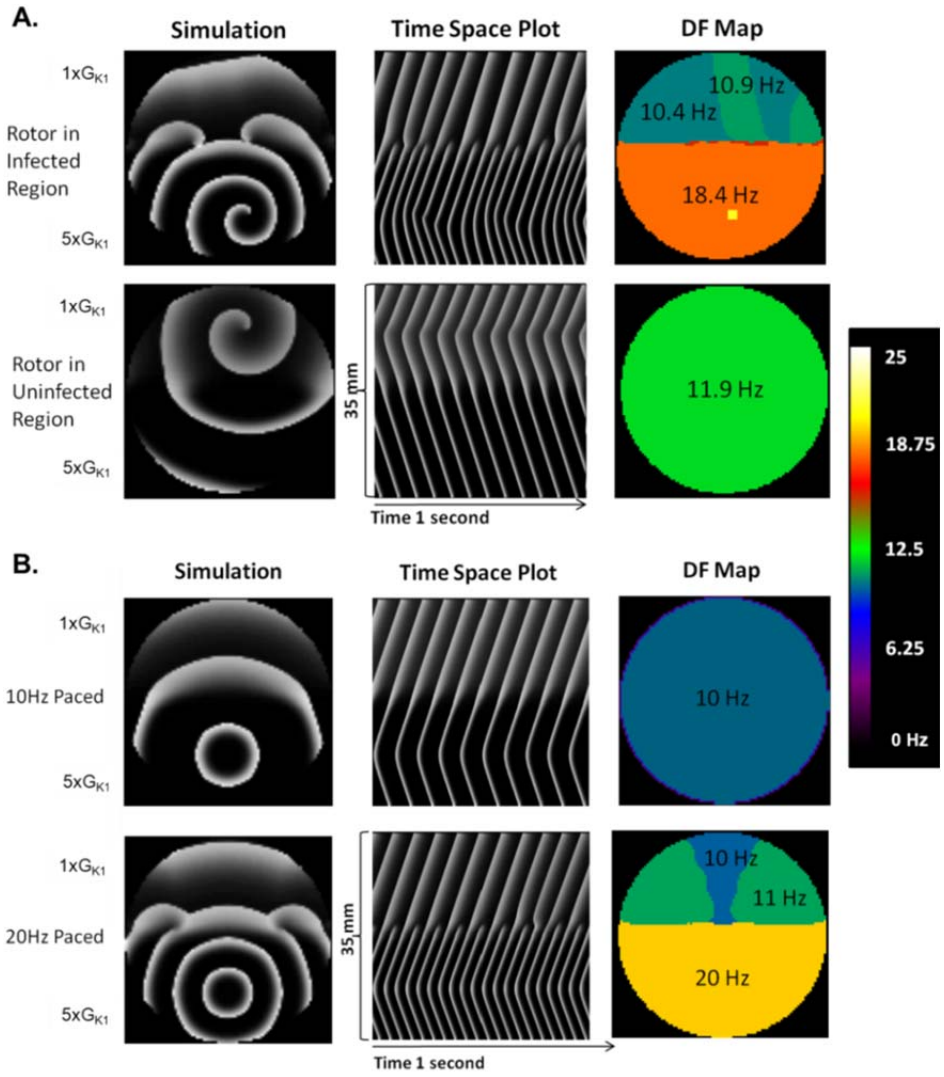

Figure 3.1. **Regional G_{K1} Heterogeneity Generates Wavebreak. A.** Rotors localized within the 5xG_{K1} region (top row) generate wavebreak and patterns of fibrillatory conduction in the 1xG_{K1} region as seen on the time space plot and DF map; (Bottom row) rotors localized within the 1xG_{K1} region activate monolayer uniformly. **B.** Pacing at 10 Hz from the 5xG_{K1} region did not generate wavebreak (top row); pacing at 20 Hz does as seen by the time space plot and DF map (bottom row).

In addition to demonstrating a regional APD heterogeneity, our simulations show how regional I_{K1} heterogeneity also plays an important role in the control of CV. Figure 3.3 shows CV maps of 4 regional G_{K1} simulations with progressively increasing levels of G_{K1} in the infected

region. Unlike APD, which exhibited a sigmoidal decrease as you go into the region of increased G_{K1}; at 10 Hz our simulations show a spatially bimodal effect on CV profiles. In the cases of relatively low G_{K1} heterogeneity 1x-1.5xG_{K1} (purple) or 1x-2xG_{K1} (red) the CV profile is mostly sigmoidal, increasing as levels of G_{K1} increase. However, as the G_{K1} gradient becomes larger (1x-5xG_{K1}), we observe a bimodal CV which peaks at the gradient region and then returns to a slower CV in the 5xG_{K1} region. Finally, looking at the 1x-10xG_{K1} case there is a bimodal CV profile with an even slower CV within the 10xG_{K1} region.

In order to understand the mechanism for this bimodal CV we used a model of a single neonatal rat ventricular cell paced at 10 Hz in which we progressively increased the levels of G_{K1}. As expected, increases in G_{K1} progressively shorten APD and hyperpolarize the resting membrane potential.

In accordance with previous studies demonstrating the interaction of I_{K1} on I_{Na}, we observed an increase of sodium channel availability as G_{K1} was increased (Figure 3.4.B). This alone cannot explain the bimodal effect we observed in CV in Figure 3.3. However, by looking at the relative progression of the slope conductance of G_{K1} and the sodium channel availability $((h*j)_{max})$ as the level of G_{K1} is increased (Figure 3.5) we can explain the bimodal CV. The slope conductance of G_{K1} increases linearly as G_{K1} is increases. However, sodium channel availability does not increase linearly with G_{K1}. A small increase in G_{K1} creates a drastic increase in sodium channel availability, while a further increase in G_{K1} does not generate an equivalently large increase. As these two forces oppose one another in their control of the upstroke velocity (dV/dt_{max}), the net effect of these changes generates a bimodal quality in the upstroke velocity. At low levels of G_{K1} there is a great effect of sodium channel availability while only a minor effect on the slope conductance; thus

sodium channel availability predominates, causing an increase in the upstroke velocity. At higher levels of G_{K1} there is less additional increase in sodium channel availability compared to the stably increasing effect on slope conductance. This results in G_{K1} having a predominant effect over sodium channel availability and we see a decrease in the upstroke velocity. Taken together these simulated results suggest that regional I_{K1} heterogeneity generates both an APD gradient as well as a bimodal CV gradient.

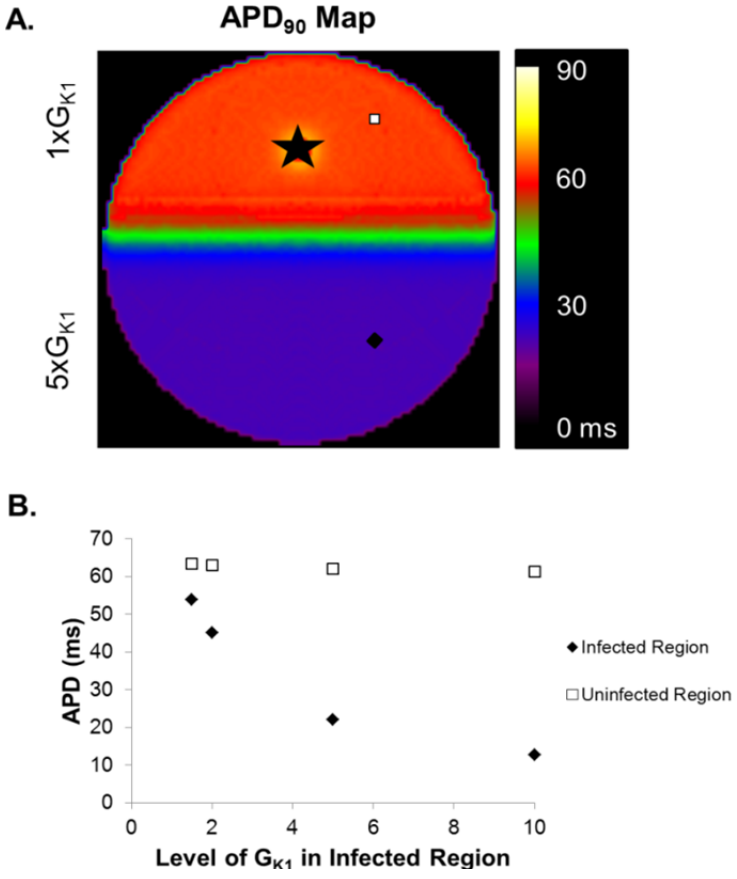

Figure 3.2. Regional G_{K1} Heterogeneity Generates Regional APD Heterogeneity. **A.** APD_{90} map of an regional 1x-5x G_{K1} simulation paced from the uninfected region (star) at 10 Hz. **B.** APD_{90} taken from both infected ($5xG_{K1}$, black diamonds) and uninfected ($1xG_{K1}$, white squares) in regional simulations with increasing levels of G_{K1} within the infected region.

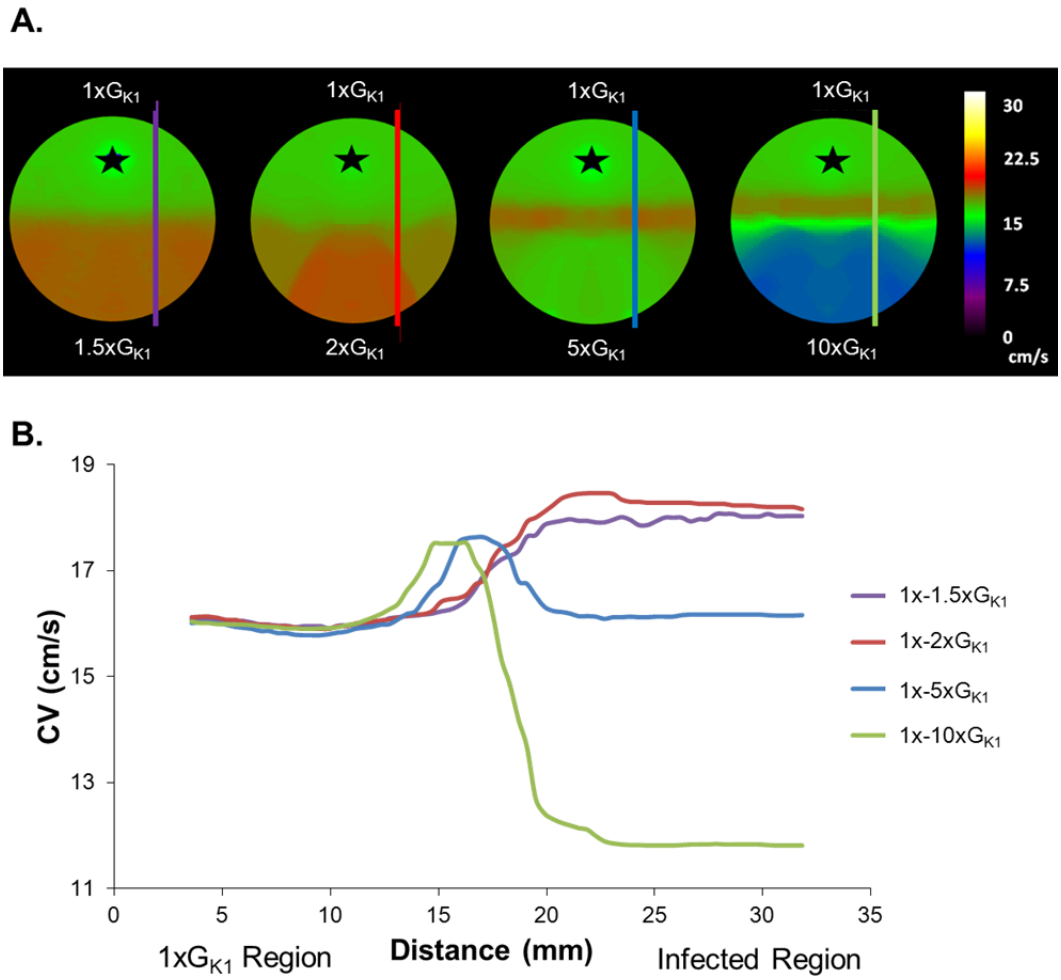

Figure 3.3. Regional G_{K1} Heterogeneity Generates a Bimodal CV Gradient. **A.** CV maps of regional G_{K1} simulations being paced at 10 Hz from the star in the uninfected region (1xG_{K1}). **B.** CV profiles taken along the vertical colored lines in A demonstrating how the CV profile changes from a sigmoidal profile at low levels of regional G_{K1} heterogeneity (1x-1.5xG_{K1}/purple and 1x-2xG_{K1}/red) to a bimodal spatial CV profile when G_{K1} is above 2xG_{K1} in the infected region (1x-5xG_{K1}/blue and 1x-10xG_{K1}/green).

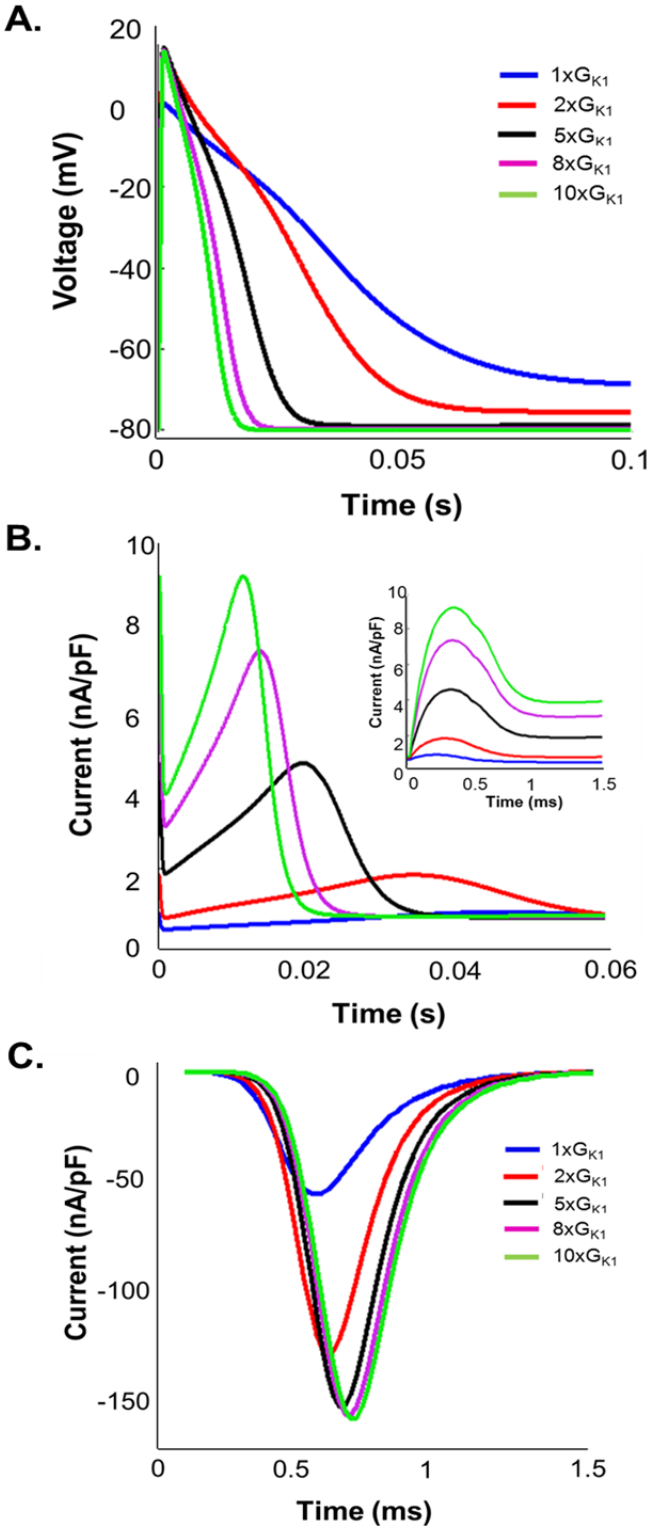

Figure 3.4. Increasing G_{K1} in Single Cell Simulations. A. Action potentials from single cell simulations with increasing levels of G_{K1} paced at 10 Hz. APD shortens and resting membrane potential becomes more hyperpolarized as G_{K1} is increased. **B.** I_{K1} throughout the progression of the action potential. **C.** I_{Na} in response to increasing levels of G_{K1}. As G_{K1} was increased it resulted in an increase in I_{Na}.

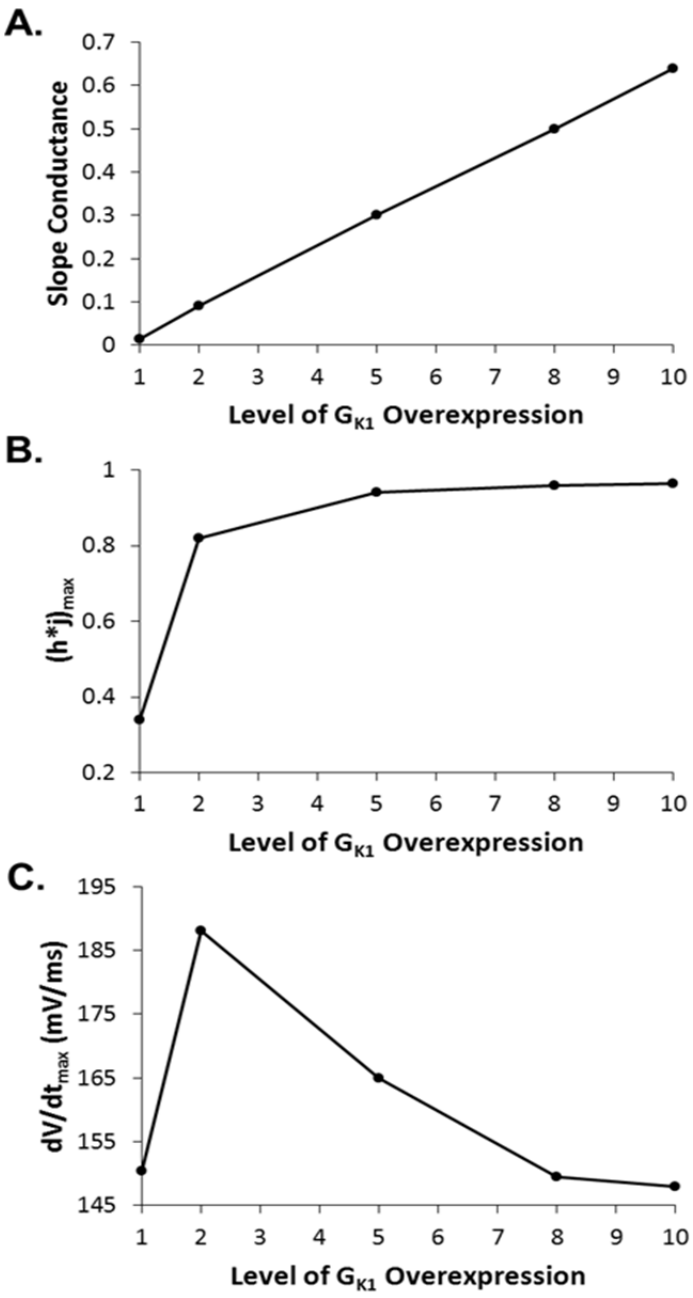

Figure 3.5. Mechanism of Bimodal CV. A. Slope conductance of I_{K1} as level of G_{K1} is increased. **B.** Sodium Channel availability ($(h*j)_{max}$) as level of G_{K1} is increased. **C.** Upstroke velocity (dV/dt_{max}) as G_{K1} is increased generates a bimodal effect. At low levels of G_{K1} there is a greater effect on sodium channel availability and only a modest effect on I_{K1} conductance resulting in a faster upstroke velocity. As G_{K1} is increased to $5xG_{K1}$ the greater effect is on increasing I_{K1}'s slope conductance resulting in a decrease in the cells upstroke velocity.

3.3.3 Experimental Model – Kir2.1 Overexpression

Using a NRVM model we characterized the effect increasing levels of Kir2.1 has on APD, CV and rotor frequency. Increasing levels of Kir2.1 overexpression lead to a progressive shortening of the APD_{50} and APD_{75}. Figure 3.6 shows APD_{75} restitution curves of uninfected monolayers (UN, red) and monolayers at increasing levels of Kir2.1 overexpression[31]. Kir2.1 infection levels are as follows; 0.01 µl (yellow), 0.03 µl (green), 0.05 µl (dark green), 0.07 µl (blue), 0.1 µl (purple) and 0.124 µl of Ad-Kir2.1 (black). At each pacing frequency (i.e., 1/basic cycle length, BCL), uninfected monolayers had significantly longer APD's than the group with the highest Kir2.1 expression; APD_{75} at BCL=1000 ms: 104.5 ± 2.8 ms vs. 86.6 ± 3.1 ms and at BCL=100 ms: 77.9 ± 2.5 ms vs. 68.3 ± 1.7 ms ($p<0.005$, the same was true for APD_{50} at all BCLs surveyed; data not shown). In validation of the numerical predictions, the experimental results demonstrate Kir2.1-dependent APD shortening independent of the BCL.

In addition to the bimodal CV observed at 10 Hz in simulations, our experimental model demonstrates that the bimodal CV profile is a frequency dependent phenomenon, as illustrated in Figure 3.7. In panel A, the superimposed CV restitution curves show a decrease in CV from the uninfected group to increased levels of Kir2.1 infection at BCLs between 200 and 1000 ms. Uninfected monolayers have the fastest CV (25 cm/s, n=17) while the monolayers infeceted with 0.124 µl Ad-Kir2.1 had one of the slowest CVs (21 cm/s, n=8, $p<0.05$)[32]. However, as better illustrated by the respective best fit lines in panel B, a completely different picture

[31] Levels of Kir2.1 are expressed in units of µl of Ad-Kir2.1-IRES-GFP rather than MOI as our magnetofection technque has signifcantly altered the probability a viral particle will infect a target cell, for simplicity of the text I will describe the level of overexpression in terms of µl of Ad-Kir2.1.

[32] 0.05 µl and 0.07 µl Ad-Kir2.1 also had the slowest CV of 21 cm/s, 0.1 µl had an intermediate CV of 23 cm/s (n=14, 15, 12).

emerges at BCLs < 200 ms. While at a BCL of 1000 ms there was a progessive decrease in CV; at BCLs shorter than 200 ms, we observed a cross over of the restitution curves demonstrating a bimodal effect on CV. At BCL=100 ms the lowest levels of Kir2.1 are slowest around 18 cm/s.

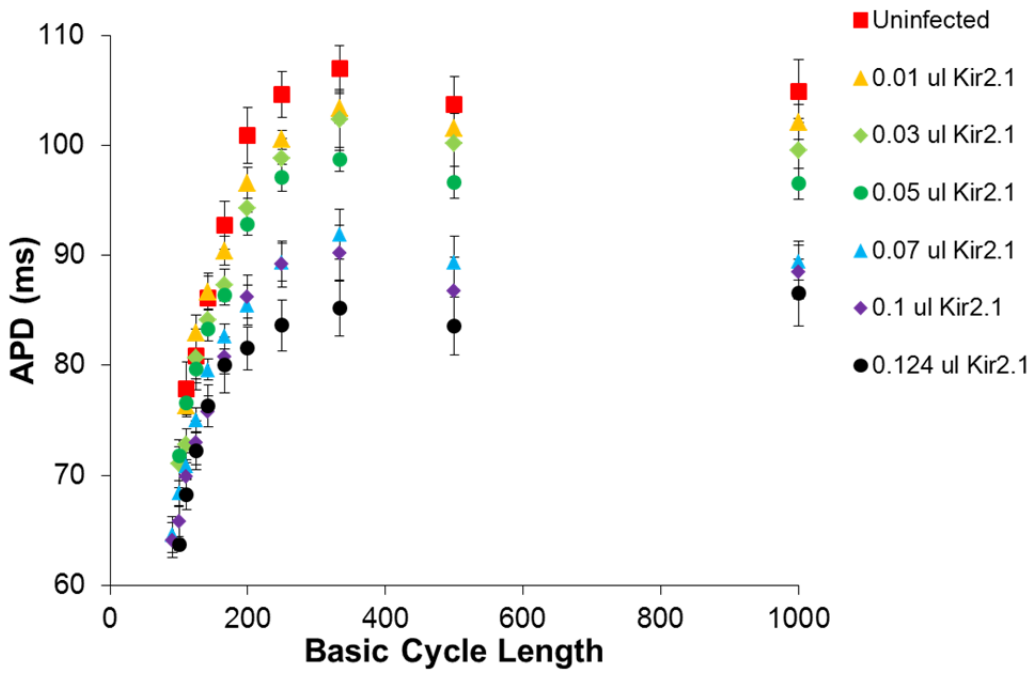

Figure 3.6. APD_{75} Restitution Curve. APD_{75} restitution curves of uninfected (red, n=17), 0.01 µl Ad-Kir2.1 (yellow, n=12), 0.03 µl Ad-Kir2.1 (green, n=17), 0.05 µl Ad-Kir2.1 (dark green, n=14), 0.07 µl Ad-Kir2.1 (blue, n=13), 0.1 µl Ad-Kir2.1 (purple, n=12) and 0.124 µl Ad-Kir2.1 (black, n=8) monolayer groups.

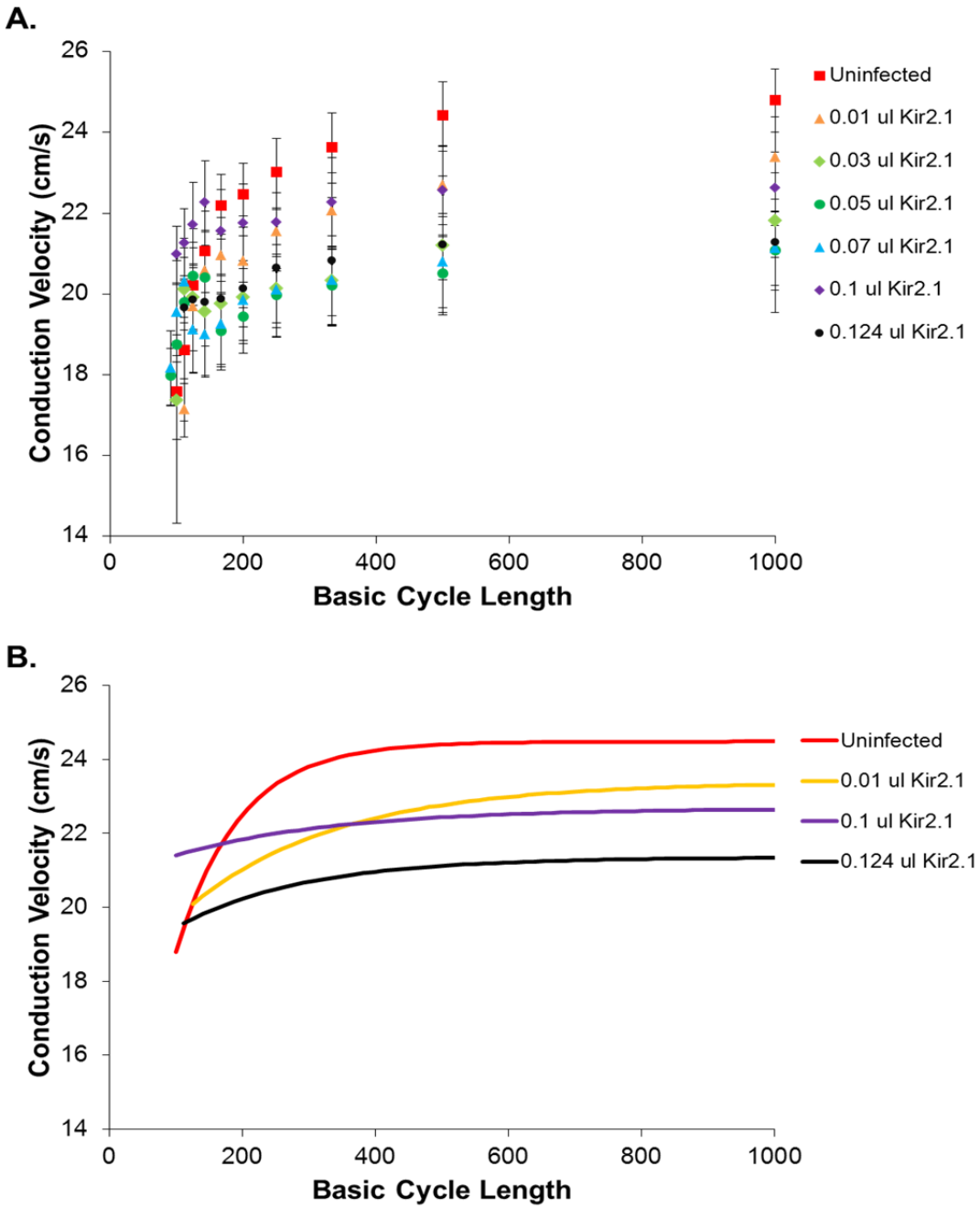

Figure 3.7. CV Restitution Curves. A. CV restitution curves of uninfected (red, n=17), 0.01 µl Ad-Kir2.1 (yellow, n=12), 0.03 µl Ad-Kir2.1 (green, n=17), 0.05 µl Ad-Kir2.1 (dark green, n=14), 0.07 µl Ad-Kir2.1 (blue, n=13), 0.1 µl Ad-Kir2.1 (purple, n=12) and 0.124 µl Ad-Kir2.1 (black, n=8) monolayer groups. **B.** Best fit lines of groups expressing the lowest levels of Kir2.1 (UN and 0.01 µl Ad-Kir2.1) and highest levels of Kir2.1 (0.1 µl and 0.124 µl Ad-Kir2.1).

On the other hand the fastest CV of 21 cm/s is seen for the second highest level of Kir2.1 (0.1 µl), while the highest level of Kir2.1 (0.124 µl) has a reduced CV of 19.6 cm/s. More important than the absolute value of the CV, is the shape of the CV restitution curve for each level of expression, which can explain the frequency-dependent effect on bimodal CV. Again, Figure 3.7.B shows the best fits for 4 of the 7 groups, the two lowest and the two highest levels of Kir2.1. Uninfected monolayers had the steepest restitution, with a rapid decline in CV as the BCL was reduced (an average drop of 6.25 cm/s between 1000 and 100 ms). Monolayers with higher levels of Kir2.1 had shallow CV restitution curves, with significantly smaller drops in CV (1.36 and 1.63 cm/s for 0.1 µl and 0.124 µl Ad-Kir2.1, respectively, $p<0.005$). Even though the highest level of Kir2.1 (0.124 µl Ad-Kir2.1) had a similar decline as 0.1 µl Ad-Kir2.1, at our range of pacing frequencies, it never surpassed the magnitude of 0.1 µl Ad-Kir2.1's CVs. In line with the model predictions, the latter effect suggested that at this level of overexpression the role of potassium conductance overcame the additional benefits of increased sodium channel availability and therefore there was a net decrease in upstroke velocity.

A bimodal effect of Kir2.1 overexpression could also be observed in the maximum dominant frequency (DF_{max}) of the spontaneous rotor activity, as illustrated by Figure 3.8. Importantly, small increases in Kir2.1 had a negligible effect on rotor frequency, whereas intermediate levels of Kir2.1 overexpression resulted in faster rotor frequencies. The largest Kir2.1 expression levels had intermediate effects. The highest levels of Kir2.1 also had the largest proportion of unexcitable monolayers.

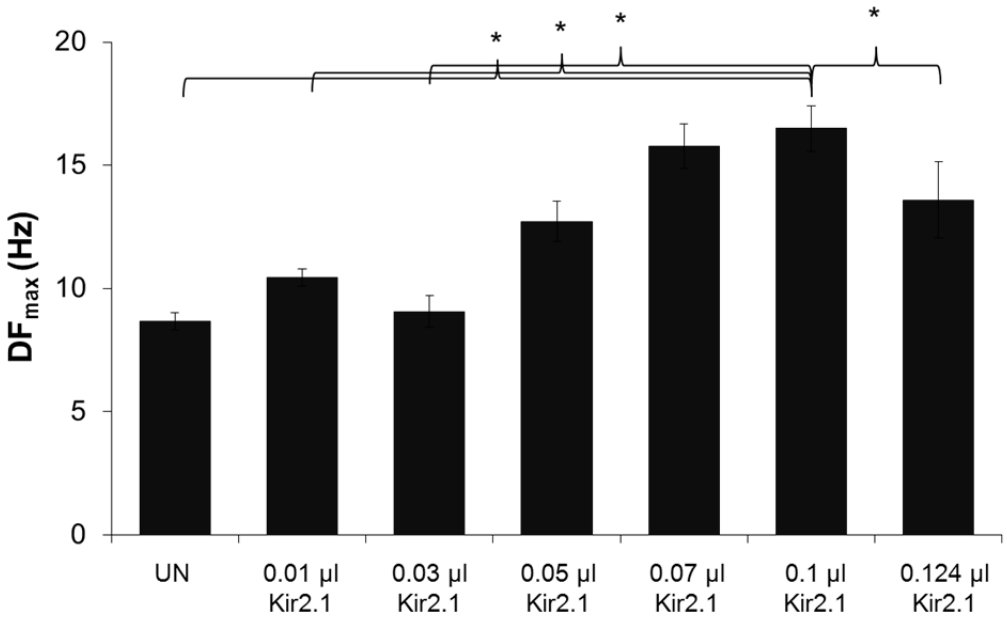

Figure 3.8. DF_{max} as Kir2.1 is Increased. DF_{max} of uninfected (n=4) and monolayers overexpressing 0.01 µl Ad-Kir2.1 (n=4), 0.03 µl Ad-Kir2.1 (n=5), 0.05 µl Ad-Kir2.1 (n=10), 0.07 µl Ad-Kir2.1 (n=10), 0.1 µl Ad-Kir2.1 (n=16) and 0.124 µl Ad-Kir2.1 (n=9). DF_{max} peaks in monolayers overexpressing 0.1 µl Kir2.1 and then decreases at 0.124 µl Ad-Kir2.1. (*$p<0.05$). Uninfected, 0.01 µl and 0.03 µl Ad-Kir2.1 are aslo significantly less than 0.07 µl and 0.1 µl but not 0.124 µl Ad-Kir2.1 ($p<0.05$, ANOVA).

To determine whether the bimodal pattern of DF_{max} was related to the local CV, we measured the CV at a constant distance of 0.9 mm from the core in monolayers with a single rotor and varying levels of homogeneous Kir2.1 overexpression. CV in the UN monolayers was 2.6 cm/s (n=4). In monolayers infected with 0.05 µl Ad-Kir2.1 it increased to 3.1 cm/s (n=5), and in those infected with 0.1 µl Ad-Kir2.1, it increased further to 3.9 cm/s (n=5). However, at 0.124 µl Ad-Kir2.1, the CV increased only to 3.2 cm/s (n=6). Again these date show a bimodal effect, CV peaking at the second highest level of Kir2.1 overexpression.

These data demonstrate how APD, CV and rotor frequency are influenced by increasing levels of Kir2.1 overexpression. APD decreases as Kir2.1 increases. At low frequencies so does CV, while at high frequencies CV changes bimodally in response to Kir2.1 overexpression, peaking at an intermediate level of Kir2.1. Rotor frequency also responds in a bimodal fasion to levels of Kir2.1 overexpression mirroring the effects demonstrated for CV.

3.3.4 Regional Kir2.1: Mechanisms of Wavebreak and Fibrillatory Conduction

Utilizing the regional magnetofection technique described in the Methods section and the previous chapter, we generated monolayers with regional Kir2.1 heterogeneity using the highest level (0.124 µl) of Kir2.1 adenoviral infection. An example of one such monolayer, panel A of Figure 3.9, shows an APD map displaying a spatially distributed 20 ms APD gradient. Representative optical action potentials from each of the two regions are superimposed in panel B and composite data comparing APDs of regionally infected, uninfected and whole infected monolayers are presented in panel C. Only R-Kir2.1 had significant APD heterogeneity (* $p<0.05$).

In panel A of Figure 3.10 we compare APD restitution curves obtained from uninfected (red) and infected (black) regions. Whether measured at 50% or 75% repolarization, APD was always shorter in the infected regions compared to uninfected regions. The basic cycle length dependence on APD was always monotonic.

Similarly to APD, we observed no regional CV heterogeneities in UN, W-GFP, R-GFP and W-Kir2.1 monolayers at any BCL (data not shown). However, as illustrated in panel B of Figure 3.10, in R-Kir2.1 monolayers CV restitution was vastly different in the infected versus

uninfected regions. In the uninfected region the curve was steep and monotonic, while the curve in the infected region was flat; this resulted in a cross-over of the two curves at relatively short BCLs. Correspondingly, at BCLs longer than 166 ms (i.e., below 6 Hz) CV in the uninfected region was significantly faster than the infected region. On the other hand, at BCLs between 125 and 148 ms (7 and 8 Hz, respectively) CV was similar in the two regions, while at BCL 99-110 ms (9-11 Hz) the velocity in the Kir2.1 overexpressing region was significantly faster than the uninfected region ($p<0.05$ Student paired t-test).

Likewise, as shown in Figure 3.11, APD dispersion, measured as the average difference between infected and uninfected regions, remained relatively constant at long BCLs (panel A) and declined monotonically at progressively shortened BCLs. However, CV dispersion initially declined toward zero at BCL=143 ms, but increased sharply at shorter BCLs. This occurred to such an extent that at BCL=100 ms CV dispersion was significantly greater than at BCL=1000 ms ($p<0.02$, Student t-test). Not only do these results demonstrate how regional Kir2.1 overexpression creates both regional APD and CV heterogeneity, it also distinguishes a frequency dependence in the CV dispersion; indicating that as frequencies change so will the regional CV profile.

Both regional G_{K1} simulations and increasing levels of Kir2.1 overexpression predict a bimodal spatial CV gradient with regional Kir2.1 overexpression. Observing the shape of the wavefront, we can clearly see how within the gradient region the wavefront propagates further from the stimulus site than the wavefront in either uninfected or infected regions (Figure 3.12). CV dispersion analysis suggests that the bimodal spatial CV is most prominent above 8 Hz (BCL=125 ms). At this frequency the CV in the gradient region was significantly faster than the CV in the Kir2.1

overexpressing region, confirming the presence of a bimodal spatial CV gradient induced by regional Kir2.1 overexpression.

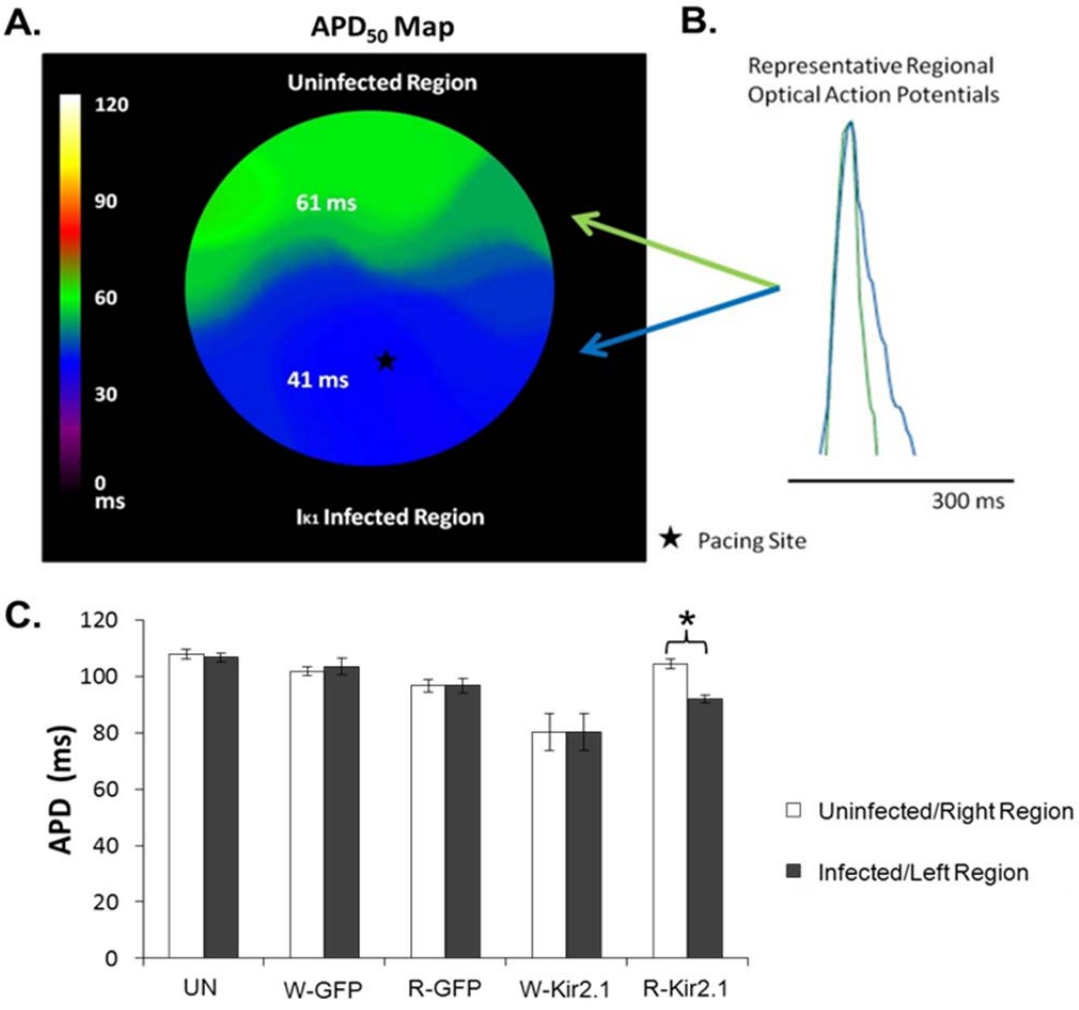

Figure 3.9. Regional APD Heterogeneity. A. APD_{50} map showing regional APD domains. **B.** Representative action potentials taken from the uninfected region (green) and infected region (blue). **C.** APD_{75} regional comparisons during 1 Hz pacing from the gradient. UN, W-GFP, R-GFP and uninfected region of the R-Kir2.1 group were significantly longer than the W-Kir2.1 regions (statistics not shown). From left to right, n = 8, 3, 9, 4, 12.

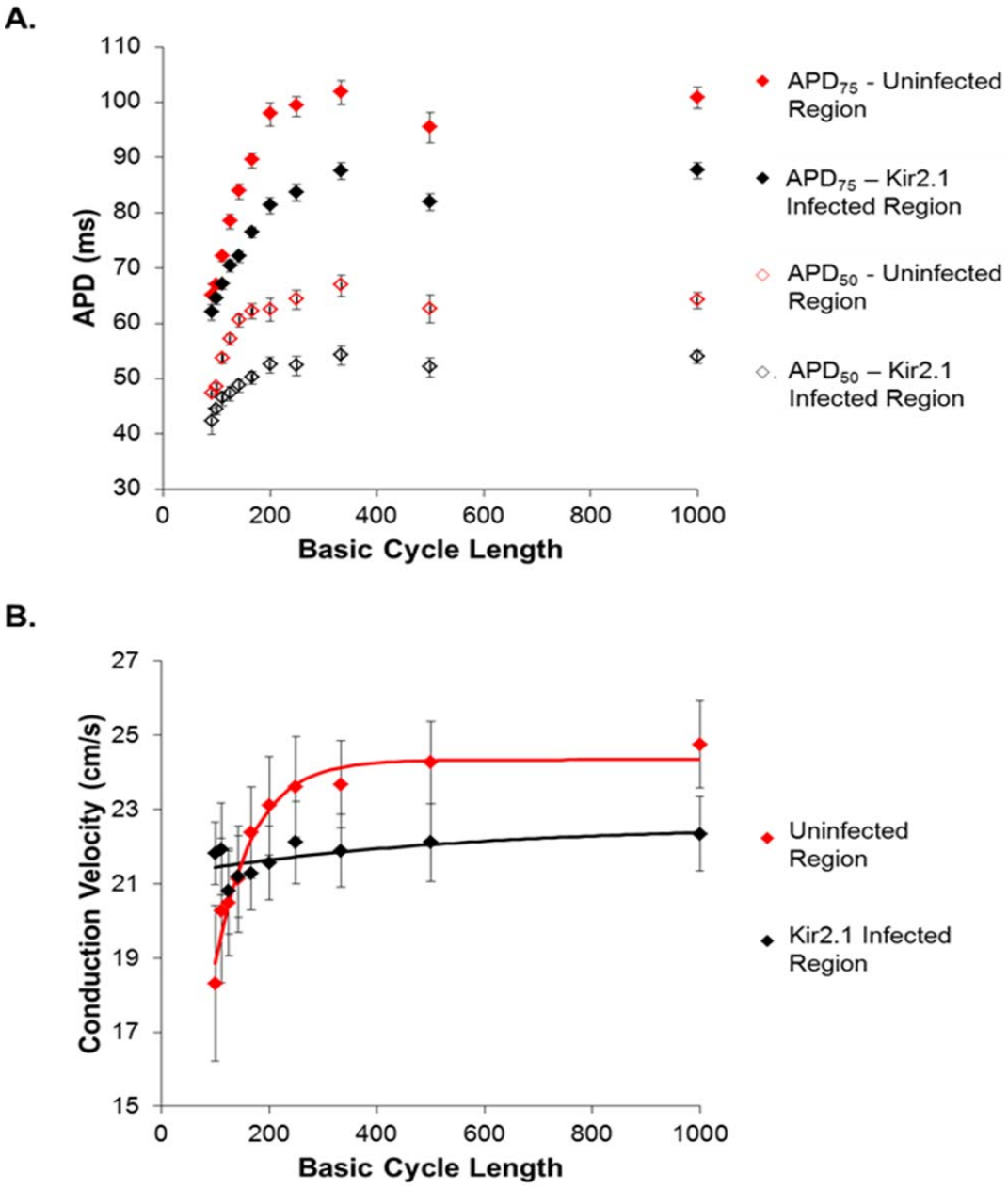

Figure 3.10. R-Kir2.1 – APD and CV Restitution Curves. A. R-Kir2.1 APD restitution curves taken from uninfected region (red) and infected regions (black); APD_{75} are filled, APD_{50} are empty. Student paired t-test reveals significant regional differences at all frequencies for both APD_{75} and APD_{50} (n=12). **B.** Regional CV comparison, from 1-6 Hz the uninfected region (red) have faster CV than the Kir2.1 infected region (black) while from 9-11 Hz the Kir2.1 infected region is significantly faster (Student paired t-test, $p<0.05$).

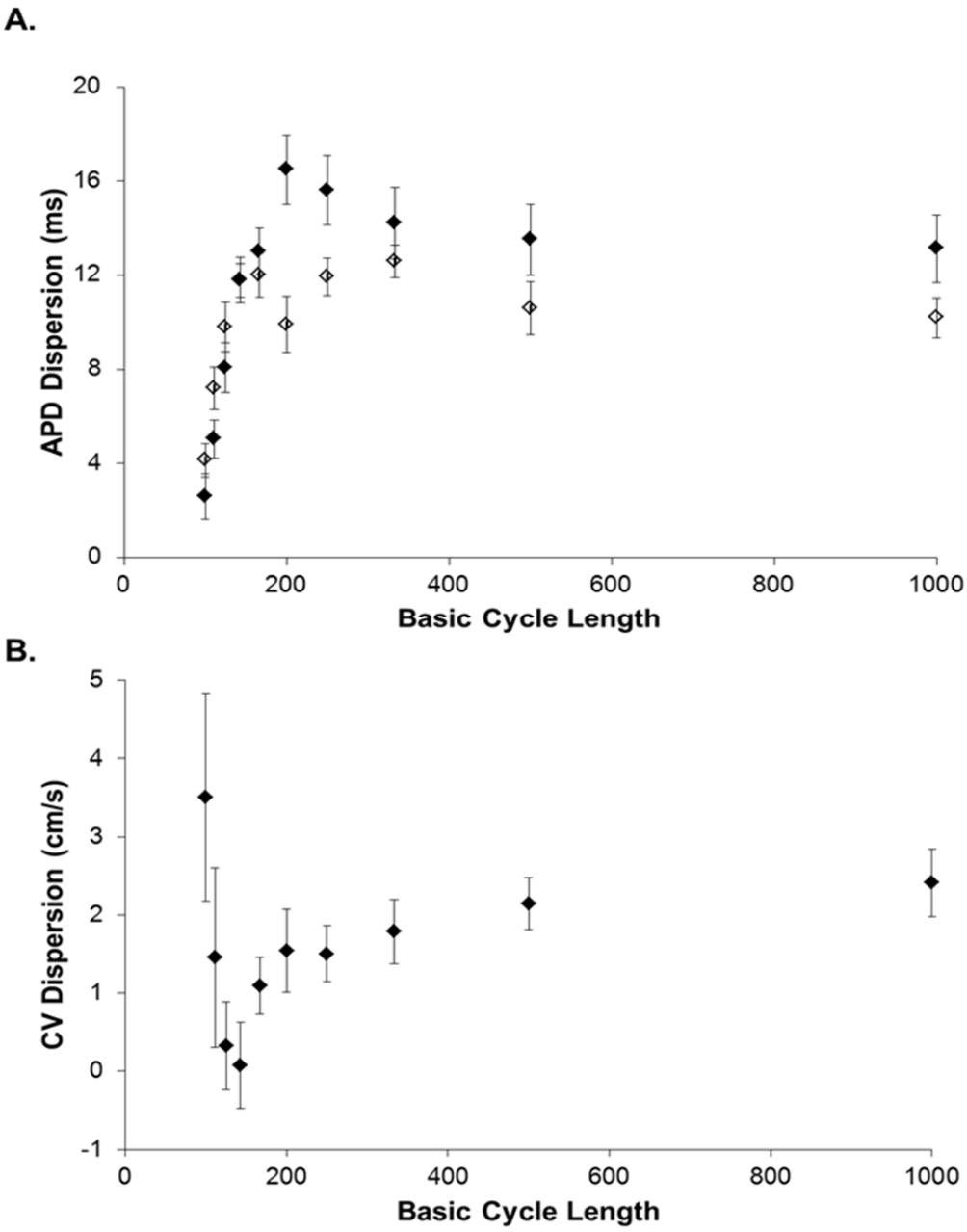

Figure 3.11. Frequency Dependence of APD and CV Dispersion. A. Frequency dependence of APD_{75} (solid diamonds) and APD_{50} (open diamonds) dispersion. **B.** Frequency dependence of CV dispersion initially declines, increases above 6 Hz, at this point the CV within the infected region overtakes the CV in the uninfected region.

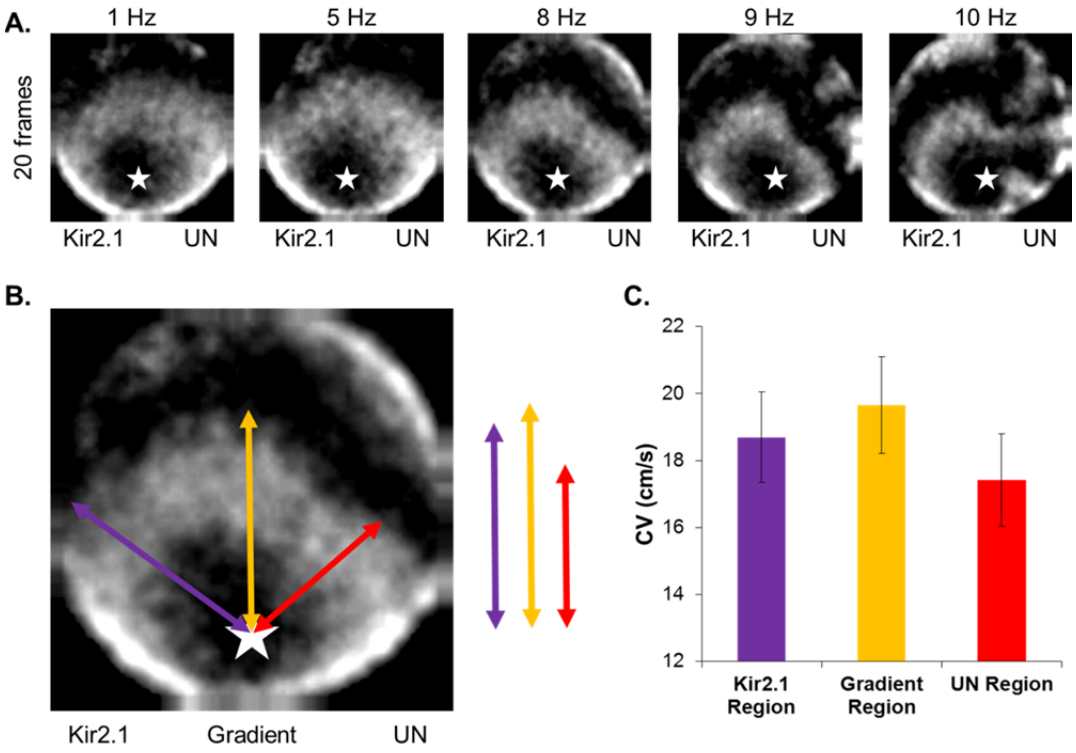

Figure 3.12. Spatial Bimodal CV Gradient. A. R-Kir2.1 paced from infection gradient (star) at 1, 5, 8, 9 and 10 Hz, images taken 20 frames after the start of the wave. Above 8 Hz the CV in the gradient region is fastest, by 9 and 10 Hz 1:1 conduction is lost and fibrillatory conduction is observed. **B.-C.** Example and quantification of CV vectors at 8 Hz. Gradient region is significantly faster than Kir2.1 infected region ($p<0.05$, Student paired t-test).

Having experimentally demonstrated that regional Kir2.1 overexpression generates both APD and bimodal spatial and frequency-dependent CV gradients; the question becomes what influence do such overlapping gradients have on the initiation of wavebreak and fibrillatory conduction. As illustrated in Figure 3.12, pacing above 8 Hz from the gradient (or from the infected regions, data not shown) tended to generate wavebreak and patterns of fibrillatory conduction within the uninfected

region only. No regional patterns of wavebreak were achieved at any pacing frequency from any other group.

3.3.5 Regional Kir2.1 Generates Wavebreak and Fibrillatory Conduction: Experiments

Regional Kir2.1 overexpression generates an APD gradient and a bimodal spatial and frequency-dependent CV gradient which we found to have a significant effect on fibrillatory dynamics. Uniform overexpression of Kir2.1 increased rotor frequency compared to UN and W-GFP and R-GFP controls, each group producing uniform DFs (Figure 3.13.A). However, R-Kir2.1 monolayers exhibited 2 different types of behavior, as follows: 1) Rotors localized to the uninfected region generated homogeneous propagation and uniform DF throughout the entire monolayer (11.3 ± 0.6 Hz, n=10, Figure 3.13.B). 2) Dominant rotors localized within the Kir2.1 overexpressing region generated wavebreak and fibrillatory conduction, with clearly demarcated DF domains (UN region: 12.3 ± 0.8 Hz, Kir2.1 region: 15.4 ± 1.1 Hz, Student paired t-test $p<0.005$, n=10, Figure 3.13.C). There was no preference for dominant rotor localization. Fibrillatory patterns mirrored simulation results: a uniform DF of 11.9 Hz when rotors were in the uninfected region and a regional DF distribution when the rotors were localized in the overexpressing region ($1xG_{K1}$ region: 9-10.4 Hz, $5xG_{K1}$ region: 18.4 Hz). When regional DF patterns were present, the DF in the uninfected region, although complex and irregular, was similar to UN and GFP groups while the DF in the Kir2.1 region was similar to frequencies observed in the W-Kir2.1 group (the reverse comparisons were significant). These results demonstrate how R-Kir2.1 gradients can generate wavebreak and fibrillatory conduction in a location dependent manner.

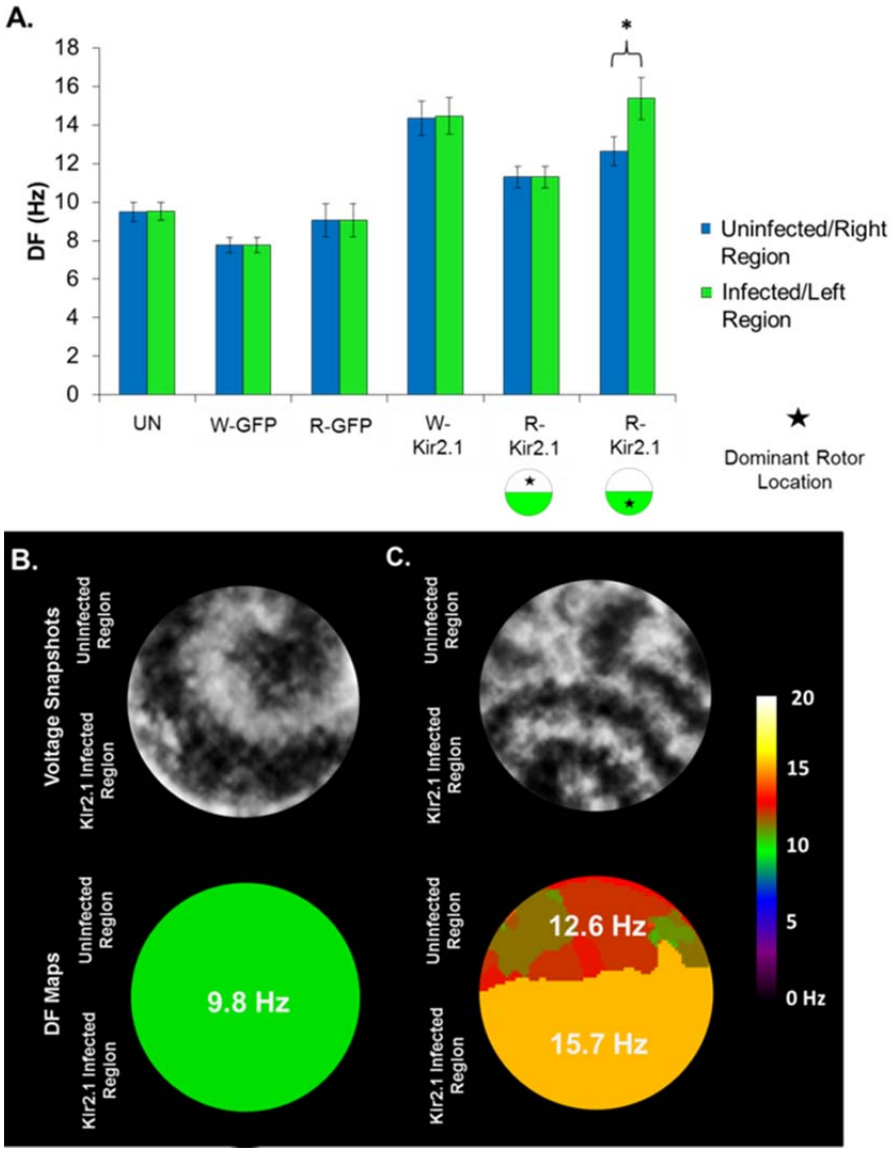

Figure 3.13. Rotor Activity. A. Regional DF values. No significant regional differences comparing UN, W-GFP, R-GFP, W-Kir2.1, or when the rotors localize within the uninfected region of the R-Kir2.1 monolayers were observed. Uninfected/right region of each group (blue), Infected/left region of each group (green). Regional DF heterogeneity was observed in R-Kir2.1 monolayers when the dominant rotors localized within the Kir2.1 overexpressing region (* $p<0.05$). **B.** R-Kir2.1 voltage snapshot when a rotor is localized within the uninfected region (top) and uninform DF map (bottom). **C.** Voltage snapshot when the dominant rotor is localized within the Kir2.1 overexpressing region (top) and DF map showing clearly demarcated DF domains (bottom), each color representing a domain and 12.6 Hz (red) being the most representative domain in the uninfected region.

3.4 Discussion

3.4.1 Major Findings

In this chapter we investigated the mechanism by which gradients in I_{K1} density contribute to high-frequency rotor formation, wavebreak and fibrillatory conduction. Our primary findings were: 1) In accordance with predictions derived from computer simulations, experimental monolayers in which Kir2.1 was overexpressed homogeneously demonstrated monotonic APD shortening in response to pacing frequency and degree of Kir2.1 overexpression. 2) In contrast, the effect of Kir2.1 overexpression on CV was frequency dependent and changed in a bimodal fashion. At relatively slow frequencies, CV decreased as the level of Kir2.1 overexpression was increased, while at frequencies above 7 Hz, CV was significantly faster in the Kir2.1 overexpressing monolayers. This occurred in a bimodal fashion with respect to the level of Kir2.1 overexpression. 3) In accordance with simulations, regional Kir2.1 heterogeneity created by local magnetofection-mediated Kir2.1 overexpression, generated APD gradients that remained significant at all activation frequencies. In contrast, above 7 Hz CV in the gradient region is faster than both uninfected and infected regions. Additionally, CV dispersion across R-Kir2.1 monolayers increased sharply as activation frequency increased above 7 Hz. In contrast, APD dispersion progressively decreased from 1 to 10 Hz. These results suggest that CV dispersion rather than APD dispersion is important in the generation of unidirectional block, wavebreak and turbulent propagation at higher frequencies. 4) Single cell simulations provided mechanistic insight into the presence of a bimodal CV profile by demonstrating that small increases in G_{K1} generated large

increases in sodium channel availability and a modest increase in I_{K1} slope conductance, whereas larger increases in G_{K1} resulted in a large increase in I_{K1} slope conductance with only a modest additional increase in sodium channel availability, all of which translates into a bimodal upstroke velocity as a function of G_{K1}. 5) In both experiments and simulations implementing regional I_{K1}, patterns of wavebreak and fibrillatory conduction were created in a location and frequency dependent manner; wavebreak was only generated if waves came from the Kir2.1 overexpressing region and were above 8 Hz. Overall, our study provides insight into the molecular mechanisms by which non-uniform distribution of the major repolarizing channel, I_{K1}, results in APD dispersion and bimodal spatial and frequency-dependent CV gradients which serve as a substrate for wavebreak and fibrillatory conduction.

3.4.2 Spatial Dispersion of I_{K1} Channels in the Heart

Spatially distributed heterogeneity of I_{K1} has been observed in a number of animal models and is associated with APD dispersion. In the mouse, there exists both a left atrium (LA)-to-right atrium (RA) gradient as well as apical-endocaridal gradient in I_{K1}, while the RV tends to have an increase in inward I_{K1} compared with LV[89, 122]. In the feline, the LV endocardial tissue has more inward and outward I_{K1} compared to epicardial tissue[123]. There is also I_{K1} heterogeneity between the LA and pulmonary veins (PV) in the canine[124]; PV I_{K1} density was reduced by about 58% of the LA[125]. This region of the atria is of particular interest as it has been implicated in the mechanisms of atrial fibrillation; ablation around the PV is often effective at terminating the arrhythmia. In the guinea pig, Samie *et al.*[57] found significant differences in the outward conductance of the I_{K1} current between left and right ventricles, almost 1.5

times greater. Warren *et al.*[118] found that there was an increase in both Kir2.1 and Kir2.3 mRNA within the LV; Kir2.1 was almost doubled and Kir2.3 increased by 1.5 times. While in the human a 2-fold gradient in I_{K1} is established between left and right atria during paroxsysmal AF[84]. These studies provided a link between the patterns of fibrillatory dynamics and the regional distribution of I_{K1}.

Cardiac fibrillation may depend on the presence of a small number of high frequency reentrant sources[57, 76, 170, 171]. Spiral wave fronts emanating periodically away from such sources may encounter functional, temporal and/or anatomical tissue heterogeneities and result in wavebreak with multiple wavelet formation[57]. The wavelets undergo irregular spatiotemporal patterns of fibrillatory conduction[7, 37]. In the isolated guinea pig heart, the presence of a fast and stable rotor driving fibrillatory activity has been demonstrated to correlate with gradients in I_{K1} density between the left and right ventricles[57]. However, details regarding the relationship between the spatial organization of excitation and the spatial I_{K1} distribution are lacking. Here we demonstrate that regional Kir2.1 heterogeneity can serve as a mechanism of rotor formation, wavebreak and fibrillatory conduction. Importantly, only rotors localized within higher Kir2.1 expression region resulted in wavebreak and fibrillatory conduction. No fibrillatory activity was observed when a driving rotor resided in lower I_{K1} regions or in uniformly infected monolayers. Kir2.1 overexpression hyperpolarizes the membrane potential and abbreviates APD, both factors contributing to rotor acceleration[113]. Our results identify not only a regional APD gradient, but a bimodal spatial and frequency-dependent CV gradient across regions with heterogeneous Kir2.1 overexpression. This is significantly different to the case of heterogeneous hERG expression in which APD dispersion plays the most prominent role (see Chapter II).

Computer simulations indicate that low increases in G_{K1} generate an increase in upstroke velocity due to a prominent impact of increased sodium channel availability, while higher levels of Kir2.1 cause a large enough hyperpolarization of the resting membrane potential to result in a decrease in the upstroke velocity. This bimodal spatial CV can be functionally observed in regional G_{K1} simulations, demonstrating its dependence on the level of G_{K1}. Simulations and experiments demonstrate how regional Kir2.1 heterogeneity establishes gradients in APD and CV which lead to wavebreak and fibrillatory conduction under certain conditions.

3.4.3 Clinical Relevance

A recent study in humans has suggested that a larger I_{K1} density in the left atrium explains the dominant left-to-right frequency gradients that prevail in patients with paroxysmal AF[84, 172]. This, together with the recent demonstration by Narayan *et al.* that AF in humans may result of long-standing rotors with fibrillatory conduction to the surrounding atrium[116], strongly supports the conclusion that rotors are the primary drivers of AF, at least in some patients. Most important, brief radiofrequency ablation at or near the center of rotation alone acutely terminated AF[116], this provides a solid rationale for investigating the mechanisms of wavebreak, rotor formation and fibrillatory conduction particularly as they relate to gradients in I_{K1}. Additionally, mutations in Kir2.1 are associated with short QT syndrome type 3 (SQT3), familial AF, Anderson-Tawil syndrome (LQT7) and catecholaminergic polymorphic ventricular tachycardia (CPVT), further identifying Kir2.1 as an important regulator of fibrillatory dynamics and a potential therapeutic target [85-88].

While our results cannot be extrapolated directly to the clinical situation, they demonstrate that heterogeneity in the form of spatially distributed APD and CV gradients constitutes a likely arrhythmogenic substrate in which waves emanating at high frequency from either focal or reentrant sources results in the turbulent electrical activation which manifests as fibrillatory conduction.

3.4.4 Limitations

Several limitations should be considered for this project. Cardiac fibrillation occurs in a complex 3-dimensonal structure and our study was performed in a simplified monolayer system. Nevertheless, we focused on ionic mechanisms of fibrillatory activity. Our methods provide a well-controlled model system to study the role of cellular and ionic heterogeneities in the generation of fibrillatory conduction. Such heterogeneities would be very difficult to study in the whole heart. Additionally, the electrical properties of NRVMs are vastly different from those of human myocytes and generate a slower CV. Kir2.1 channels expressed in rodent myocytes differ functionally from adult human channels. Nevertheless, we[113, 166, 174, 176] and others[119] have demonstrated that the uniform and heterogeneous NRVM models recapitulate many of the observations in whole adults hearts. We did not address the potential effects Kir2.1 overexpression may have on other transmembrane currents. Recent research has suggested a complex structural relationship between I_{K1} and I_{Na}; while this has not been demonstrated in NRVM we cannot exclude the possibility that Kir2.1 overexpression alters the expression patterns of other channels. Nevertheless, based on our experimental and numerical results, we are confident that regional Kir2.1 overexpression was an appropriate tool to generate predictable and quantifiable APD and CV gradients.

It may also be the case that magnetofection introduces unidentified effects on the electrophysiology of the cells. Yet we feel reassured that this technique did not adversely affect our preparations. Whole and regional magnetofection of Ad-GFP did not produce any effects on CV, APD or rotor frequency. We were also limited by the maximal level of Kir2.1 overexpression we could achieve. Increasing Kir2.1 above the level used in these experiments generated a very high proportion of monolayers which were no longer excitable. While this further supports the observation of a bimodal CV, it was not an optimal condition to study. We are also limited in our discussion of how regional Kir2.1 gradients impact rotor initiation and drift. We did not observe rotor initiation or drift of a driving rotor in any monolayer; as such we can only make assertions as to their final localization. Additionally, I_{K1} density was not assessed in our experimental model and any conclusions about the specific magnitude of I_{K1} are drawn from simulations.

At this time there are several limitations to our simulated results. In future we intend to increase the range of G_{K1} explored in both rotor and pacing experiments. This will allow us to confirm experimental results and identify how the level of G_{K1} specifically relates to the bimodal CV gradient as well as the frequency dependent threshold for wavebreak. It is likely that the overexpressing $5xG_{K1}$ region produced a slightly different level of G_{K1} than we generated in our experimental model. Simulations at $5xG_{K1}$ produced higher frequency rotors than 0.124 µl Ad-Kir2.1 overexpression, while $1xG_{K1}$ and uninfected regions in experiments produce very similar frequencies. Repeating these simulations over a more complete range of G_{K1} levels and pacing frequencies will allow us to further specify the frequency and level of G_{K1} which is sufficient for wavebreak and fibrillatory conduction.

3.5 Regional Kir2.1 Heterogeneity: Future Directions

This project has demonstrated that regional Kir2.1 overexpression is a mechanism for wavebreak and fibrillatory conduction. Experimental and simulation evidence points to both APD heterogeneity and bimodal spatial and frequency-dependent CV heterogeneity as the likely mechanisms responsible for the behavior. However, we have yet to fully elucidate the relative impact of these two mechanisms as they relate to wavebreak and fibrillatory conduction.

Future work with simulations will allow us to generate a regional G_{K1} model in which we can clamp the resting membrane potential and separate the mechanisms of the APD gradient from the bimodal CV gradient. Several sets of simulations will need to be run: 1) a regional APD model with no regional CV input (clamped throughout the monolayer); 2) a bimodal CV gradient without an APD gradient; 3) and a regional G_{K1} model which is progressively clamped at more depolarizing voltages. Additionally, simulations using single cell preparations are needed to demonstrate the frequency dependent effects of the bimodal CV we observed at 10 Hz. It is likely the frequency dependence is due, at least in part, to the rate dependency of the sodium channel availability. These additional simulations will elucidate the relative impact the Kir2.1-heterogeneity induced APD and bimodal CV gradients on the initiation of wavebreak and fibrillatory conduction which cannot be experimentally addressed.

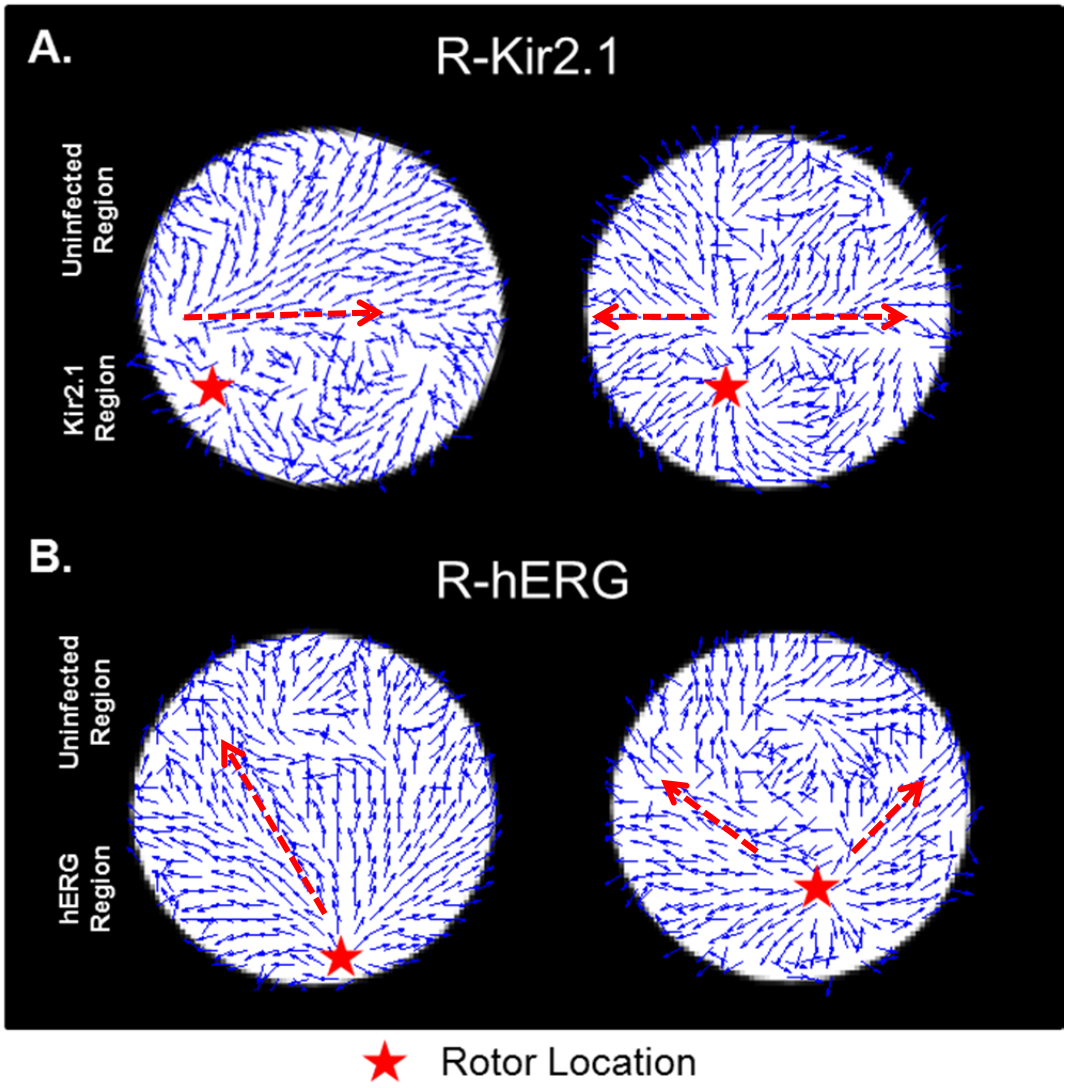

Figure 3.14. Directionality Vector Maps. A. R-Kir2.1 directionality maps of 2 examples with rotors localized within the overexpressing region (star) note the increased horizontal propagation at the gradient region. **B.** R-hERG directionality maps of 2 examples with the most amount of horizontal propagation at (or near) the gradient. The red arrows approximate the dominant direction of propagation at the gradient region.

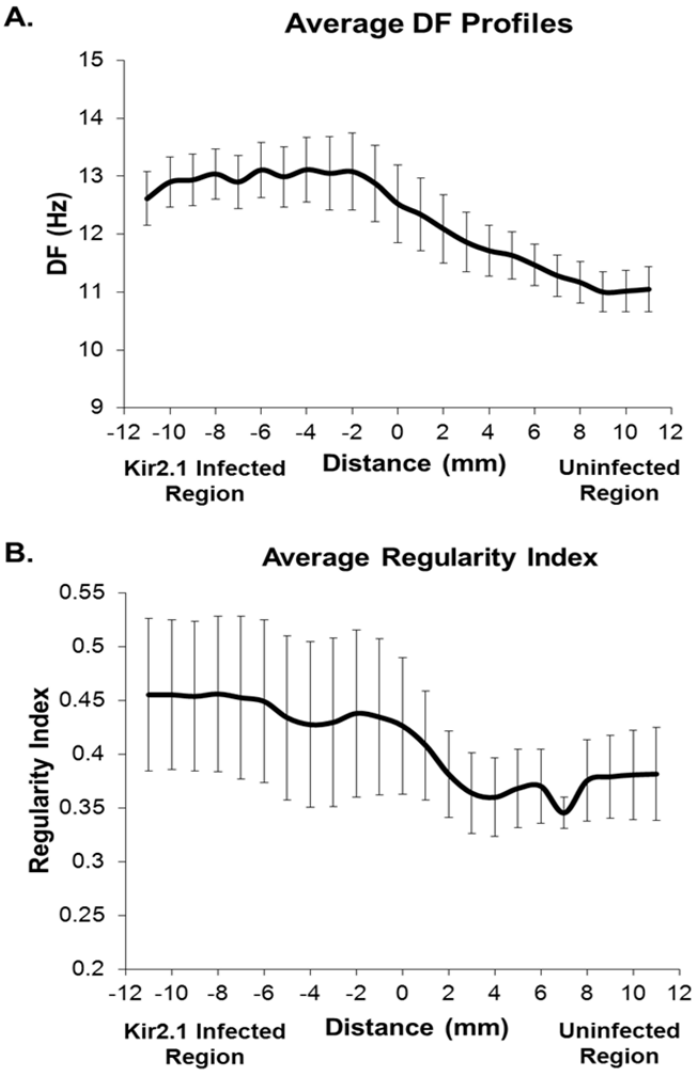

Figure 3.15. Average DF and RI Profiles. A. R-Kir2.1 average DF profile taken centrally perpendicular to infection gradient when rotors localize in the infected region. Peak DF at -4 mm is significantly greater than DF at any distance within the uninfected region (n = 10, $p<0.05$ Student paired t-test). **B.** R-Kir2.1 average RI, no points are significant but there is a trend for a decrease in RI within the uninfected region (comparison of maximum and minimum $p = 0.059$).

In addition to these simulations, we observed specific differences in the fibrillatory patterns between R-Kir2.1 and R-hERG monolayers. This suggests a need for further investigation into how APD and bimodal CV gradients influence propagation. R-Kir2.1 monolayers have demonstrated not only a regional APD gradient, but a bimodal spatial and frequency-dependent CV gradient. R-hERG monolayers, on the other hand, only generate an APD gradient between uninfected and infected regions (see

Chapter II). Such electrophysiological differences likely result in altered dynamics and wave propagation during high frequency activation by focal or rotor activity.

In this regard, we have noticed some intriguing differences in the wave propagation patterns at the gradient region in R-Kir2.1 experiments in comparison to our regional hERG studies examined in Chapter II. One such difference is the apparent tendency towards more horizontal propagation (parallel to the infection gradient) as the waves move into the gradient from the high-frequency region during fibrillation (see Figure 3.14). This suggests that the bimodal CV gradient we observed in R-Kir2.1, but not R-hERG, is having a modulatory effect on the dynamics of fibrillation, despite both groups having achieved a similar APD dispersion (13 ms vs. 16 ms) and rotor frequencies (15.4 Hz vs. 18 Hz).

DF profiles revealed further dissimilarities between R-hERG and R-Kir2.1 monolayers during fibrillation. R-hERG DF profiles were characterized by two distinct frequency plateaus, one in the hERG region and one in the uninfected region, with a centered DF gradient that spanned 2.3 ± 1.6 mm. In contrast to this narrow, centrally located DF gradient, R-Kir2.1 monolayers generated a significantly greater DF gradient width of 5.9 ± 0.7 mm which was shifted 3.5 mm into the uninfected region (Figure 3.15.A). It appears as though R-hERG causes a more abrupt DF transition which corresponds to the infection gradient, while R-Kir2.1 causes a more shallow DF transition which is shifted towards the uninfected region[33]. This strongly suggests that the additional CV gradient established by R-Kir2.1 has a modulatory effect on fibrillatory

[33] The frequency differences between infected regions of hERG and Kir2.1 monolayers may have an impact on these results. However, when looking at the width of the DF gradient in R-hERG monolayers with DF_{max} under 16 Hz (6/9) the DF gradient width shrinks to 0.73 ± 0.64 mm and is significantly less than the DF gradient width seen in R-Kir2.1 monolayers suggesting that this is not the case.

dynamics, both at the infection gradient and within the uninfected region when compared to the behavior observed in R-hERG monolayers.

Similarly, we saw differences when we examined the average regularity index (RI) profiles. R-Kir2.1 generates a small decline in RI at the gradient and throughout the uninfected region (Figure 3.15.B) while R-hERG created a significant dip in RI at the gradient region and then increased again within the uninfected region (Figure 2.12.C). R-Kir2.1 was more irregular than R-hERG throughout, and had only a slight drop between uninfected and infected regions. This suggests that R-Kir2.1 has a more destabilizing effect not just at the gradient, but also distally within the uninfected region as well, while R-hERG heterogeneity has a destabilizing effect at the gradient. Overall, this further suggests there is a role for bimodal CV gradients in the modulation of the dynamic patterns of fibrillation, and may be responsible for the increased propagation perpendicular to the infection gradient, the lengthening of the DF gradient and the increased disorganization of fibrillatory patterns.

In summary, the immediate future directions for this project should be to definitively establish whether R-Kir2.1's induced APD gradient or bimodal CV gradient is the primary mechanism for wavebreak. While the latter appears to have an important role in modulating patterns of fibrillation, it should be tested whether it is independently capable of generating wavebreak. Such results may provide important novel insights as our knowledge of multiple overlapping and interacting ionic gradients evolves.

Chapter VI

Thesis Summary: Regional hERG and Kir2.1 Heterogeneity

4.1 Overview

We are at a point where technological and scientific advancements provide us with the opportunity to integrate information from genetic and molecular levels to systemic and environmental levels. As a result, we have arrived at a more complete and necessarily more complex understanding of the interacting elements involved in cardiac arrhythmias. In this doctoral thesis, my project aims to integrate our understanding of some molecular and ionic concepts with some of the mechanisms governing electrical propagation and fibrillatory conduction. Specifically, the objective has been to determine the mechanisms by which regional gradients in repolarizing potassium channels (I_{Kr} and I_{K1}) contribute to propagation, rotor dynamics, and most importantly wavebreak and fibrillatory conduction.

Both of the projects in this thesis are concerned with very similar questions. Recognizing that regional ionic gradients in the heart have been shown to associate with regional fibrillatory patterns; can we determine if regional gradients in I_{Kr} or I_{K1} provide a substrate for wavebreak and fibrillation? The answer is unequivocally yes. Once we had developed a novel technique to allow appropriate investigation of this question, we were able to clearly demonstrate that regional overexpression of either of these major repolarizing potassium channels is capable of generating and controlling patterns of fibrillatory dynamics. That being said, we have discovered that they do this by somewhat individual mechanisms, resulting in different characteristic patterns of fibrillatory behavior.

The results put forth in this thesis suggest that native cardiac ionic gradients of either Kir2.1 or hERG may play an instrumental role in the generation of wavebreak and fibrillatory conduction. Moreover, our findings are in accordance with literature identifying regional frequency patterns within the chambers of the heart associated with regional expression patterns of each of these channels. Taken together this dissertation illustrates the importance, as well as the need, for a more comprehensive understanding of not just the individual ionic current during fibrillation, but of its regional ionic heterogeneities as well. It is important that we strive to understand the significance of how the multiple overlapping ionic heterogeneities in the heart so that we may better understand the mechanisms of responsible for these deadly arrhythmias.

4.2 Discoveries

4.2.1 Novel Investigative Technique: Regional Magnetofection

Regional ionic heterogeneities in I_{K1} and I_{Kr} have been shown to associate with regional fibrillatory patterns in a manner which, very convincingly, suggests that they have a major influence over fibrillatory behavior. However, it has yet to be demonstrated that these associations are causal to the disruptive behavior. This is because the heart contains quite a lot of structural and ionic heterogeneity[34]. The efficacy of this thesis project was entirely contingent upon our ability to engineer an appropriate model in which we could investigate regional ionic heterogeneity without the presence of additional regional structural heterogeneities.

To address this major technical limitation we made a number of attempts to generate such a reproducible model. However, by far the most successful was the adaptation of a magnetofection technique from a means to increase infection efficiency to one which allows for the regional infection within a monolayer of myocytes[35]. Several months were spent troubleshooting and optimizing this technique, but in the end we generated an experimental model which could easily and controllably generate regional ionic heterogeneity in a structurally uniform substrate. Regional magnetofection proved to be very effective in addressing our primary questions about how regional ionic heterogeneity in I_{K1} and I_{Kr} may be contributing to fibrillatory behaviors.

4.2.2 Chapter Synopses: Regional Ionic Heterogeneity

[34] There is also a large degree of molecular and genetic heterogeneity involved in everything from signaling pathways to proteins involved in mechanical functions of cardiac cells.

[35] For more detail on this subject see the methods section of Chapter II.

Using our novel regional magnetofection technique, in Chapter II we addressed what impact regional hERG heterogeneity has on fibrillatory dynamics. In brief, we found that both uniform and regional hERG heterogeneity increased the percentage of spontaneous rotors. Greater rates of spontaneous rotor formation were observed in the regional hERG monolayers, strongly signifying the arrhythmogenic potential of such regional gradients. Moreover, R-hERG monolayers generated wavebreak, regional DF heterogeneity and decreased RI at the infection gradient, in both a frequency and location dependent manner. Wavebreak and fibrillation only occurred when waves impinged upon the infection gradient from the hERG infected region and at a frequency above 12.9 Hz. To investigate the mechanism for this fibrillatory behavior we found that regional hERG overexpression generated a regional APD profile and a small gradient in maximal diastolic potential. Computer simulations enabled us to predict that while the transient hyperpolarization, caused by hERG overexpression, plays a role in rotor frequency, it has little to no effect on the dynamics of fibrillation; rather it is the regional hERG-induced APD gradient which is the primary mechanism for wavebreak and fibrillation observed in our model.

Chapter 3 is primarily concerned with the regional overexpression of Kir2.1. In this chapter we demonstrate how in addition to the expected APD gradient, we observed a novel bimodal spatial and frequency-dependent CV gradient as a result of regional Kir2.1 overexpression. We found that while APD dispersion progressively declines as frequency is increased, CV dispersion declines up to 7 Hz after which it sharply increases reversing the region of fastest CV. Additionally, above 7 Hz we see a bimodal spatial gradient in CV; the Kir2.1 gradient region produced faster CVs than the uninfected and Kir2.1 overexpressing regions. This

bimodal spatial and frequency-dependent CV response changed based on the level of Kir2.1 overexpression. This suggests that there is a range of interacting variables generated by regional Kir2.1 expression which can impact fibrillatory dynamics. Single cell simulations provide us with a mechanism for this observation. Small increases in I_{K1} increase sodium channel availability as the resting membrane potential hyperpolarizes, which leads to a net increase in upstroke velocity.[36] Larger increases in I_{K1} result in large changes to the resting membrane potential; without a great additional input from sodium channel availability, resulting in a net decrease in upstroke velocity.

In both monolayer experiments and simulations, we found that the regional Kir2.1 heterogeneity serves as a substrate for wavebreak and fibrillatory conduction in a similar location and frequency dependent manner as regional hERG heterogeneity; waves had to impinge upon the infection gradient from the Kir2.1 overexpressing region and had to be above 8 Hz, by pacing. In summary, regional Kir2.1 overexpression generates regional APD and bimodal spatial and frequency-dependent CV gradients, both of which contribute to a substrate for wavebreak and fibrillatory conduction.

4.3 Comparison: Kir2.1 vs. hERG Gradients

The cumulative result of the two projects included in this thesis provides a clear demonstration that regional ionic heterogeneity, affecting the primary determinants of propagation, has the potential to generate

[36] Simulations have yet to be completed to confirm this is the mechanism for the alterations in CV, but given the strong relationship between upstroke velocity and CV, it seems a likely result.

wavebreak and fibrillatory conduction. However, while both regional I_{K1} and I_{Kr} clearly demonstrate their contribution to fibrillatory dynamics, we observed some key differences in the character of their involvement. I will first preface this comparison by saying that we employed an overexpression model of each channel, and as such I cannot speak to the comparable levels of either current, or specifically how each channel relates to native levels of these ionic currents in the human heart. However, with that said, there is still a lot which can be gleaned from such a comparison.

Homogenous overexpression of either current led to increases in rotor frequency. However, one of the most surprising results we obtained was that even though I_{K1} has repeatedly been implicated in the control of rotor frequency, it was I_{Kr} overexpression which yielded the higher frequency behavior. This we believe is purely the result of experimental limitations we encountered. The Kir2.1 adenovirus we used had a tendency, even at an MOI of less than one[37], to generate monolayers which were no longer excitable. This suggests that our adenoviral promoter is quite strong, such that any individual infected cell will highly express Kir2.1 while its neighboring cells will produce only the native amount; this likely results in strong electrotonic effects between such neighboring cells. This may be introducing an element of local heterogeneity into our infected regions and perhaps preventing an optimal balance of sodium channel availability and I_{K1} conductance over a large enough area of cells to obtain a maximal increase in rotor frequency. We believe this to be the explanation for why hERG overexpression generated faster rotors than Kir2.1 overexpression.

[37] This resulted in a very poor infection efficiency using normal infection techniques, not magnetofection. Only a couple cells per ~500 were fluorescing per field of view suing a 10x objective.

Aside from this technical limitation, we found that within regionally infected monolayers, infected regions of either current led to increases in rotor frequency, while rotors localized within uninfected regions maintained frequencies similar to uninfected and GFP controls. This suggests that the gradient of either channel is not a major determinant of rotor behavior when the rotor is located at a distance to the gradient.[38] We found that when either R-hERG or R-Kir2.1 overexpression presented with dominant rotors localized in the uninfected regions, waves propagated with no disruption across the infection gradient. Similarly, both generated patterns of wavebreak and fibrillatory conduction when waves impinged upon the gradient coming from rotor or pacing activity in the infected regions, as long as the frequency was fast enough. All rotors in the infected region of R-Kir2.1 monolayers were fast enough to generate wavebreak (above 10.8 Hz). That being said R-hERG dishes required a minimum frequency of 12.8 Hz to generate wavebreak. This suggests that cardiac tissue containing Kir2.1 gradients may be more susceptible to wavebreak as it has a lower frequency threshold than tissue containing regional hERG heterogeneity.

Both fibrillatory groups generated clear and regionally assigned frequency domains. However, their DF profiles were surprisingly different. While R-hERG had a very steep, narrow and centrally located regional DF dispersion, R-Kir2.1 had a shallow and wide DF dispersion whose location was slightly shifted to the uninfected region. This may be due to the differences in rotor frequencies, caused by the aforementioned limitations to our viral construct. However, DF profile analysis of a subset of R-hERG

[38] In R-hERG overexpressing monolayers we did observe instances where rotors localized to the gradient region, the percentage of rotors within this region was reduced compared with the percentage of rotors localized within either infected or uninfected regions suggesting rotors may be less likely to stabilize in that region.

monolayers with slower frequencies resulted in an even sharper average DF gradient. This suggests that the dissimilarities in DF profiles are not purely frequency dependent; that they are more likely a consequence of the specific ion channel being regionally overexpressed. And indeed when comparing patterns of propagation between R-hERG and R-Kir2.1 movies we observe differences in the dynamics. Most notably there is an increase in the propagation along the gradient in R-Kir2.1 examples rather than across the gradient, which is more common in the R-hERG movies. This propagation may be contributing to the different pattern of wavebreak and frequency domains.

In addition to the DF profiles we found a marked difference in the regularity index when comparing these groups. R-hERG very clearly results in a decreased RI at the gradient region in comparison to both the infected and uninfected regions; while R-Kir2.1 produced no significant regional heterogeneities in RI. The trend we did observe was a sharp, but small decline in RI at the gradient which remained within the uninfected region. This suggests that the entirety of the uninfected region is subject to a more irregular and destabilizing influence, rather than just the gradient region as we see in R-hERG monolayers.

As mentioned previously, further investigation is needed into the relative importance of APD and CV gradients in the mechanisms of wavebreak in the setting of regional Kir2.1. However, given the similar APD heterogeneity generated by R-Kir2.1 and R-hERG, it seems reasonable to conclude that while APD heterogeneity is itself a proarrhythmic substrate, it is likely Kir2.1-induced bimodal CV heterogeneity is an important regulator of fibrillatory dynamics as well. Bimodal CV gradients may be important for decreasing the frequency

threshold for wavebreak and result in greater destabilization throughout the uninfected region.

Both regional Kir2.1 and hERG heterogeneity may play important roles in the generation of wavebreak and fibrillatory conduction in the whole heart. R-hERG primarily by way of establishing APD heterogeneity and R-Kir2.1 by way of APD heterogeneity and a bimodal CV gradient, increasing susceptibility to frequency dependent alterations and reducing the regularity of fibrillation in comparison to R-hERG.

4.4 Outlook

To fulfill the objective of developing better treatments for people who experience AF and VF we must continue to improve our understanding of the heart. To do this we need to bridge our understanding of molecular, genetic and ionic mechanisms with the dynamic electrical mechanisms along with the clinical states of cardiac fibrillation. The work presented in this thesis provides a clear demonstration of the relevance of regional ionic heterogeneity during fibrillation. We show how regional heterogeneity in either Kir2.1 or hERG can generate wavebreak and fibrillation; each having an enormous impact on fibrillatory dynamics. Taken together, this suggest that the native regional ionic gradients in the heart are likely contributing to the regional fibrillatory patterns so often seen in experimental and clinical settings. The work presented in this dissertation highlights the need for a more comprehensive and detailed understanding of the multiple overlapping and interacting ionic gradients in the heart; many parameters of which are still currently unknown. If we can understand how regional ionic heterogeneities in cardiac tissue contribute to atrial and ventricular

fibrillation we may eventually find a way to treat or even prevent these all too common clinical occurrences.

Appendix

Computer Simulations

A.1 Computer Simulations

Numerical simulations were performed using an existing mathematical model for the neonatal rat ventricular myocyte adapted to experimental data from our laboratory and previously described in detail[113]. AP morphology was already validated by patch clamp data previously[113]. Minor modifications in some ionic currents were done to better adjust the APD, conduction velocities and frequency gradients observed experimentally in our experimental model of regional I_{Kr} heterogeneity. Kinetics were left unchanged from the previous model. Table A.I summarizes those changes and Table A.II shows a comparison of the electrophysiological properties in the R-hERG experiments (optical mapping) and the model. No further modifications were made to the basic model for the I_{K1} experiments conducted in Chapter II. A 2D disk-shaped sheet used a Cartesian mesh of 352 × 352 nodes with a spatial resolution of 100 μm that contains a 35 mm diameter disk-shaped active domain in its center, with a non-diffusive outer domain boundary was used to simulate a NRVM monolayer of tissue. The area outside of the monolayer was implemented with passive and non-diffusive nodes for ease of

integration. The membrane model at each node was solved by the finite volume method with a time-step of 10 μs and no-flux boundary conditions, as described previously by Zlochiver *et al*.[166]. This model was employed to study and provide mechanistic understanding to the effects of regional hERG and Kir2.1 overexpression on reentry dynamics, impulse propagation and wavebreak formation in tissue.

This model was constructed with a resolution of 100 μm per computational cell and solved using the traditional monodomain formulation for the reaction-diffusion equation describing changes in transmembrane voltage for every computational cell (Equation 1). Discretization and linearization of the differential equation were performed using the finite volume method as previously described[177].

$$\frac{\partial V_m}{\partial t} = \frac{1}{C_m}(I_{stim} - I_m) + \nabla \cdot (D\nabla V_m) \quad (1)$$

G_{Kr} or G_{K1} maximal conductance was either set as homogeneous (whole G_K, 1xG_K–uninfected or 5xG_K–infected; G_K representing either G_{Kr} or G_{K1}) or varied spatially across the model (regional G_K model). To simulate the spatial gradient in G_{Kr} expression along the model we implemented the Boltzmann best fit of the hERG-GFP fluorescence data obtained in the experiments for all the groups (Figure 2.3 and 2.13). A native level of G_{Kr} was used in the 'uninfected' region (1x). G_{Kr} was increased over a range of 1 to 20 times basal levels within 'infected region' of the model. Similarly, the Boltzmann best fit of Kir2.1-IRES-GFP fluorescence data was implemented to create regional simulations (not shown). A native level of G_{K1} was used in the 'uninfected' region (1x) and G_{K1} in the infected region was increased to 1.5x, 2x, 5x and 10xG_{K1}. The following equation represents the Boltzmann distribution applied to the

maximal conductance (G_K representing either G_{Kr} or G_{K1} depending on the set of simulations) from the distal and proximal sides of the disk-shaped model (Equation 2). Parameters of the best fit are summarized in Table A.III.

$$G_{I_K}(x) = G_{I_{K,distal}} + \frac{G_{I_{K,proximal}} - G_{I_{K,distal}}}{1+e^{\left(\frac{X-X_{50}}{\Delta x}\right)}} \quad (2)$$

A.2 Parameter Measurements in Numerical Simulations

All the methods used for the parameter measurements from the numerical simulations have been described in detail before. Dominant frequency maps, DF spatial profiles and proximal to distal (n:m) activation ratios were built from the simulations as previously described, matching the experimental methods of analysis[140]. To plot APD, DF and MDP spatial profiles we averaged those parameters first in time for every pixel in the last second of the respective simulation and also in space in a band of 20 pixels width in the center. Local conduction velocity (CV) was obtained from activation times for each pixel as described previously in detail[113, 178, 179]. Briefly, distribution of activation times for a spatial neighborhood of 5 × 5 pixels were fitted into a plane, and gradients of activation times in each direction were calculated for each plane constructing both magnitude and directionality (angle) maps. Computer-assisted algorithms were used to build the phase maps and for the detection of singularity points. The instantaneous phase of the action potential at each pixel was determined by obtaining the inverse tangent of the ratio of the Hilbert transform signals and the original signals so that the angle, with values in between [–π,π], was color coded to represent the

different phases of the AP[118]. Singularity points (SP) were defined as a point where all the phases converged[180], neighboring sites around exhibit a continuous progression of phase of approximately 2π.

During functional reentry both APD and CV change gradually as a function of the distance from the center of rotation (core). To verify the properties of the rotors obtained in the different scenarios explored (homogeneous and heterogeneous conditions) and closely fit previously reported experimental observations from our laboratory[113], we measured CV as function of radial distance from the core and WL as function of distance along the curvature of the wavefront, as described elsewhere[107, 113].

A.3 Fitting Experimental Observations

Fitting simulations to experimental parameters was conducted with R-hERG experiments, and did not need to be repeated for R-Kir2.1 experiments. Both pacing and reentry were induced in homogeneous and heterogeneous models. Reentry was induced via S1-S2 cross-field stimulation protocol[181]. Pacing in the homogeneous models showed similar APD restitution properties as compared with experimental optical data. Table A.II shows how APD and CV properties were in good agreement with our experiments. Figure 2.13 shows on the left the Boltzman distribution of G_{Kr} between 5x and 1x. On the right is the same distribution in 2D used to simulate the experimental conditions of regional hERG infection. Panel B shows the resulting APD_{50} map with individual action potentials at locations 1-3 during pacing at 1 Hz from the $5xG_{Kr}$ region (white asterisk on map).

Rotors were initially generated in the homogeneous whole $1xG_{Kr}$ (uninfected) and $5xG_{Kr}$ (infected) models. The level of $5xG_{Kr}$ similarly matched the average DF of I_{Kr} whole experimental infections at 15.0 Hz

vs. 16.3 ± 0.51 Hz (Table A.III) and was the value used as reference. We induced rotors in a range of frequencies by increasing the level of I_{Kr} upregulation within the infected region from 1-20xG_{Kr}. In good agreement with experimental data the frequency of rotation increased as a result of the APD abbreviation within that region secondary to I_{Kr} upregulation.

When rotors where initiated in the infected half of the I_{Kr} regional model a spatial gradient in frequency was observed along the I_{Kr} gradient direction (from 10.7 to 14.6 Hz) while uniform profile appear otherwise (11.7 Hz). Figure 2.12 shows a comparison of DF spatial profiles as function of distance (along the I_{Kr} gradient for regional models) among the 3 models explored showing similar frequency gradients as in experiments (Summary in Table A.I, Figure 2.12 and 2.15).

Table A.I. Adjusted Parameters and Values in the Numerical NRVM Model.

Parameter	Description	Model
$\mathbf{K_{IK1}}$	Scaling factor for I_{K1}	1.7
$\mathbf{G_{Kr}}$	Maximal I_{Kr} conductance (mS/μF)	0.0123602
$\mathbf{G_{CaL}}$	Maximal I_{CaL} conductance (dm^3/F ms)	0.000031185
$\mathbf{G_{Na}}$	Maximal I_{Na} conductance (mS/μF)	5.3550
D	Diffusion coefficient in 2D simulations (cm^2/ms)	0.0065
$\boldsymbol{\beta_m}$	Scaling factor β_m	$\beta_m = 0.06 \cdot e^{-V/11}$

Table A.II. Comparison of Optical AP Characteristics from Experiments and Simulations. DF values in the model are for 5x.

Parameter		Experiments	Model
Uninfected APD_{50} (ms)	**1 Hz**	58.9 ± 2.32 ms	102.503 ms
Uninfected APD_{75} (ms)	**1 Hz**	117.3 ± 2.39 ms	117.568 ms
DF_{max} Uninfected Whole		9.5 ± 0.57 Hz	11.7 Hz
DF_{max} I_{Kr} Infected Whole		16.4 ± 0.51 Hz	15.0 Hz
DF_{max} Regional I_{Kr}: Uninfected Region		11.1 ± 0.55 Hz	11.7 Hz
DF_{max} Regional I_{Kr}: Infected Regional		18.0 ± 0.54 Hz	14.6 Hz
CV_{1Hz} Uninfected Whole		23.0 ± 0.97 cm/s	20.861 cm/s
CV_{1Hz} Infected Whole		20.4 ± 0.24 cm/s	20.528 cm/s

Table A.III. Parameters of the Boltzmann Best Fit Model the Regional I_{Kr} Heterogeneity.

Parameter	Description	Experiments	Model
x_{50}	Midpoint Location	~17.5 mm	17.6 mm
Δx	Slope of the Boltzmann Distribution	0.94 ± 0.078 mm	0.98676 mm

Bibliography

1. Kannel WB, Abbott RD, Savage DD, McNamara PM. Epidemiologic features of chronic atrial fibrillation: the Framingham study. N Engl J Med. 1982;306(17):1018-22.
2. Fuster V, Ryden LE, Cannom DS, Crijns HJ, Curtis AB, Ellenbogen KA, et al. 2011 ACCF/AHA/HRS focused updates incorporated into the ACC/AHA/ESC 2006 Guidelines for the management of patients with atrial fibrillation: a report of the American College of Cardiology Foundation/American Heart Association Task Force on Practice Guidelines developed in partnership with the European Society of Cardiology and in collaboration with the European Heart Rhythm Association and the Heart Rhythm Society. J Am Coll Cardiol. 2011;57(11):e101-98.
3. Calkins H, Kuck KH, Cappato R, Brugada J, Camm AJ, Chen SA, et al. 2012 HRS/EHRA/ECAS expert consensus statement on catheter and surgical ablation of atrial fibrillation: recommendations for patient selection, procedural techniques, patient management and follow-up, definitions, endpoints, and research trial design: a report of the Heart Rhythm Society (HRS) Task Force on Catheter and Surgical Ablation of Atrial Fibrillation. Developed in partnership with the European Heart Rhythm Association (EHRA), a registered branch of the European Society of Cardiology (ESC) and the European Cardiac Arrhythmia Society (ECAS); and in collaboration with the American College of Cardiology (ACC), American Heart Association (AHA), the Asia Pacific Heart Rhythm Society (APHRS), and the Society of Thoracic Surgeons (STS). Endorsed by the governing bodies of the American College of Cardiology Foundation, the American Heart Association, the European Cardiac Arrhythmia Society, the European Heart Rhythm Association, the Society of Thoracic Surgeons, the Asia Pacific Heart Rhythm Society, and the Heart Rhythm Society. Heart Rhythm. 2012;9(4):632-96 e21.
4. Myerburg RJ, Spooner PM. Opportunities for sudden death prevention: directions for new clinical and basic research. Cardiovasc Res. 2001;50(2):177-85.
5. Zipes DP, Wellens HJ. Sudden cardiac death. Circulation. 1998;98(21):2334-51.
6. Lloyd-Jones DM, Wang TJ, Leip EP, Larson MG, Levy D, Vasan RS, et al. Lifetime risk for development of atrial fibrillation: the Framingham Heart Study. Circulation. 2004;110(9):1042-6.
7. Jalife J. Ventricular fibrillation: mechanisms of initiation and maintenance. Annu Rev Physiol. 2000;62:25-50.
8. Moe GK, Rheinboldt WC, Abildskov JA. A Computer Model of Atrial Fibrillation. Am Heart J. 1964;67:200-20.
9. Jalife J, Gray RA, Morley GE, Davidenko JM. Self-organization and the dynamical nature of ventricular fibrillation. Chaos. 1998;8(1):79-93.
10. Jalife J, Berenfeld O, Skanes A, Mandapati R. Mechanisms of atrial fibrillation: mother rotors or multiple daughter wavelets, or both? J Cardiovasc Electrophysiol. 1998;9(8 Suppl):S2-12.
11. Lip GY, Beevers DG. ABC of atrial fibrillation. History, epidemiology, and importance of atrial fibrillation. BMJ. 1995;311(7016):1361-3. PMCID: 2551280.

12. Acierno LJ. The history of cardiology. London ; New York: Parthenon Pub. Group; 1994.
13. Bernardi W. [The controversy over animal electricity in 18th-century Italy: Galvani, Volta, and others]. Rev Hist Sci Paris. 2001;54(1):53-70.
14. Erichsen JE. On the influence of the coronary circulation on the action of the heart. London Medical Gazette. 1842;2:561-83.
15. Hoffa M, ; Ludwig, C;. Einige neue Versuche über Herzbewegung. Z Rationelle Med. 1850;9:107-44.
16. Vulpian A. Notes sur les effects de la faradization direct des ventricular du coeur chez le chien. Arch Phyisiol Norm Path. 1874;6:975-82.
17. McWilliams J. Electrical stimulation of the heart in man. British Medical Journal. 1889;1:298-310.
18. McWilliams JA. Fibrillar contraction of the heart. Journal of Physiology London. 1897;8:296-310.
19. Lewis T. Report Cxix. Auricular Fibrillation: A Common Clinical Condition. Br Med J. 1909;2(2552):1528. PMCID: 2321318.
20. Wit AL, Cranefield PF. Reentrant excitation as a cause of cardiac arrhythmias. Am J Physiol. 1978;235(1):H1-17.
21. Garrey W. The nature of fibrillary contraction of the heart-Its relation to tissue mass and form. American Journal of Physiology. 1914;33:397-414.
22. Mines GR. On dynamic equilibrium in the heart. J Physiol. 1913;46(4-5):349-83. PMCID: 1420430.
23. Wiggers CJ, Bell JR, Paine M. Studies of ventricular fibrillation caused by electric shock: II. Cinematographic and electrocardiographic observations of the natural process in the dog's heart. Its inhibition by potassium and the revival of coordinated beats by calcium. Ann Noninvasive Electrocardiol. 2003;8(3):252-61; discussion 1.
24. De Palma A, Pareti G. Bernstein's long path to membrane theory: radical change and conservation in nineteenth-century German electrophysiology. J Hist Neurosci. 2011;20(4):306-37.
25. Cole KS, Curtis HJ. Electric Impedance of the Squid Giant Axon during Activity. J Gen Physiol. 1939;22(5):649-70. PMCID: 2142006.
26. Cole KS, Hodgkin AL. Membrane and Protoplasm Resistance in the Squid Giant Axon. J Gen Physiol. 1939;22(5):671-87. PMCID: 2142005.
27. Coraboeuf SWE. Potentiels de repos et potentiels d'action du muscle cardiaque, mesurés à l'aide d'électrodes intracellulaires. CR Soc Biol (Paris). 1949;143:1329-31.
28. Draper MH, Weidmann S. Cardiac resting and action potentials recorded with an intracellular electrode. J Physiol. 1951;115(1):74-94. PMCID: 1392010.
29. Hodgkin AL, Huxley AF. Resting and action potentials in single nerve fibres. J Physiol. 1945;104(2):176-95. PMCID: 1393558.
30. Hodgkin AL, Huxley AF. Currents carried by sodium and potassium ions through the membrane of the giant axon of Loligo. J Physiol. 1952;116(4):449-72. PMCID: 1392213.

31. Weidmann S. The effect of the cardiac membrane potential on the rapid availability of the sodium-carrying system. J Physiol. 1955;127(1):213-24. PMCID: 1365850.
32. Hutter OF, Noble D. Rectifying properties of heart muscle. Nature. 1960;188:495.
33. Hall AE, Hutter OF, Noble D. Current-voltage relations of Purkinje fibres in sodium-deficient solutions. J Physiol. 1963;166:225-40. PMCID: 1359373.
34. Noble D, Garny A, Noble PJ. How the Hodgkin-Huxley equations inspired the Cardiac Physiome Project. J Physiol. 2012;590(Pt 11):2613-28. PMCID: 3424720.
35. Noble D, Tsien RW. Kinetics of slow component of potassium current in cardiac purkinje fibres. J Physiol. 1968;194(1):31P-2P.
36. Kleber AG, Rudy Y. Basic mechanisms of cardiac impulse propagation and associated arrhythmias. Physiol Rev. 2004;84(2):431-88.
37. Jalife J DM, Davidenko J, Anumonwo J. Basic Cardiac Electrophysiology for the Clinician. New York: Futura Publishing Co Inc; 1998.
38. Curtis KSCHJ. Membrane resting and action potentials from the squid giant axon. J Cell Comp Physiol. 1942;19:135-44.
39. Moe GK, Abildskov JA. Atrial fibrillation as a self-sustaining arrhythmia independent of focal discharge. Am Heart J. 1959;58(1):59-70.
40. Moe GK. Cardiac arrhythmias; introductory remarks. Ann N Y Acad Sci. 1956;64(4):540-2.
41. Allessie WEJEPLFIMBJHMA. Experimental evaluation of Moe's multiple wavelet hypothesis of atrial fibrillation In: Jalife DPZJ, editor. Cardiac Electrophysiology and Arrhythmias. Orlando, FL: Grune & Stratton; 1985.
42. Wiener N, Rosenblueth A. The mathematical formulation of the problem of conduction of impulses in a network of connected excitable elements, specifically in cardiac muscle. Arch Inst Cardiol Mex. 1946;16(3):205-65.
43. Allessie MA, Bonke FI, Schopman FJ. Circus movement in rabbit atrial muscle as a mechanism of tachycardia. III. The "leading circle" concept: a new model of circus movement in cardiac tissue without the involvement of an anatomical obstacle. Circ Res. 1977;41(1):9-18.
44. Allessie MA, Bonke FI, Schopman FJ. Circus movement in rabbit atrial muscle as a mechanism of trachycardia. Circ Res. 1973;33(1):54-62.
45. Winfree AT. Sudden cardia death: a problem in topology. Sci Am. 1983;248(5):144-9, 52-7, 60-1.
46. Selfridge O. Studies on flutter and fibrillation; some notes on the theory of flutter. Arch Inst Cardiol Mex. 1948;18(2):177-87.
47. Krinsky VI, Biktashev VN, Pertsov AM. Autowave approaches to cessation of reentrant arrhythmias. Ann N Y Acad Sci. 1990;591:232-46.
48. Krinskii VI. [Excitation propagation in nonhomogenous medium (actions analogous to heart fibrillation)]. Biofizika. 1966;11(4):676-83.
49. Gul'ko FB, Petrov AA. [Mechanism of formation of closed propagation pathways in excitable media]. Biofizika. 1972;17(2):261-70.

50. Winfree AT. Vortex action potentials in normal ventricular muscle. Ann N Y Acad Sci. 1990;591:190-207.
51. Frazier DW, Wolf PD, Wharton JM, Tang AS, Smith WM, Ideker RE. Stimulus-induced critical point. Mechanism for electrical initiation of reentry in normal canine myocardium. J Clin Invest. 1989;83(3):1039-52. PMCID: 303781.
52. Cabo C, Pertsov AM, Baxter WT, Davidenko JM, Gray RA, Jalife J. Wave-front curvature as a cause of slow conduction and block in isolated cardiac muscle. Circ Res. 1994;75(6):1014-28.
53. Davidenko JM, Pertsov AV, Salomonsz R, Baxter W, Jalife J. Stationary and drifting spiral waves of excitation in isolated cardiac muscle. Nature. 1992;355(6358):349-51.
54. Gray RA, Jalife J, Panfilov A, Baxter WT, Cabo C, Davidenko JM, et al. Nonstationary vortexlike reentrant activity as a mechanism of polymorphic ventricular tachycardia in the isolated rabbit heart. Circulation. 1995;91(9):2454-69.
55. Jalife J, Berenfeld O, Mansour M. Mother rotors and fibrillatory conduction: a mechanism of atrial fibrillation. Cardiovasc Res. 2002;54(2):204-16.
56. Jalife J, Berenfeld O. Molecular mechanisms and global dynamics of fibrillation: an integrative approach to the underlying basis of vortex-like reentry. J Theor Biol. 2004;230(4):475-87.
57. Samie FH, Berenfeld O, Anumonwo J, Mironov SF, Udassi S, Beaumont J, et al. Rectification of the background potassium current: a determinant of rotor dynamics in ventricular fibrillation. Circ Res. 2001;89(12):1216-23.
58. Gray RA, Pertsov AM, Jalife J. Spatial and temporal organization during cardiac fibrillation. Nature. 1998;392(6671):75-8.
59. Kim YH, Garfinkel A, Ikeda T, Wu TJ, Athill CA, Weiss JN, et al. Spatiotemporal complexity of ventricular fibrillation revealed by tissue mass reduction in isolated swine right ventricle. Further evidence for the quasiperiodic route to chaos hypothesis. J Clin Invest. 1997;100(10):2486-500. PMCID: 508449.
60. Vaquero M, Calvo D, Jalife J. Cardiac fibrillation: from ion channels to rotors in the human heart. Heart Rhythm. 2008;5(6):872-9. PMCID: 2486257.
61. Janse MJ, van Capelle FJ, Morsink H, Kleber AG, Wilms-Schopman F, Cardinal R, et al. Flow of "injury" current and patterns of excitation during early ventricular arrhythmias in acute regional myocardial ischemia in isolated porcine and canine hearts. Evidence for two different arrhythmogenic mechanisms. Circ Res. 1980;47(2):151-65.
62. Wiggers CJ, Theisen H, Williams HA. FURTHER OBSERVATIONS ON EXPERIMENTAL AORTIC INSUFFICIENCY: II. Cinematographic Studies of Changes in Ventricular Size and in Left Ventricular Discharge. J Clin Invest. 1930;9(2):215-33. PMCID: 435692.
63. Salzberg BM, Davila HV, Cohen LB. Optical recording of impulses in individual neurones of an invertebrate central nervous system. Nature. 1973;246(5434):508-9.
64. Morad M, Salama G. Optical probes of membrane potential in heart muscle. J Physiol. 1979;292:267-95. PMCID: 1280857.
65. Herron TJ, Lee P, Jalife J. Optical imaging of voltage and calcium in cardiac cells & tissues. Circ Res. 2012;110(4):609-23. PMCID: 3291718.

66. Jalife DSRJ, editor. Optical Mapping of Cardiac Excitation and Arrhythmias. Armonk, New York: Futura Publishing Company; 2001.
67. Loew LM, Cohen LB, Dix J, Fluhler EN, Montana V, Salama G, et al. A naphthyl analog of the aminostyryl pyridinium class of potentiometric membrane dyes shows consistent sensitivity in a variety of tissue, cell, and model membrane preparations. J Membr Biol. 1992;130(1):1-10.
68. Kuo CS, Munakata K, Reddy CP, Surawicz B. Characteristics and possible mechanism of ventricular arrhythmia dependent on the dispersion of action potential durations. Circulation. 1983;67(6):1356-67.
69. Sampson KJ, Henriquez CS. Simulation and prediction of functional block in the presence of structural and ionic heterogeneity. Am J Physiol Heart Circ Physiol. 2001;281(6):H2597-603.
70. Han J, Moe GK. Nonuniform Recovery of Excitability in Ventricular Muscle. Circ Res. 1964;14:44-60.
71. Cabo C, Pertsov AM, Davidenko JM, Jalife J. Electrical turbulence as a result of the critical curvature for propagation in cardiac tissue. Chaos. 1998;8(1):116-26.
72. Agladze K, Keener JP, Muller SC, Panfilov A. Rotating spiral waves created by geometry. Science. 1994;264(5166):1746-8.
73. Cabo C, Pertsov AM, Davidenko JM, Baxter WT, Gray RA, Jalife J. Vortex shedding as a precursor of turbulent electrical activity in cardiac muscle. Biophys J. 1996;70(3):1105-11. PMCID: 1225040.
74. Fast VG, Kleber AG. Role of wavefront curvature in propagation of cardiac impulse. Cardiovasc Res. 1997;33(2):258-71.
75. Comtois P, Kneller J, Nattel S. Of circles and spirals: bridging the gap between the leading circle and spiral wave concepts of cardiac reentry. Europace. 2005;7 Suppl 2:10-20.
76. Noujaim SF, Pandit SV, Berenfeld O, Vikstrom K, Cerrone M, Mironov S, et al. Up-regulation of the inward rectifier K+ current (I K1) in the mouse heart accelerates and stabilizes rotors. J Physiol. 2007;578(Pt 1):315-26. PMCID: 2075137.
77. Atienza F, Almendral J, Moreno J, Vaidyanathan R, Talkachou A, Kalifa J, et al. Activation of inward rectifier potassium channels accelerates atrial fibrillation in humans: evidence for a reentrant mechanism. Circulation. 2006;114(23):2434-42.
78. Beaumont J, Davidenko N, Davidenko JM, Jalife J. Spiral waves in two-dimensional models of ventricular muscle: formation of a stationary core. Biophys J. 1998;75(1):1-14. PMCID: 1299675.
79. Fakler B, Brandle U, Bond C, Glowatzki E, Konig C, Adelman JP, et al. A structural determinant of differential sensitivity of cloned inward rectifier K+ channels to intracellular spermine. FEBS Lett. 1994;356(2-3):199-203.
80. Fakler B, Brandle U, Glowatzki E, Weidemann S, Zenner HP, Ruppersberg JP. Strong voltage-dependent inward rectification of inward rectifier K+ channels is caused by intracellular spermine. Cell. 1995;80(1):149-54.
81. Ficker E, Taglialatela M, Wible BA, Henley CM, Brown AM. Spermine and spermidine as gating molecules for inward rectifier K+ channels. Science. 1994;266(5187):1068-72.

82. Lopatin AN, Makhina EN, Nichols CG. The mechanism of inward rectification of potassium channels: "long-pore plugging" by cytoplasmic polyamines. J Gen Physiol. 1995;106(5):923-55. PMCID: 2229292.
83. Lopatin AN, Makhina EN, Nichols CG. Potassium channel block by cytoplasmic polyamines as the mechanism of intrinsic rectification. Nature. 1994;372(6504):366-9.
84. Voigt N, Trausch A, Knaut M, Matschke K, Varro A, Van Wagoner DR, et al. Left-to-right atrial inward rectifier potassium current gradients in patients with paroxysmal versus chronic atrial fibrillation. Circ Arrhythm Electrophysiol. 2010;3(5):472-80.
85. Priori SG, Pandit SV, Rivolta I, Berenfeld O, Ronchetti E, Dhamoon A, et al. A novel form of short QT syndrome (SQT3) is caused by a mutation in the KCNJ2 gene. Circ Res. 2005;96(7):800-7.
86. Xia M, Jin Q, Bendahhou S, He Y, Larroque MM, Chen Y, et al. A Kir2.1 gain-of-function mutation underlies familial atrial fibrillation. Biochem Biophys Res Commun. 2005;332(4):1012-9.
87. Plaster NM, Tawil R, Tristani-Firouzi M, Canun S, Bendahhou S, Tsunoda A, et al. Mutations in Kir2.1 cause the developmental and episodic electrical phenotypes of Andersen's syndrome. Cell. 2001;105(4):511-9.
88. Barajas-Martinez H, Hu D, Ontiveros G, Caceres G, Desai M, Burashnikov E, et al. Biophysical and Molecular Characterization of a Novel de novo KCNJ2 Mutation Associated with Andersen-Tawil Syndrome and CPVT Mimicry. Circ Cardiovasc Genet. 2010.
89. Panama BK, McLerie M, Lopatin AN. Heterogeneity of IK1 in the mouse heart. Am J Physiol Heart Circ Physiol. 2007;293(6):H3558-67.
90. McLerie M, Lopatin AN. Dominant-negative suppression of I(K1) in the mouse heart leads to altered cardiac excitability. J Mol Cell Cardiol. 2003;35(4):367-78.
91. Miake J, Marban E, Nuss HB. Functional role of inward rectifier current in heart probed by Kir2.1 overexpression and dominant-negative suppression. J Clin Invest. 2003;111(10):1529-36. PMCID: 155052.
92. Li J, McLerie M, Lopatin AN. Transgenic upregulation of IK1 in the mouse heart leads to multiple abnormalities of cardiac excitability. Am J Physiol Heart Circ Physiol. 2004;287(6):H2790-802.
93. Noble D, Tsien RW. Outward membrane currents activated in the plateau range of potentials in cardiac Purkinje fibres. J Physiol. 1969;200(1):205-31. PMCID: 1350425.
94. Sanguinetti MC, Jurkiewicz NK. Two components of cardiac delayed rectifier K+ current. Differential sensitivity to block by class III antiarrhythmic agents. J Gen Physiol. 1990;96(1):195-215. PMCID: 2228985.
95. Wang Q, Curran ME, Splawski I, Burn TC, Millholland JM, VanRaay TJ, et al. Positional cloning of a novel potassium channel gene: KVLQT1 mutations cause cardiac arrhythmias. Nat Genet. 1996;12(1):17-23.
96. Barhanin J, Lesage F, Guillemare E, Fink M, Lazdunski M, Romey G. K(V)LQT1 and lsK (minK) proteins associate to form the I(Ks) cardiac potassium current. Nature. 1996;384(6604):78-80.

97. Sanguinetti MC, Curran ME, Zou A, Shen J, Spector PS, Atkinson DL, et al. Coassembly of K(V)LQT1 and minK (IsK) proteins to form cardiac I(Ks) potassium channel. Nature. 1996;384(6604):80-3.
98. Sanguinetti MC, Jiang C, Curran ME, Keating MT. A mechanistic link between an inherited and an acquired cardiac arrhythmia: HERG encodes the IKr potassium channel. Cell. 1995;81(2):299-307.
99. Trudeau MC, Warmke JW, Ganetzky B, Robertson GA. HERG, a human inward rectifier in the voltage-gated potassium channel family. Science. 1995;269(5220):92-5.
100. Sesti F, Abbott GW, Wei J, Murray KT, Saksena S, Schwartz PJ, et al. A common polymorphism associated with antibiotic-induced cardiac arrhythmia. Proc Natl Acad Sci U S A. 2000;97(19):10613-8. PMCID: 27073.
101. Splawski I, Shen J, Timothy KW, Lehmann MH, Priori S, Robinson JL, et al. Spectrum of mutations in long-QT syndrome genes. KVLQT1, HERG, SCN5A, KCNE1, and KCNE2. Circulation. 2000;102(10):1178-85.
102. Weerapura M, Nattel S, Chartier D, Caballero R, Hebert TE. A comparison of currents carried by HERG, with and without coexpression of MiRP1, and the native rapid delayed rectifier current. Is MiRP1 the missing link? J Physiol. 2002;540(Pt 1):15-27. PMCID: 2290231.
103. Chen YH, Xu SJ, Bendahhou S, Wang XL, Wang Y, Xu WY, et al. KCNQ1 gain-of-function mutation in familial atrial fibrillation. Science. 2003;299(5604):251-4.
104. Sanguinetti MC. Long QT syndrome: ionic basis and arrhythmia mechanism in long QT syndrome type 1. J Cardiovasc Electrophysiol. 2000;11(6):710-2.
105. Bellocq C, van Ginneken AC, Bezzina CR, Alders M, Escande D, Mannens MM, et al. Mutation in the KCNQ1 gene leading to the short QT-interval syndrome. Circulation. 2004;109(20):2394-7.
106. Hong K, Piper DR, Diaz-Valdecantos A, Brugada J, Oliva A, Burashnikov E, et al. De novo KCNQ1 mutation responsible for atrial fibrillation and short QT syndrome in utero. Cardiovasc Res. 2005;68(3):433-40.
107. Munoz V, Grzeda KR, Desplantez T, Pandit SV, Mironov S, Taffet SM, et al. Adenoviral expression of IKs contributes to wavebreak and fibrillatory conduction in neonatal rat ventricular cardiomyocyte monolayers. Circ Res. 2007;101(5):475-83.
108. Sun ZQ, Thomas GP, Antzelevitch C. Chromanol 293B inhibits slowly activating delayed rectifier and transient outward currents in canine left ventricular myocytes. J Cardiovasc Electrophysiol. 2001;12(4):472-8.
109. Varro A, Balati B, Iost N, Takacs J, Virag L, Lathrop DA, et al. The role of the delayed rectifier component IKs in dog ventricular muscle and Purkinje fibre repolarization. J Physiol. 2000;523 Pt 1:67-81. PMCID: 2269783.
110. Gaita F, Giustetto C, Bianchi F, Wolpert C, Schimpf R, Riccardi R, et al. Short QT Syndrome: a familial cause of sudden death. Circulation. 2003;108(8):965-70.
111. Brugada R, Hong K, Dumaine R, Cordeiro J, Gaita F, Borggrefe M, et al. Sudden death associated with short-QT syndrome linked to mutations in HERG. Circulation. 2004;109(1):30-5.

112. Perrin MJ, Subbiah RN, Vandenberg JI, Hill AP. Human ether-a-go-go related gene (hERG) K+ channels: function and dysfunction. Prog Biophys Mol Biol. 2008;98(2-3):137-48.
113. Hou L, Deo M, Furspan P, Pandit SV, Mironov S, Auerbach DS, et al. A major role for HERG in determining frequency of reentry in neonatal rat ventricular myocyte monolayer. Circ Res. 2010;107(12):1503-11. PMCID: 3005848.
114. Nuss HB, Marban E, Johns DC. Overexpression of a human potassium channel suppresses cardiac hyperexcitability in rabbit ventricular myocytes. J Clin Invest. 1999;103(6):889-96. PMCID: 408140.
115. Hua F, Johns DC, Gilmour RF, Jr. Suppression of electrical alternans by overexpression of HERG in canine ventricular myocytes. Am J Physiol Heart Circ Physiol. 2004;286(6):H2342-51.
116. Narayan SM, Patel J, Mulpuru S, Krummen DE. Focal impulse and rotor modulation ablation of sustaining rotors abruptly terminates persistent atrial fibrillation to sinus rhythm with elimination on follow-up: a video case study. Heart Rhythm. 2012;9(9):1436-9. PMCID: 3432749.
117. Zaitsev AV, Berenfeld O, Mironov SF, Jalife J, Pertsov AM. Distribution of excitation frequencies on the epicardial and endocardial surfaces of fibrillating ventricular wall of the sheep heart. Circ Res. 2000;86(4):408-17.
118. Warren M, Guha PK, Berenfeld O, Zaitsev A, Anumonwo JM, Dhamoon AS, et al. Blockade of the inward rectifying potassium current terminates ventricular fibrillation in the guinea pig heart. J Cardiovasc Electrophysiol. 2003;14(6):621-31.
119. Sekar RB, Kizana E, Cho HC, Molitoris JM, Hesketh GG, Eaton BP, et al. IK1 heterogeneity affects genesis and stability of spiral waves in cardiac myocyte monolayers. Circ Res. 2009;104(3):355-64. PMCID: 2789171.
120. Anumonwo JM, Lopatin AN. Cardiac strong inward rectifier potassium channels. J Mol Cell Cardiol. 2010;48(1):45-54. PMCID: 2813336.
121. Dhamoon AS, Jalife J. The inward rectifier current (IK1) controls cardiac excitability and is involved in arrhythmogenesis. Heart Rhythm. 2005;2(3):316-24.
122. Brunet S, Aimond F, Li H, Guo W, Eldstrom J, Fedida D, et al. Heterogeneous expression of repolarizing, voltage-gated K+ currents in adult mouse ventricles. J Physiol. 2004;559(Pt 1):103-20. PMCID: 1665075.
123. Furukawa T, Kimura S, Furukawa N, Bassett AL, Myerburg RJ. Potassium rectifier currents differ in myocytes of endocardial and epicardial origin. Circ Res. 1992;70(1):91-103.
124. Cha TJ, Ehrlich JR, Zhang L, Chartier D, Leung TK, Nattel S. Atrial tachycardia remodeling of pulmonary vein cardiomyocytes: comparison with left atrium and potential relation to arrhythmogenesis. Circulation. 2005;111(6):728-35.
125. Ehrlich JR, Cha TJ, Zhang L, Chartier D, Melnyk P, Hohnloser SH, et al. Cellular electrophysiology of canine pulmonary vein cardiomyocytes: action potential and ionic current properties. J Physiol. 2003;551(Pt 3):801-13. PMCID: 2343292.
126. Beuckelmann DJ, Nabauer M, Erdmann E. Alterations of K+ currents in isolated human ventricular myocytes from patients with terminal heart failure. Circ Res. 1993;73(2):379-85.

127. Dobrev D, Wettwer E, Kortner A, Knaut M, Schuler S, Ravens U. Human inward rectifier potassium channels in chronic and postoperative atrial fibrillation. Cardiovasc Res. 2002;54(2):397-404.
128. Pogwizd SM, Schlotthauer K, Li L, Yuan W, Bers DM. Arrhythmogenesis and contractile dysfunction in heart failure: Roles of sodium-calcium exchange, inward rectifier potassium current, and residual beta-adrenergic responsiveness. Circ Res. 2001;88(11):1159-67.
129. Fauconnier J, Lacampagne A, Rauzier JM, Vassort G, Richard S. Ca2+-dependent reduction of IK1 in rat ventricular cells: a novel paradigm for arrhythmia in heart failure? Cardiovasc Res. 2005;68(2):204-12.
130. Tsuji Y, Opthof T, Kamiya K, Yasui K, Liu W, Lu Z, et al. Pacing-induced heart failure causes a reduction of delayed rectifier potassium currents along with decreases in calcium and transient outward currents in rabbit ventricle. Cardiovasc Res. 2000;48(2):300-9.
131. Rozanski GJ, Xu Z, Whitney RT, Murakami H, Zucker IH. Electrophysiology of rabbit ventricular myocytes following sustained rapid ventricular pacing. J Mol Cell Cardiol. 1997;29(2):721-32.
132. Koumi S, Arentzen CE, Backer CL, Wasserstrom JA. Alterations in muscarinic K+ channel response to acetylcholine and to G protein-mediated activation in atrial myocytes isolated from failing human hearts. Circulation. 1994;90(5):2213-24.
133. Li D, Melnyk P, Feng J, Wang Z, Petrecca K, Shrier A, et al. Effects of experimental heart failure on atrial cellular and ionic electrophysiology. Circulation. 2000;101(22):2631-8.
134. Kleiman RB, Houser SR. Outward currents in normal and hypertrophied feline ventricular myocytes. Am J Physiol. 1989;256(5 Pt 2):H1450-61.
135. Furukawa T, Bassett AL, Furukawa N, Kimura S, Myerburg RJ. The ionic mechanism of reperfusion-induced early afterdepolarizations in feline left ventricular hypertrophy. J Clin Invest. 1993;91(4):1521-31. PMCID: 288128.
136. Farid TA, Nair K, Masse S, Azam MA, Maguy A, Lai PF, et al. Role of KATP channels in the maintenance of ventricular fibrillation in cardiomyopathic human hearts. Circ Res. 2011;109(11):1309-18.
137. Miyoshi S, Miyazaki T, Moritani K, Ogawa S. Different responses of epicardium and endocardium to KATP channel modulators during regional ischemia. Am J Physiol. 1996;271(1 Pt 2):H140-7.
138. Furukawa T, Kimura S, Furukawa N, Bassett AL, Myerburg RJ. Role of cardiac ATP-regulated potassium channels in differential responses of endocardial and epicardial cells to ischemia. Circ Res. 1991;68(6):1693-702.
139. Pandit SV, Kaur K, Zlochiver S, Noujaim SF, Furspan P, Mironov S, et al. Left-to-right ventricular differences in I(KATP) underlie epicardial repolarization gradient during global ischemia. Heart Rhythm. 2011;8(11):1732-9. PMCID: 3244837.
140. Berenfeld O, Zaitsev AV, Mironov SF, Pertsov AM, Jalife J. Frequency-dependent breakdown of wave propagation into fibrillatory conduction across the pectinate muscle network in the isolated sheep right atrium. Circ Res. 2002;90(11):1173-80.

141. Mandapati R, Skanes A, Chen J, Berenfeld O, Jalife J. Stable microreentrant sources as a mechanism of atrial fibrillation in the isolated sheep heart. Circulation. 2000;101(2):194-9.
142. Sarmast F, Kolli A, Zaitsev A, Parisian K, Dhamoon AS, Guha PK, et al. Cholinergic atrial fibrillation: I(K,ACh) gradients determine unequal left/right atrial frequencies and rotor dynamics. Cardiovasc Res. 2003;59(4):863-73.
143. Mansour M, Mandapati R, Berenfeld O, Chen J, Samie FH, Jalife J. Left-to-right gradient of atrial frequencies during acute atrial fibrillation in the isolated sheep heart. Circulation. 2001;103(21):2631-6.
144. Liu DW, Antzelevitch C. Characteristics of the delayed rectifier current (IKr and IKs) in canine ventricular epicardial, midmyocardial, and endocardial myocytes. A weaker IKs contributes to the longer action potential of the M cell. Circ Res. 1995;76(3):351-65.
145. Bryant SM, Wan X, Shipsey SJ, Hart G. Regional differences in the delayed rectifier current (IKr and IKs) contribute to the differences in action potential duration in basal left ventricular myocytes in guinea-pig. Cardiovasc Res. 1998;40(2):322-31.
146. Brahmajothi MV, Morales MJ, Reimer KA, Strauss HC. Regional localization of ERG, the channel protein responsible for the rapid component of the delayed rectifier, K+ current in the ferret heart. Circ Res. 1997;81(1):128-35.
147. Charles Antzelevitch VN, Adam L. Muzikant, J. Jeremy Rice, Gang Chen, Thomas Colatsky. Influence of transmural repolarization gradients on the elctrophysiology and pharmacology of ventricular myocardium. Cellular basis for the Brugada and long-QT syndromes. Phil Trans R Soc Lond A 2001;359:1201-16.
148. Li D, Zhang L, Kneller J, Nattel S. Potential ionic mechanism for repolarization differences between canine right and left atrium. Circ Res. 2001;88(11):1168-75.
149. Jalife J. Rotors and spiral waves in atrial fibrillation. J Cardiovasc Electrophysiol. 2003;14(7):776-80.
150. Nanthakumar K, Jalife J, Masse S, Downar E, Pop M, Asta J, et al. Optical mapping of Langendorff-perfused human hearts: establishing a model for the study of ventricular fibrillation in humans. Am J Physiol Heart Circ Physiol. 2007;293(1):H875-80.
151. Amit G, Kikuchi K, Greener ID, Yang L, Novack V, Donahue JK. Selective molecular potassium channel blockade prevents atrial fibrillation. Circulation. 2010;121(21):2263-70. PMCID: 2892844.
152. Rohr S, Fluckiger-Labrada R, Kucera JP. Photolithographically defined deposition of attachment factors as a versatile method for patterning the growth of different cell types in culture. Pflugers Arch. 2003;446(1):125-32.
153. Kadota S, Kanayama T, Miyajima N, Takeuchi K, Nagata K. Enhancing of measles virus infection by magnetofection. J Virol Methods. 2005;128(1-2):61-6.
154. Plank C, Schillinger U, Scherer F, Bergemann C, Remy JS, Krotz F, et al. The magnetofection method: using magnetic force to enhance gene delivery. Biol Chem. 2003;384(5):737-47.
155. Liu G, Gao J, Ai H, Chen X. Applications and Potential Toxicity of Magnetic Iron Oxide Nanoparticles. Small. 2012.

156. Huth S, Lausier J, Gersting SW, Rudolph C, Plank C, Welsch U, et al. Insights into the mechanism of magnetofection using PEI-based magnetofectins for gene transfer. J Gene Med. 2004;6(8):923-36.
157. Zhang Y, Bergelson JM. Adenovirus receptors. J Virol. 2005;79(19):12125-31. PMCID: 1211528.
158. Scherer F, Anton M, Schillinger U, Henke J, Bergemann C, Kruger A, et al. Magnetofection: enhancing and targeting gene delivery by magnetic force in vitro and in vivo. Gene Ther. 2002;9(2):102-9.
159. Sharifi S, Behzadi S, Laurent S, Forrest ML, Stroeve P, Mahmoudi M. Toxicity of nanomaterials. Chem Soc Rev. 2012;41(6):2323-43.
160. Shubayev VI, Pisanic TR, 2nd, Jin S. Magnetic nanoparticles for theragnostics. Adv Drug Deliv Rev. 2009;61(6):467-77. PMCID: 2700776.
161. Soenen SJ, Illyes E, Vercauteren D, Braeckmans K, Majer Z, De Smedt SC, et al. The role of nanoparticle concentration-dependent induction of cellular stress in the internalization of non-toxic cationic magnetoliposomes. Biomaterials. 2009;30(36):6803-13.
162. Naqvi S, Samim M, Abdin M, Ahmed FJ, Maitra A, Prashant C, et al. Concentration-dependent toxicity of iron oxide nanoparticles mediated by increased oxidative stress. Int J Nanomedicine. 2010;5:983-9. PMCID: 3010160.
163. Zhou Z, Gong Q, Ye B, Fan Z, Makielski JC, Robertson GA, et al. Properties of HERG channels stably expressed in HEK 293 cells studied at physiological temperature. Biophys J. 1998;74(1):230-41. PMCID: 1299377.
164. Morley GE, Vaidya D, Samie FH, Lo C, Delmar M, Jalife J. Characterization of conduction in the ventricles of normal and heterozygous Cx43 knockout mice using optical mapping. J Cardiovasc Electrophysiol. 1999;10(10):1361-75.
165. Kalifa J, Tanaka K, Zaitsev AV, Warren M, Vaidyanathan R, Auerbach D, et al. Mechanisms of wave fractionation at boundaries of high-frequency excitation in the posterior left atrium of the isolated sheep heart during atrial fibrillation. Circulation. 2006;113(5):626-33.
166. Zlochiver S, Munoz V, Vikstrom KL, Taffet SM, Berenfeld O, Jalife J. Electrotonic myofibroblast-to-myocyte coupling increases propensity to reentrant arrhythmias in two-dimensional cardiac monolayers. Biophys J. 2008;95(9):4469-80. PMCID: 2567962.
167. Cheng K, Li TS, Malliaras K, Davis DR, Zhang Y, Marban E. Magnetic targeting enhances engraftment and functional benefit of iron-labeled cardiosphere-derived cells in myocardial infarction. Circ Res. 2010;106(10):1570-81. PMCID: 2885138.
168. Stoll M, Quentin M, Molojavyi A, Thamer V, Decking UK. Spatial heterogeneity of myocardial perfusion predicts local potassium channel expression and action potential duration. Cardiovasc Res. 2008;77(3):489-96.
169. Obreztchikova MN, Patberg KW, Plotnikov AN, Ozgen N, Shlapakova IN, Rybin AV, et al. I(Kr) contributes to the altered ventricular repolarization that determines long-term cardiac memory. Cardiovasc Res. 2006;71(1):88-96.
170. Jalife J, Gray R. Drifting vortices of electrical waves underlie ventricular fibrillation in the rabbit heart. Acta Physiol Scand. 1996;157(2):123-31.

171. Vaidya D, Morley GE, Samie FH, Jalife J. Reentry and fibrillation in the mouse heart. A challenge to the critical mass hypothesis. Circ Res. 1999;85(2):174-81.
172. Caballero R, de la Fuente MG, Gomez R, Barana A, Amoros I, Dolz-Gaiton P, et al. In humans, chronic atrial fibrillation decreases the transient outward current and ultrarapid component of the delayed rectifier current differentially on each atria and increases the slow component of the delayed rectifier current in both. J Am Coll Cardiol. 2010;55(21):2346-54.
173. Shimizu W, Antzelevitch C. Effects of a K(+) channel opener to reduce transmural dispersion of repolarization and prevent torsade de pointes in LQT1, LQT2, and LQT3 models of the long-QT syndrome. Circulation. 2000;102(6):706-12.
174. Deo M, Sato PY, Musa H, Lin X, Pandit SV, Delmar M, et al. Relative contribution of changes in sodium current vs intercellular coupling on reentry initiation in two dimensional preparations of Plakophilin-2-deficient cardiac cells. Heart Rhythm. 2011.
175. Zobel C, Cho HC, Nguyen TT, Pekhletski R, Diaz RJ, Wilson GJ, et al. Molecular dissection of the inward rectifier potassium current (IK1) in rabbit cardiomyocytes: evidence for heteromeric co-assembly of Kir2.1 and Kir2.2. J Physiol. 2003;550(Pt 2):365-72. PMCID: 2343053.
176. Campbell KF, Calvo CJ, Mironov S, Herron T, Berenfeld O, Jalife J. Spatial Gradients in Action Potential Duration Created by Regional Magnetofection of hERG are a Substrate for Wavebreak and Turbulent Propagation in a Rat Cardiomyocyte Monolayer Model of Cardiac Fibrillation. J Physiol. 2012.
177. Abboud S, Eshel Y, Levy S, Rosenfeld M. Numerical calculation of the potential distribution due to dipole sources in a spherical model of the head. Comput Biomed Res. 1994;27(6):441-55.
178. Mironov S, Jalife J, Tolkacheva EG. Role of conduction velocity restitution and short-term memory in the development of action potential duration alternans in isolated rabbit hearts. Circulation. 2008;118(1):17-25. PMCID: 2574713.
179. Korhonen T, Hanninen SL, Tavi P. Model of excitation-contraction coupling of rat neonatal ventricular myocytes. Biophys J. 2009;96(3):1189-209. PMCID: 2716686.
180. Iyer AN, Gray RA. An experimentalist's approach to accurate localization of phase singularities during reentry. Ann Biomed Eng. 2001;29(1):47-59.
181. Leon LJ, Roberge FA, Vinet A. Simulation of two-dimensional anisotropic cardiac reentry: effects of the wavelength on the reentry characteristics. Ann Biomed Eng. 1994;22(6):592-609.